



Universidad de Jaén

PONTIFICIA UNIVERSIDAD CATÓLICA DEL PERÚ

Escuela de Posgrado

Contribution to the characterization of emerging
photovoltaics technologies in Lima-Peru

Tesis para obtener el grado académico de Doctor en Física que
presenta:

Luis Angel Conde Mendoza

Asesores:

Dr. Jan Amaru Palomino Töfflinger

Dr. Juan de la Casa Higuera

Lima, 2022

Declaración jurada de autenticidad


Yo, Jan Amaru Palomino Töfflinger, docente de la Escuela de Posgrado de la Pontificia Universidad Católica del Perú, y yo, Juan de la Casa Higuera, docente de la Universidad de Jaén, asesores de la tesis titulada “*Contribution to the characterization of emerging photovoltaics technologies in Lima-Peru*” del autor Luis Angel Conde Mendoza, para la obtención del Doble Título de Doctor en Régimen de Cotutela Internacional, dejamos constancia de lo siguiente:

- El mencionado documento tiene un índice de puntuación de similitud de 25%, pero se tiene que omitir las referencias 1 y 12 del informe dado que estas son artículos elaborados por el mismo alumno y producto de la tesis doctoral. El índice de similitud, omitiendo las referencias señaladas, es de 14 %, lo que está dentro del límite establecido. Así lo consigna el reporte de similitud emitido por el software Turnitin el 1/12/2022.
- Hemos revisado con detalle dicho reporte y confirmamos que cada una de las coincidencias detectadas no constituyen plagio alguno.
- Las citas a otros autores y sus respectivas referencias cumplen con las pautas académicas.

Lugar y fecha: Lima, 05 de diciembre de 2022

| | |
|---|--|
| Apellidos y nombres de asesor 1: Palomino Töfflinger, Jan Amaru | |
| DNI: 48866095 | Firma:  |
| ORCID: https://orcid.org/0000-0002-2076-4046 | |

Lugar y fecha: Jaén, 05 de diciembre de 2022

| | |
|---|---|
| Apellidos y nombres de asesor 2: de la Casa Higuera, Juan | |
| DNI: 26001227A | Firma:  |
| ORCID: https://orcid.org/0000-0002-1781-3417 | |

Acknowledgments

First of all, I would like to express my gratitude to all the people who have helped me during the years of the development of this thesis.

A special thanks to my supervisors for the efforts invested to initiate the successful collaboration between PUCP and UJA. I want to thank Dr. Amaru Töfflinger for all his support, patience and trust, and for allowing me to start and be part of this new line of research in Photovoltaics in the MatER-PUCP group. By the funds that he always helped me to obtain and all the experiences that we share in our trips. Thanks to his scientific knowledge and his advice, he helped me mature scientifically and personally.

Thanks to Dr. Juan de la Casa, my second supervisor, for all his support and patience in the doctoral program at UJA. For all the facilities that he gave me in my first internships abroad and for allowing me to work in his laboratories and share his experience and advice.

From the IDEA Research Group of the UJA. I would like to thank Dr. Jesús Montes for sharing his knowledge and experience in the development of measurement systems. Also, thanks to Dr. Gustavo Nofuentes for his great support and patience in the development of my first high-impact scientific publication.

Thanks to the professors who lead the MatER-PUCP research group: Dr. Andres Guerra, Dr. Rolf Grieseler, and Dr. Francisco Rumiche. Those who supported me to start research in materials science and still consider me to be part of new projects.

Thanks to the director and coordinator of the doctoral program at PUCP: Dr. Alberto Gago and Dr. José Bazo. For their support in accessing the doctoral scholarship and funds. Additionally, to the former director of the master's program in Physics, Dr. María Elena López, by

having allowed me to access my first postgraduate scholarship, and Dr. Roland Weingärtner for guiding me through the master's program and for introducing me in the exciting subject of materials science.

Thanks to my colleagues, José Angulo and Alejandro Carhuavilca, for all the experiences and knowledge that we have learned and shared on our travels. Also, thanks to Luis Herrera for helping me during all the stays in Spain.

I want to thank all my colleagues in the PV research group: Miguel Sevillano, Brando, Michael, Arturo, Wildor, Pedro, Edgar, Erick, Renzo, Ricardo, Marcos, Gerardo, Martin, Dante... Without you, the installation and correct operation of PV systems would not be possible.

Thanks to my classmates who I met during the master's degree and who shared good experiences: Nhell, Julio, Luis Pretell, Paul, Rafael, Carlos, Alvaro, Jorge, Marvin, Enrique, Loreleyn, and María del Carmen. Also, my colleagues that I met during my doctoral stage: Betty, Miguel Piñero, Estrella, Luis Sanchez, Anthony, Erick, Roger, Kevin, Zully, Fabiola, Aranselly. Lastly, I would like to thank my longtime friends whom I am still in contact: José Melgarejo, Daniel Aranda, Pedro Yllia, and Jesús Champi.

Finally, I want to thank my family for all the support and love they have always given me. Thank you for all the sacrifice you have always given for me, to make me a better professional and person to meet my goals.

Thanks to the National Council of Science, Technology and Technological Innovation (CONCYTEC) for the funds and the stipend in the framework of the doctoral scholarship program (236-2015-FONDECYT).

Thanks to the research support program for postgraduate students (PAIP 2019-PUCP), for the financial support. To the mobility grants for doctoral students (UNIA-2021) aimed at members of "La Rabida 2021" for Ibero-American universities, by the mobilization funds.

Thanks to Dr. Carlos Fosca for the seed fund of the VRAD and VRI with which the first version of the research laboratory was implemented. Acknowledgments to the additional support for the development of the laboratory by the National Fund for Scientific and Technological Development of Peru (FONDECYT) through Contract No. 124-2018-FONDECYT.

Thanks to the memory of Dr. Heinrich Berg from Delta Volt company, to CER-UNI, and the following companies: Q-Energy, Enercity and Novum Solar, for their support in the acquisition of equipment and loans of PV modules for analysis.

Finally, acknowledge the support provided by the Vicerectory of the PUCP through research activities PO0088, PI0664, and PI0737.



Resumen

Esta Tesis Doctoral contribuyó a desarrollar un nuevo laboratorio fotovoltaico (FV) en la ciudad de Lima-Perú, mediante la implementación de un sistema de caracterización para módulos FV. Este sistema permite realizar estudios de rendimiento de diferentes tecnologías FV en condiciones exteriores. Este nuevo laboratorio es el primero de su tipo en Perú debido a su instrumentación especializada para diversas investigaciones de rendimiento FV.

Este sistema fue instalado en el laboratorio de FV en los exteriores de la sección de Física ($12^{\circ}2'S$, $77^{\circ}1'O$) de la Pontificia Universidad Católica del Perú (PUCP), en colaboración con el grupo de investigación IDEA de la Universidad de Jaén (UJA) de España. Actualmente se encuentran instalados siete módulos FV de diferentes tecnologías e instrumentos para medir las condiciones ambientales. Este sistema mide la curva de corriente-voltaje (I-V) de cada módulo FV a intervalos de cinco minutos y mide simultáneamente la temperatura del módulo FV, la irradiancia, el espectro solar y las condiciones ambientales. Con estos datos experimentales, es posible realizar estudios de caracterización y rendimiento de módulos o sistemas FV.

El sistema comenzó a funcionar en marzo de 2019 y continúa funcionando automatizada hasta la fecha. Se empezaron a caracterizar tres tipos de tecnologías FV: campo de superficie posterior de aluminio (del inglés Al-BSF, Aluminum Back Surface Field), heterounión con capa delgada intrínseca (del inglés HIT, Heterojunction with Intrinsic Thin-Layer) y tándem de silicio amorfo/microcristalino (del inglés a-Si/ μ c-Si, Amorphous/microcrystalline silicon tandem). En el 2020 se instalaron cuatro tecnologías adicionales: contacto posterior interdigitado (del inglés IBC, Interdigitated Back Contact), emisor pasivo totalmente difuso posterior (del inglés PERT, Passivated Emitter Rear Totally Diffused), silicio amorfo (del inglés a-Si, Amor-

phous Silicon), y seleniuro de cobre, indio, galio (del inglés CIGS, Copper Indium Gallium Selenide).

En el segundo capítulo se describe el sistema de caracterización compuesto por un trazador de curvas corriente-voltaje (I-V), un sistema de multiplexado y los instrumentos/sensores ambientales. Se enumeran los módulos FV, instrumentos de medición, sensores, componentes para placas de circuitos y diagramas de conexión. En la subcapítulo acerca del control automatizado, se describe la arquitectura del software desarrollado en LabVIEW para la medición, visualización y almacenamiento de datos.

En el tercer capítulo se realiza un análisis de los datos extraídos de las curvas I-V, principalmente en el punto de máxima potencia. Para ello, se desarrolló una metodología de calibración de módulos FV en exteriores. Se utilizaron métodos simples, como Osterwald y factor de llenado constante (del inglés *FF_k*, fill factor constant), para modelar la potencia máxima del HIT, Al-BSF y tándem a-Si/ μ c-Si, durante tres meses (mayo 2019 - abril 2020). A continuación, se analiza la eficiencia de conversión de energía utilizando el coeficiente de rendimiento (del inglés *PR*, performance ratio) en las siguientes tecnologías FV: HIT, Al-BSF, tándem a-Si/ μ c-Si, IBC, PERT, a-Si y CIGS por dos años (marzo 2020 – febrero 2022).

En el cuarto capítulo se realiza un estudio experimental del espectro solar durante un año (marzo 2019 – febrero 2020). El espectro se caracterizó por la energía fotónica promedio (del inglés *APE*, average photon energy). Se encontró que el *APE* anual para el periodo de estudio fue de 1.923 eV, lo que indicó que el espectro en Lima tiene un corrimiento hacia el azul con respecto al espectro estándar AM1.5G. Adicionalmente, la variación del *APE* mensual durante el año es despreciable. Luego, se realizó una evaluación teórica del factor de desajuste espectral (del inglés *MM*, spectral mismatch factor) y la ganancia espectral para la respuesta espectral (del inglés *SR*, spectral response) de siete tecnologías fotovoltaicas: a-Si, Perovskita, CdTe (del inglés, cadmium telluride), dos CIGS con diferentes *SR*, multi-Si (del inglés, multicrystalline silicon) y mono-Si (del inglés, monocrystalline silicon).

En las conclusiones y trabajos futuros, se resumen los objetivos conseguidos y el estado actual del laboratorio de investigación con los nuevos sistemas e instrumentos instalados.

Finalmente, en los anexos se encuentra información adicional y mas detallada de los circuitos, algoritmos, y arreglos matemáticos que fueron necesarios para el desarrollo de la tesis.



Abstract

This Doctoral Thesis contributed to forming a new photovoltaic (PV) laboratory in Lima-Peru, by developing an outdoor characterization system for PV modules. This system enables performance studies of different PV technologies under outdoor conditions. The new laboratory is the first of its kind in Peru due to its appropriate instrumentation for various PV performance research.

This system was installed in the outdoor-PV laboratory of the Physics section ($12^{\circ}2'S$, $77^{\circ}1'W$) at the Pontifical Catholic University of Peru (PUCP) in collaboration with the IDEA research group of the University of Jaén (UJA) in Spain. Seven PV modules of different technologies, and instruments are currently installed to measure environmental conditions. This system measures the current-voltage (I-V) curve of each PV module at five-minute intervals and simultaneously measures module temperature and irradiance. Additionally, the solar spectrum and environmental conditions are measured. With these experimental data, it is possible to carry out characterization and performance studies of PV modules or systems.

The system started working in March 2019 and continues to work automatically to date. Three types of PV technologies began to be characterized: Aluminum Back Surface Field (Al-BSF), Hetero-junction with Intrinsic Thin-Layer (HIT), and Amorphous/micro-crystalline silicon tandem (a-Si/ μ c-Si). Four additional technologies were installed in 2020: Interdigitated Back Contact (IBC), Passivated Emitter Rear Totally Diffused (PERT), Amorphous Silicon (a-Si), and Copper Indium Gallium Selenide (CIGS).

The first part describes the characterization system composed of an I-V curve tracer, a multiplexing system, and environmental sensors. PV modules, measuring instruments, sensors,

components for circuit boards, and connection diagrams are listed. The automated control section describes the architecture of the software developed in LabVIEW for measurement, visualization, and data storage.

In the second part, an analysis of the data extracted from the I-V curves is made, mainly in the maximum power point. For this, a methodology was developed to calibrate the PV modules outdoors. Simple methods such as Osterwald and Constant Fill Factor (FF_k) were used to model the maximum power of HIT, Al-BSF, and tandem a-Si/ μ c-Si, for a year (May 2019 – April 2020). Next, the energy conversion efficiency is analyzed using the Performance Ratio (PR) in the following PV technologies: HIT, Al-BSF, tandem a-Si/ μ c-Si, IBC, PERT, a-Si, and CIGS for another year (March 2020 – February 2022).

In the third part, an experimental study of the solar spectrum was carried out during one year (March 2019 – February 2020). The spectrum was characterized by the Average Photon Energy (APE). It was found that the yearly APE for the study period was 1.923 eV, indicating that the spectrum in Lima has a blue shift with respect to the AM1.5G standard spectrum. Additionally, the variation of the monthly APE during the year is negligible. Then, a theoretical evaluation of the Mismatch Factor (MM) and spectral gain was made for the spectral response (SR) of seven PV technologies: a-Si, Perovskite, CdTe, two CIGS with different SRs, multi-Si, and mono-Si.

In the part of conclusions and future works, the objectives achieved and the current state of the research laboratory with the new systems and instruments installed are summarized.

Finally, in the appendixes there is more detailed additional information on the circuits, algorithms, and mathematical arrangements that were necessary for the development of the thesis.

Contents

| | |
|--|------------|
| Acknowledgments | i |
| Resumen | iv |
| Abstract | vii |
| Contents | ix |
| List of Figures | xi |
| List of Tables | xiv |
| I Introduction | 1 |
| II Measurement System Design | 9 |
| 2.1 Introduction | 9 |
| 2.2 System description | 10 |
| 2.2.1 I-V curve tracer | 12 |
| 2.2.2 Meteorological instruments | 15 |
| 2.3 Control System | 18 |
| 2.3.1 Sensor card | 18 |
| 2.3.2 Control Software | 23 |
| 2.4 Automated System Measurements | 27 |
| 2.4.1 I-V Curve measurements | 27 |
| 2.4.2 Weather measurements | 30 |
| 2.4.3 Spectral measurements | 30 |
| 2.5 Conclusions | 32 |
| III Performance evaluation and characterization | 33 |
| 3.1 Introduction | 33 |
| 3.2 Methodology | 34 |
| 3.2.1 Experimental set-up | 34 |
| 3.2.2 Calibration | 34 |
| 3.2.3 Modeling the maximum Power | 36 |
| 3.2.4 Module Performance Ratio | 38 |
| 3.3 Predicted vs. Modeled Power | 38 |

| | | |
|-----------|--|------------|
| 3.3.1 | Calibration results | 38 |
| 3.3.2 | Modeling results compared with experimental results | 39 |
| 3.4 | Module Performance Ratio results | 48 |
| 3.4.1 | Calibration results of nominal power | 48 |
| 3.4.2 | Monthly and Annual Module Performance Ratio results | 49 |
| 3.5 | Conclusions | 56 |
| IV | Spectral analysis and characterization | 58 |
| 4.1 | Introduction | 58 |
| 4.2 | Methodology | 59 |
| 4.2.1 | Extrapolation of spectra | 59 |
| 4.2.2 | Gaussian Fit | 61 |
| 4.2.3 | Angle of incidence | 62 |
| 4.2.4 | Average Photon Energy | 63 |
| 4.2.5 | Spectral Mismatch Factor | 66 |
| 4.3 | Average Photon Energy in Lima Results | 67 |
| 4.4 | Spectral Mismatch Factor for PV modules Results | 71 |
| 4.5 | Conclusions | 73 |
| V | Conclusions and Future Lines | 75 |
| | Appendix A: Complementary information of the measurement system | 81 |
| | Appendix B: Gaussian fit for Spectral Response | 91 |
| | Bibliography | 99 |
| | Publications | 111 |
| | Scientific publications indexed with relative quality index | 111 |
| | Scientific publications without relative quality index | 113 |
| | Communications in congresses with paper indexed in scopus | 114 |

List of Figures

| | | |
|------|---|----|
| 1.1 | Example of an experimental (a) I-V curve and (b) P-V curve under illumination. | 4 |
| 1.2 | I-V curve with the possible losses. | 6 |
| 2.1 | General schematic diagram of the measurement system | 10 |
| 2.2 | PV modules and measuring instruments installed on the roof | 11 |
| 2.3 | I-V tracer system | 11 |
| 2.4 | Schematic diagram of an I-V curve tracer | 12 |
| 2.5 | Phases for I-V curve tracing process. | 14 |
| 2.6 | Photography of the I-V curve tracer. | 15 |
| 2.7 | Meteorological instruments: (a) Irradiance sensors and spectroradiometer (b) Smart weather station. | 17 |
| 2.8 | Connection diagram of the sensor card | 18 |
| 2.9 | Timing diagram for I-V tracing and environmental measurements. | 19 |
| 2.10 | Schematic diagram of the Module Box | 20 |
| 2.11 | Photography of the Module Box. | 20 |
| 2.12 | Multiplexer system diagram | 21 |
| 2.13 | Photography of the Multiplexer System. | 22 |
| 2.14 | Timing diagram for eight PV modules. | 23 |
| 2.15 | State machines for Control System software. | 24 |
| 2.16 | Control interface screen capture. | 25 |
| 2.17 | Graph Tab screen capture. | 25 |
| 2.18 | Viewer Tab screen capture. | 26 |
| 2.19 | Configuration Tab screen capture. | 26 |
| 2.20 | Result of the I-V curve measurement by a capacitive load. | 27 |
| 2.21 | Measurement of (a) current and (b) voltage, as a function of time. | 28 |
| 2.22 | Incomplete I-V curve at the I_{SC} point and with partial shadow. | 29 |
| 2.23 | I-V curves under different levels of irradiance. | 29 |
| 2.24 | Variation of the air temperature, humidity and irradiance for a sunny summer day (13-Feb-2022). | 30 |
| 2.25 | Spectral distributions by hours of a sunny day in Lima. | 31 |
| 2.26 | Spectral distributions for a sunny day in Lima in an interval of five minutes. | 31 |
| 3.1 | AI-BSF Modeled Power by the method (a) Osterwald and (b) FFk. | 40 |
| 3.2 | HIT Modeled Power by the method (a) Osterwald and (b) FFk. | 41 |
| 3.3 | Tandem Modeled Power by the method (a) Osterwald and (b) FFk. | 42 |
| 3.4 | AI-BSF Modeled Power corrected by the method (a) Osterwald and (b) FFk. | 44 |

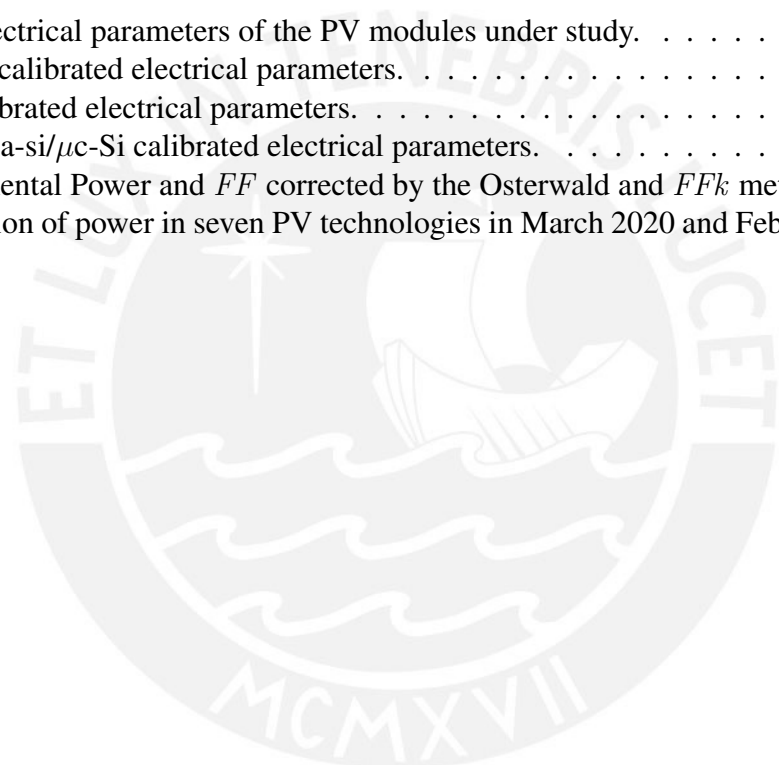
| | | |
|------|---|----|
| 3.5 | HIT Modeled Power corrected by the method (a) Osterwald and (b) FFk. | 45 |
| 3.6 | Tandem Modeled Power corrected by the method (a) Osterwald and (b) FFk. . . | 46 |
| 3.7 | (a) NRMSE and (b) NMBE, comparing the methods of Osterwald and FFk. . . | 47 |
| 3.8 | PV technologies based in c-Si: (a) PR (b) PR corrected by temperature (c) Monthly average of the module temperature and air temperature (d) Monthly average of daily irradiation. | 51 |
| 3.9 | PV technologies based in TF: (a) PR (b) PR corrected by temperature (c) Monthly average of the module temperature and air temperature (d) Monthly average of daily irradiation. | 52 |
| 3.10 | PR_{mod}^a and $PR_{mod,T \rightarrow 25}^a$ for c-Si technologies with respect to $P_{M,exp}^*$ from March 2020. | 54 |
| 3.11 | PR_{mod}^a and $PR_{mod,T \rightarrow 25}^a$ for TF technologies with respect to $P_{M,exp}^*$ from March 2020. | 54 |
| 3.12 | PR_{mod}^a and $PR_{mod,T \rightarrow 25}^a$ for c-Si technologies with respect to P_M^* in STC. . . . | 55 |
| 3.13 | PR_{mod}^a and $PR_{mod,T \rightarrow 25}^a$ for TF technologies with respect to P_M^* in STC. . . . | 55 |
| 4.1 | Shaded area between 700-1100 nm of an experimental spectrum. | 60 |
| 4.2 | Shaded area between 700-1100 nm of AM1.5G spectrum. | 60 |
| 4.3 | Resulting extrapolated experimental spectrum. | 61 |
| 4.4 | Relative spectral responses of PV modules and the normalized spectral irradiance AM1.5G. | 62 |
| 4.5 | Examples of spectral irradiance distributions measured in Lima. | 64 |
| 4.6 | Irradiance and APE for a sunny day in Lima. | 64 |
| 4.7 | Irradiance and APE for a partially cloudy day in Lima. | 65 |
| 4.8 | Irradiance and APE for a cloudy day in Lima. | 65 |
| 4.9 | Annual distribution of APE_i of about 23,000 spectra recorded from March 2019 to February 2020 as a function of APE | 68 |
| 4.10 | Daily, monthly and annual irradiance weighted APE in one year. | 68 |
| 4.11 | APE_i with respect to G_i . The APE_a and $APE_{AM1.5G}$ are indicate as reference. | 69 |
| 4.12 | Monthly and annual MM averages evaluated for different PV technologies in one year in Lima. | 70 |
| 4.13 | Correlation between the APE and MM weighted by irradiance of each PV technology with (a) daily and (b) monthly values. The APE_a is indicate as a reference. | 72 |
| 5.1 | PV Research Laboratory at PUCP. | 77 |
| 5.2 | (a) Vertical and (b) tilted, bifacial PV modules and pyranometers. | 78 |
| 5.3 | Diffuse horizontal measurement systems of the solar spectrum and irradiance. . . | 79 |
| 5.4 | Schematic diagram of the current state of the entire Outdoor-PV Laboratory. . . | 80 |
| A.1 | Photograph of I-V tracer | 81 |
| A.2 | Diagram for the I-V curve tracer | 82 |
| A.3 | PCB for the sensor card. | 83 |
| A.4 | PCB for the Box circuit. | 84 |
| A.5 | Photography of the PV Box circuit. | 84 |
| A.6 | PCB for the multiplexer circuit. | 85 |

| | | |
|-----|---|----|
| A.7 | Photography of the multiplexer system. | 85 |
| A.8 | Timing diagram for I-V tracing and environmental measurements. | 89 |
| A.9 | Flowchart of the automated software for the measurement and storage of I-V curves, solar spectrum and environmental parameters. | 90 |
| B.1 | Spectral responses for seven PV technologies. | 91 |
| B.2 | Gaussian Fit for a-Si SR. | 92 |
| B.3 | Gaussian Fit for Perovskite SR. | 93 |
| B.4 | Gaussian Fit for CdTe SR. | 94 |
| B.5 | Gaussian Fit for CIGS-2 SR. | 95 |
| B.6 | Gaussian Fit for multi-Si SR. | 96 |
| B.7 | Gaussian Fit for CIGS-1 SR. | 97 |
| B.8 | Gaussian Fit for mono-Si SR | 98 |



List of Tables

| | | |
|-----|--|----|
| 2.1 | List of meteorological instruments and sensors. | 15 |
| 2.2 | Combinations for the multiplexer circuit. | 22 |
| 3.1 | Main electrical parameters of the PV modules under study. | 34 |
| 3.2 | Al-BSF calibrated electrical parameters. | 39 |
| 3.3 | HIT calibrated electrical parameters. | 39 |
| 3.4 | Tandem a-si/ μ c-Si calibrated electrical parameters. | 39 |
| 3.5 | Experimental Power and FF corrected by the Osterwald and FF_k method . . . | 43 |
| 3.6 | Calibration of power in seven PV technologies in March 2020 and February 2021. . | 49 |



Chapter I

Introduction

In the decade, prior to the COVID-19 pandemic, the Peruvian economy had moderately grown, with an annual average GDP growth rate of 4% in 2018, being one of the most attractive economies for investors in Latin America [1]. According to studies carried out by Zambrano-Monserrate et al. [2], economic growth implies greater energy consumption.

Most of the non-renewable energy sources in Peru come from fossil fuels and the country's growing demand for electrical energy is almost supplied by hydroelectric plants and natural gas [3]. Therefore, the use of fossil fuels and natural gas implies a greater emission of greenhouse gases. For example, a World Bank report [4] shows how CO₂ emissions have increased in metric tons from 0.984 in 2003 to 1.697 in 2018.

The Peruvian government has the objective of sustainable decarbonization by 2050 with an intermediate goal in 2030. According to the energy transition plan [5] and the roadmap presented by Enel-Deloitte [6], some of its objectives are: Achieve a green energy matrix by switching to emission-free primary energy sources, promote energy efficiency nationwide and the electrification in rural regions, and the development of infrastructure and digitalization of the electricity transmission network in all areas of the country.

Rural electrification projects are being implemented in regions without access to the electricity grid. For example, in one of these projects, 200 thousand PV modules were installed for essential electricity services in houses, medical centers and schools [7]. At the end of 2018, Peru had a total of 284.5 MW of installed power based on solar energy [8]. Rubi Solar PV

plant in Moquegua is the largest in Peru until the end of 2022 and has a generation capacity of 440 GW h per year [9]. However, currently, there is a lack of knowledge of the real performance of PV technologies in the different regions of Peru since it has 38 types of climates [10].

First performance studies in Peru were conducted by R. Espinoza [11][12] and I. Romero-Fiances [13] within the framework of the project "Emerging with the sun" [14]. The performance of three different PV module technologies were analyzed: monocrystalline silicon (mono-Si), polycrystalline silicon (poly-Si) and tandem amorphous silicon/Microcrystalline silicon (a-Si/ μ c-Si), for grid-connected PV systems in Lima, Arequipa and Tacna. They reported how the performance of these PV module technologies are affected by the different climates of these cities. However, they conclude that more campaigns of characterization are necessary that also include other PV module technologies and with more complete instrumentation.

Lima is located on the east coast of Peru ($12^{\circ}2'S$, $77^{\circ}1'W$) with a climate categorized as "Hot-Arid Desert" [15]. It is one of the largest cities in South America and has a population of 10 million people. Most Peruvian industries and businesses are located here; hence, it has the highest energy and electricity consumption in the country. However, the environmental conditions in Lima (intermediate ambient temperature, high humidity, and partially cloudy irradiation) are very different from those in other temperate climates, where the performance of PV modules is widely reported [16].

Therefore, it is essential to fill the knowledge gap on the performance of PV modules in coastal, desertic climates like this. This information can provide constructive advice to system integrators and investors to determine which type of PV module technology offers the best performance under these given conditions.

The general objective of this thesis is to understanding the performance behavior of PV technologies in Lima-Peru through implementing an Outdoor-PV Laboratory at the PUCP, suitable for characterizing, calibrating, and monitoring commercial PV modules in outdoor conditions.

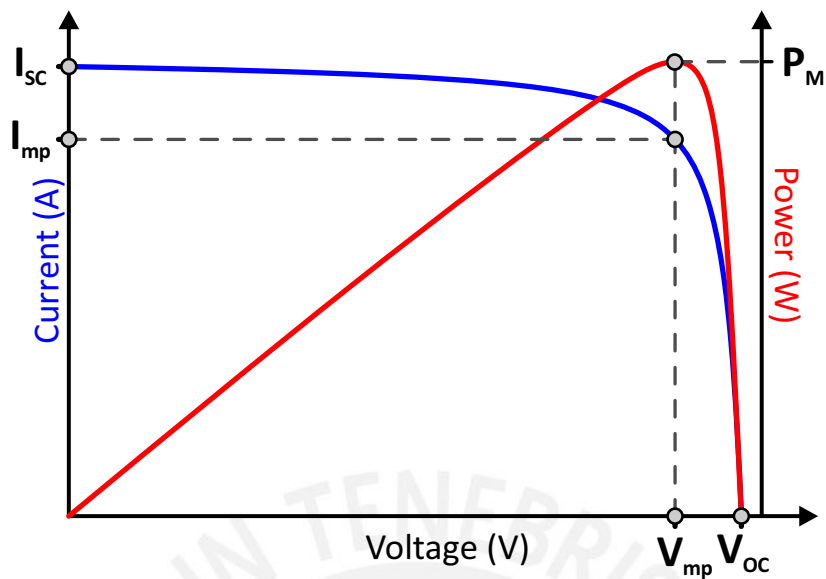
To achieve the general objective, the following specific objectives were set:

- Design and implement a system for the characterization and calibration of PV modules of different outdoor technologies in the Physics Section of the PUCP.
- Validation of the characterization system by applying simple models to the experimental data to verify the correct functioning of the system.
- Modeling electrical behavior outdoors of different PV module technologies and contrasting with experimental data.
- Evaluation of the results with respect to the literature and reports from locations with similar climatic conditions.

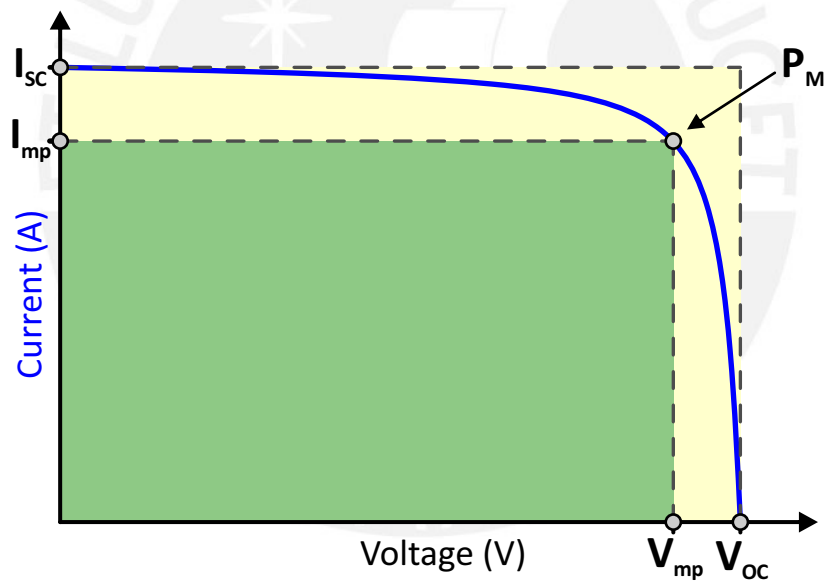
Manufacturers categorize PV modules in "Standard Test Conditions" (STC) according to IEC 60891 [17] and that allow a comparative reference for PV devices. These are: Normal irradiance of 1000 W m^{-2} , constant cell temperature of $25 \text{ }^\circ\text{C}$, and spectral distribution of AM1.5. In addition, with the electrical parameters in STC, the price of the PV modules are established, and therefore, the price and the generation capacity of the PV installations.

However, STC conditions rarely occur in outdoors conditions, so the outdoor PV modules' performance is greatly influenced by different environmental conditions [18]. The energy performance of photovoltaic systems depends mainly on the incident irradiance and the operating temperature, and whose effects on performance are well known [17][19][20]. But it is also affected by the spectral distribution, low irradiance levels, soiling, angle of incidence (AOI), degradation, and system failures [21]. For example, the spectral effects have been scarcely experimentally evaluated in different locations with diverse climates due to the necessary specialized, expensive instrumentation that requires continuous maintenance and regular calibration.

The experiment that provides the most information on the behavior of a PV module is the measurement of the I-V curve. There are several methods to measure the I-V curve, such as: Variable resistor, capacitive load, electronic load, DC-DC converter, and power supply [22].



(a)



(b)

Figure 1.1: Example of an experimental (a) I-V curve and (b) P-V curve under illumination.

Although there are different commercial I-V curve tracers, these tracers often are not suitable for an extensive experimental campaign as they are limited to the manufacturer's specifications for the PV generator, sensors, and software. That is why different laboratories have developed their own I-V curve tracers, adapting with respect to their measurement instruments/sensors and climatic conditions. For example, the Laboratory of Photovoltaics and Optoelectronics

of the University of Ljubljana developed a monitoring system that has the ability to measure all the main performance parameters of photovoltaic modules (I-V curve, power, current and voltage at the MPP point, open-circuit voltage, short-circuit current, efficiency, ...) in various climatic conditions [23].

The measurement system for I-V curves of PV modules developed in this thesis works with a capacitive load. This allows for fast current and voltage sweeps that minimize errors caused by constantly changing environments. The design and implementation are based on the following publication [24] from the IDEA research group of the University of Jaén (Spain).

Figure 1.1 shows a PV module's experimental I-V curve (blue line) under illumination. When the values of I and V are multiplied, the Power-Voltage (P-V) curve (red line) is obtained. From the I-V curve, the following PV parameters can be extracted:

Maximum power point (P_M): Is the point located at the *knee* of the I-V curve, where the solar cell works with maximum power.

Short-circuit current (I_{SC}): The PV module's maximum current under illumination at $V = 0$. It is linearly dependent on solar irradiance and is not strongly temperature dependent. It tends to increase slightly with increasing module temperature.

Open-circuit voltage (V_{OC}): The PV module's maximum voltage occurs when the current is zero ($I = 0$). The V_{OC} is mainly affected by the temperature and logarithmically by the irradiance.

Fill factor (FF): It represents the curvature of the I-V curve. In Figure 1.1b it is the ratio of two areas in the I-V curve formed by $I_{mp} \cdot V_{mp}$ and $I_{SC} \cdot V_{OC}$. The FF is expressed by

$$FF = \frac{I_{mp}V_{mp}}{I_{SC}V_{OC}} \quad (1.1)$$

The FF is a measure of the quality of the cell and varies between cell technologies. From 0.75 to 0.85 for crystalline silicon cells and from 0.55 to 0.75 for most thin-film cells. The FF can also be reduced by various kinds of PV degradations [25].

Efficiency (η): It is defined as the ratio of P_M and the incident solar power on the cell (P_i):

$$\eta = \frac{P_M}{P_i} = \frac{P_M}{G_i A} \quad (1.2)$$

Where P_i is equal to the incident irradiance at an instant (G_i) multiplied by the area A . Currently, efficiencies for crystalline silicon cells are between 14 % and 27 %. While those of thin film reach a maximum of 24 % [26].

When a deeper analysis of the performance and anomalies of a PV module or PV array is required, the measurement of the I-V curve provides qualitative and quantitative information on the state of the installation. The continuous measurement of the I-V curve in an extensive experimental campaign allows for obtaining data on the behavior of the PV module in different irradiance levels, temperatures, and spectral distributions and identifying possible losses [25].

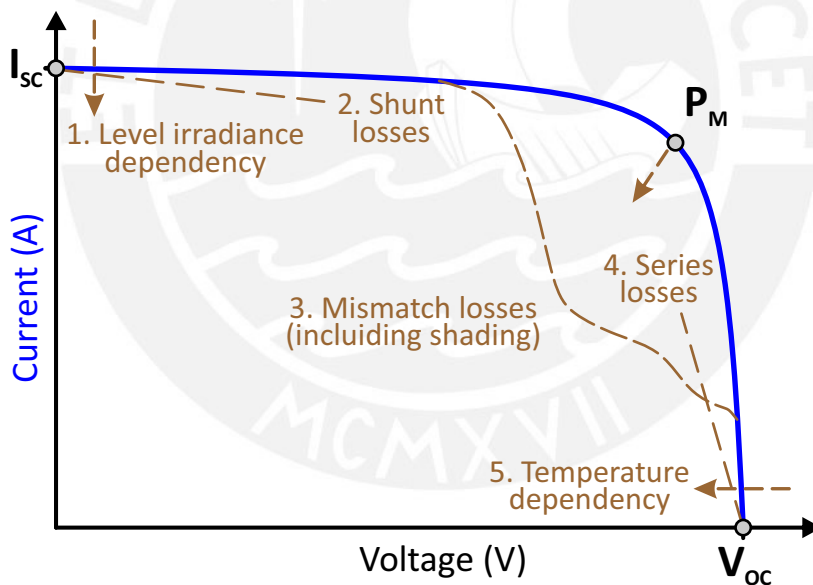


Figure 1.2: I-V curve with the possible losses.

Figure 1.2 shows an I-V curve with the possible losses reflected in the curve's shape: (1) Irradiance levels cause the I_{sc} to shift in height on the y-axis. (2) Losses due to shunt resistances produce the tilt towards the x-axis. (3) Losses due to spatially inhomogeneous irradiance on the module surface, which can be caused by partial shadowings, inhomogeneous dirt accumulation, and mismatch between cells, can be identified as steps or kinks in the I-V curve where the bypass

diodes are activated. (4) Losses due to series resistances cause the tilt towards the y-axis. (5) The variation in temperature causes the V_{OC} to shift along the x-axis.

To evaluate different PV installations, procedures for measuring and calculating parameters in conjunction with performance metrics were established according to the IEC 61724 standard [27]. These procedures' parameters and metrics characterize energy production, productivity rates, losses, and overall system efficiency [28]. Such performance parameters and metrics also allow the comparison of different PV generators that may vary in design, size, technology, or location [29].

In order to describe the measurement system and performance analysis, this Doctoral Thesis has been structured in five chapters and three annexes are presented, which are described below.

Chapter 2 describes the design, implementation, and software for the Automated Measurement System for I-V curves. The content of this chapter was published in the article "Implementation of a Laboratory for the Outdoor characterization of Photovoltaic Technologies under the climatic conditions of Lima" in *Tecnia* 2019 [30].

Chapter 3 presents the results of the analysis and study of the experimental characterization of the behavior of PV modules of different technologies under the climatic conditions of Lima. The content of this chapter was published in the proceeding "Performance evaluation and characterization of different photovoltaic technologies under the coastal, desertic climate conditions of Lima, Peru" of the ISES Solar World Congress 2019 [31]. An extension of this study was published in "Monitoring versus prediction of the power of three different PV technologies in the coast of Lima-Peru" in *Journal of Physics: Conference Series* 2021 [32].

Chapter 4 analyzes ground-based experimental spectral irradiance data taken with a spectroradiometer during one year (March 2019-February 2020) and studies the influence that the spectrum exerts on the performance of different PV module technologies. The content of this chapter was published in the article "Spectral effects on the energy yield of various photovoltaic technologies in Lima (Peru)" in *Energy* 2021 [33].

Chapter 5 highlights the main conclusions and contributions after completing of this Doctoral Thesis. In the same way, the main lines of future research that will allow continuing with the work developed are presented.

Appendix A provides additional information on the design and control of the measurement system described in chapter 2. Appendix B details the Gaussian fitting that was necessary for the spectral analysis in chapter 4.

The Bibliographical References of the Doctoral Thesis are arranged in order of appearance.

The results of this thesis were presented at national and international conferences, and published in indexed journals. A list of the publications derived from this thesis is given in the final section.



Chapter II

Measurement System Design

2.1 Introduction

This chapter presents the measurement system's design, implementation, and programming. The system is able to measure the I-V curve to 16 different PV modules consecutively, with a time interval of five minutes for each PV module. Simultaneously, the global horizontal and tilted irradiance is recorded with spectral distribution and weather data (air temperature, relative humidity, ambient pressure, air density, wind speed, and wind direction) [30].

The system is located at the facilities of the MatER-PUCP research group in the Physics Section of the PUCP on the east coast of Lima ($12^{\circ}4'S$, $77^{\circ}4'W$). This system was developed in collaboration with the IDEA research group of the UJA [24], so its components and uncertainty analysis have already been analyzed [34]. This system was adapted and expanded in hardware and software to Lima's climatic conditions and to include the largest number of PV modules and measurement instruments. The experimental campaign began its installation and testing phase in January 2019 and began to fully operate in May 2019.

2.2 System description

The general scheme of the system is shown in Figure 2.1. The system is divided into two parts: On the roof are installed the PV modules, the multiplexing system, and the meteorological instruments (Figure 2.2). The I-V curve tracer, the two multimeters that measure current and voltage, the monitoring PC, and the power supplies for the meteorological instruments are installed in the laboratory (Figure 2.3).

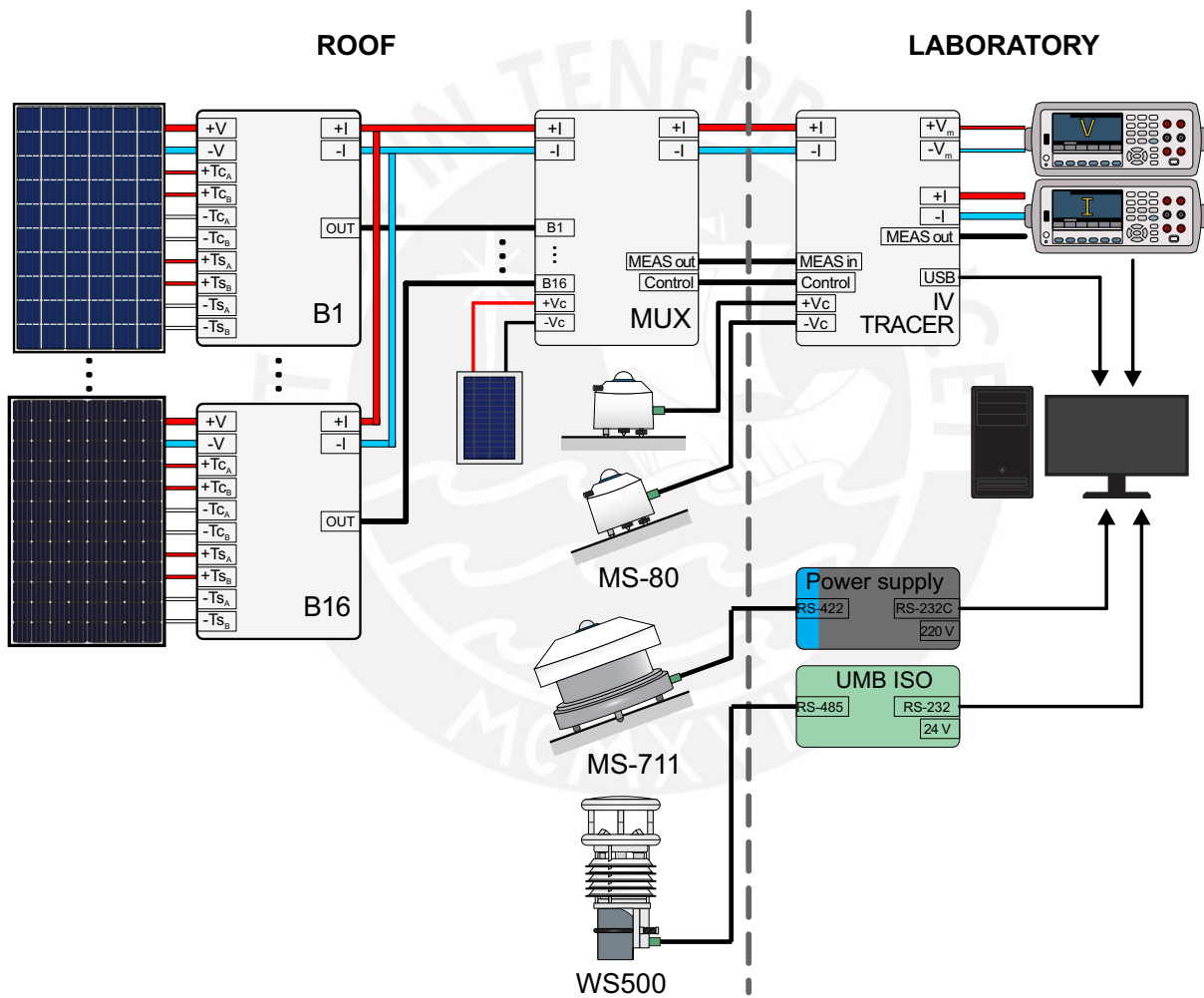


Figure 2.1: General schematic diagram of the measurement system.



Figure 2.2: PV modules and measuring instruments installed on the roof.



Figure 2.3: I-V tracer system.

2.2.1 I-V curve tracer

Figure 2.4 shows the schematic diagram of an I-V curve tracer based on a capacitive load (C) for a PV module [35]. PV module voltage and current are measured using two digital multimeters, M_V and M_I . The multimeters are in a four-wire configuration to avoid errors due to voltage drop produced by the connections' resistance. The voltage is measured parallel to the load circuit. The current is determined by relating it to the voltage drop across the shunt resistor (R_{sh}). The operation consists of three phases: pre-charge, charge, and discharge of the capacitive load [36]. R_1 and R_2 are relays that allow the charge phase. P is a button, and V_p is a negative voltage source for the pre-charge phase. R_3 and R_4 are relays, and R_d a resistor for the discharge phase.

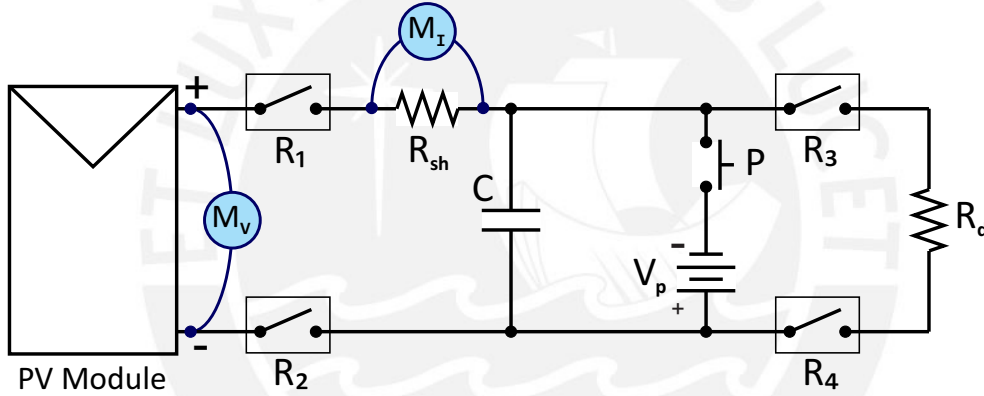


Figure 2.4: Schematic diagram of an I-V curve tracer.

The main drawback in tracing the I-V curve is the uncertainty in determining the charging time (t_c) [ms]. The relationship between t_c , the capacitance of C [F], and instantaneous values of I_{SC} and V_{OC} can be approximated by [37]:

$$t_c = \frac{V_{OC}}{I_{SC}} C \quad (2.1)$$

V_{OC} and I_{SC} are calculated with the following equations:

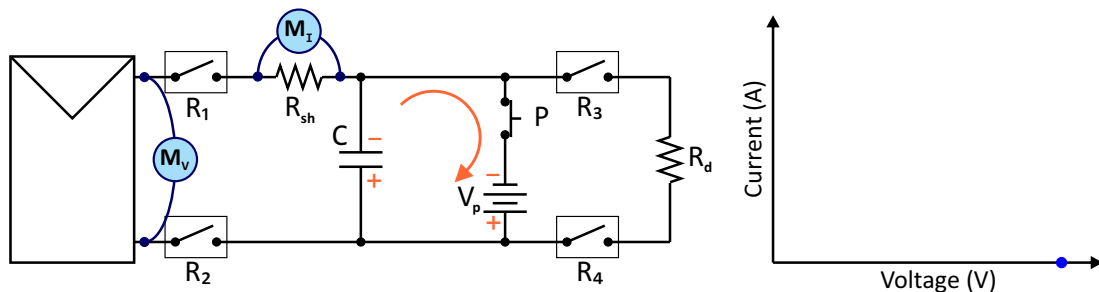
$$V_{OC} = V_{OC}^* - \beta (T_m - 25) \quad (2.2)$$

$$I_{SC} = I_{SC}^* \frac{G_i}{1000} (1 + \alpha (T_m - 25)) \quad (2.3)$$

Where V_{OC}^* and I_{SC}^* are the electrical parameters in STC, β is the temperature coefficient of the V_{OC} , α is the temperature coefficient of the I_{SC} , G_i is the incident irradiance, and T_m is the module temperature.

Figure 2.5 shows all the phases for the I-V curve tracing process. The two multimeters M_I and M_V measure I and V simultaneously over time. The corresponding I-V pairs are plotted on the right side of the figure 2.5.

First, the capacitor is disconnected and discharged, as indicated in Figure 2.4. When P closed, the capacitor is connected directly with the negative source voltage (Figure 2.5a). This ensures that the measurement passes through the I_{SC} point. At the instant that the R_1 and R_2 relays close, the charging phase starts (Figure 2.5b). The current entering the capacitor and measured by M_I is maximum and equivalent to I_{SC} . During the subsequent charging time of the capacitor (Figure 2.5c). The current will start to decrease while the voltage will increase. When the capacitor charging time is exceeded, the I-V tracing is completed. The current will not flow and will be equal to 0, and the same time, the voltage will be maximum and equivalent to the V_{OC} of the PV module (Figure 2.5d). Finally, in the discharge phase, the R_3 and R_4 relays are closed so that the discharge resistor R_d consumes the energy stored in the capacitor (Figure 2.5e).



(a) Pre-charge phase.

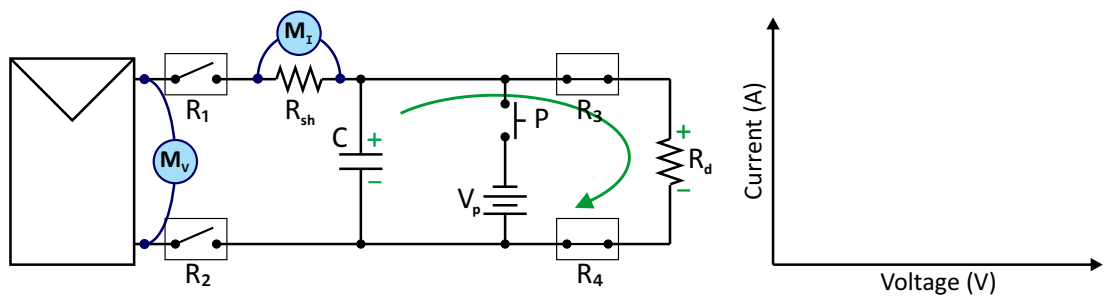
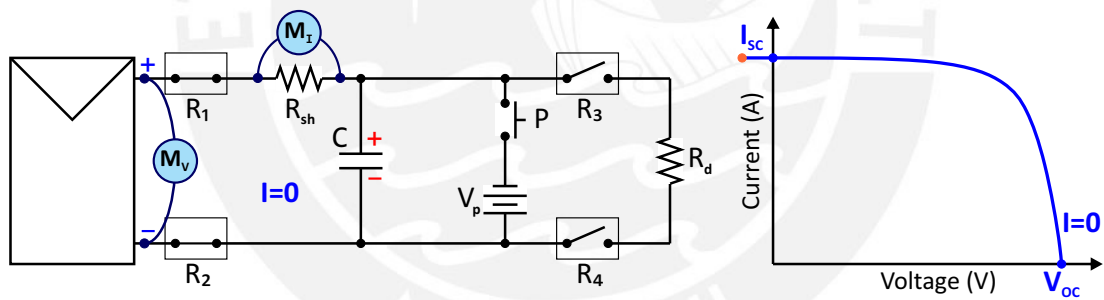
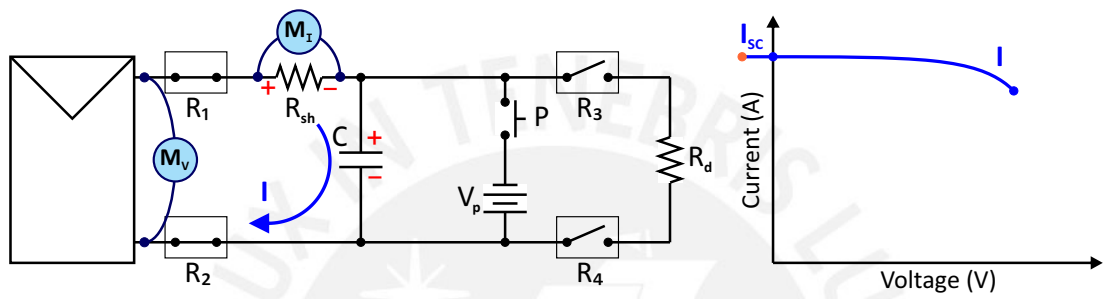
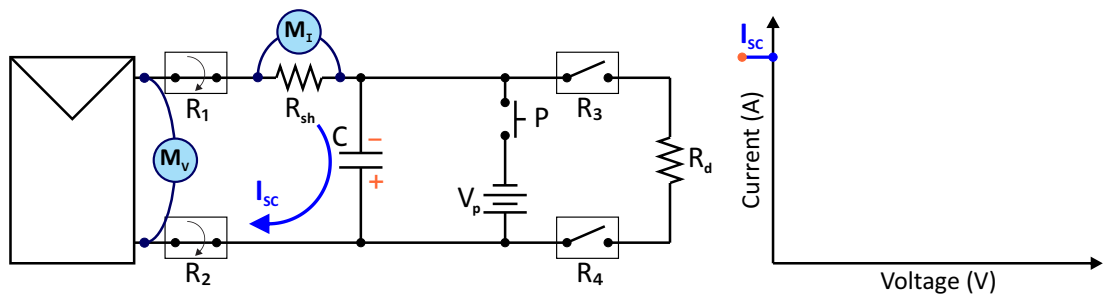


Figure 2.5: Phases for I-V curve tracing process.

Figure 2.6 shows a photograph of the I-V tracer installed in the MatER group laboratory. Component and circuit diagrams are shown in Appendix A.



Figure 2.6: Photography of the I-V curve tracer.

2.2.2 Meteorological instruments

The installed meteorological instruments are shown in Table 2.1. The irradiance sensors are shown in Figure 2.7a. One EKO MS-80 pyranometer facing north measures the global tilted irradiance (GTI) at 20° , in the plane-of-array, and another EKO MS-80 pyranometer at 0° measures the global horizontal irradiance (GHI). The EKO MS-711 spectroradiometer is installed inclined at 20° to the north. There is also a 5 W calibrated cell at an inclination of 20° and facing north.

Table 2.1: List of meteorological instruments and sensors.

| Measurement | Device | Model | Manufacturer |
|------------------------------|----------------------|---------|--------------|
| Global tilted Solar Spectrum | Spectroradiometer | MS-711 | EKO |
| Global tilted Irradiance | Calibrated Cell | 9148445 | PV-LOGIC |
| Global tilted Irradiance | Analogic Pyranometer | MS-80 | EKO |
| Global horizontal Irradiance | Analogic Pyranometer | MS-80 | EKO |
| Weather | Smart Sensor Station | WS500 | Lufft |

The tilted and horizontal EKO MS-80 pyranometers have a sensitivity constant of $10.52 \mu\text{V}$ and $10.73 \mu\text{V}$, respectively. Both have an expanded uncertainty of 0.63 %, according to the manufacturer's calibration certificate. The pyranometers use a thermopile sensor with a single glass dome and have the advantage of no need for thermal compensation and a fast response [38]. A voltage signal is generated when there is a temperature difference between the inside and the outside shell of the pyranometer. If the voltage signal is multiplied by the sensitivity constant, the irradiance value is obtained.

The EKO MS-711 spectroradiometer is suitable for working in different climates and with a wavelength range of 300-1100 nm and a wavelength interval of 0.3~0.4 nm with a spectral resolution $< 7 \text{ nm}$. According to the manufacturer's calibration certificate, the expanded uncertainties of the spectroradiometer in the 300-350 nm, 350-450 nm, 450-1050 nm, and 1050-1100 nm wavelength ranges are $\pm 17.4 \%$, $\pm 5.1 \%$, $\pm 4.2 \%$, $\pm 5.3 \%$, respectively, and the wavelength precision is $\pm 0.2 \text{ nm}$. These spectroradiometer models work by separating light into wavelengths using a diffraction grating or prism [39].

The calibrated cell is short-circuited with a high-precision resistor so that a voltage measurement corresponds directly to the irradiance value. For specific investigations, calibrated cells or modules can be more suitable for irradiance measurements than a pyranometer because their spectral and angular responses are similar to a PV module. However, if the purpose of a study is to compare different PV technologies, a device-independent sensor with a spectrally flat response, such as a pyranometer, could be more suitable [40].

Weather Smart Sensor Lufft SW500 is shown in Figure 2.7b. Air temperature is measured by a highly accurate NTC resistor, while humidity is measured using a capacitive humidity sensor. Absolute air pressure is measured by a built-in sensor (MEMS), and relative pressure is calculated from the location's altitude. Air density is calculated from the measured air temperature, humidity, and air pressure values. The wind gauge uses four ultrasonic sensors that take cyclic measurements in all directions. The resulting wind speed and direction are calculated from a sound differential [41].



(a)



(b)

Figure 2.7: Meteorological instruments: (a) Irradiance sensors and spectroradiometer
(b) Smart weather station.

2.3 Control System

The Control System consists in three parts: sensor card, multiplexing system, and the control software. The main component of the Control System is an Arduino Mega 2560, a development board based on the ATmega2560 microcontroller. Arduino digital outputs (A1, . . . , A54) control the multiplexers, relays, optocouplers, and the multimeters trigger.

2.3.1 Sensor card

The sensor card allows the connection of the Keysight 2 multimeter to the different sensors. Figure 2.8 shows the connection diagram of the sensor card. The PV module voltage is connected directly to the Keysight 1 multimeter. The current, irradiance, and temperature are individually measured with the Keysight 2 multimeter by activating a digital output (A6, A7, A8, A9, A10, A11). The pyranometers, calibrated cell, and shunt resistor are connected in a 2-wire configuration. Instead, the temperature measurements by the Pt100 IEC751 class B RTD sensor are derived from a difference in resistance in a 4-wire configuration. The multimeters' external trigger (A5) enables the simultaneous current and voltage measurements.

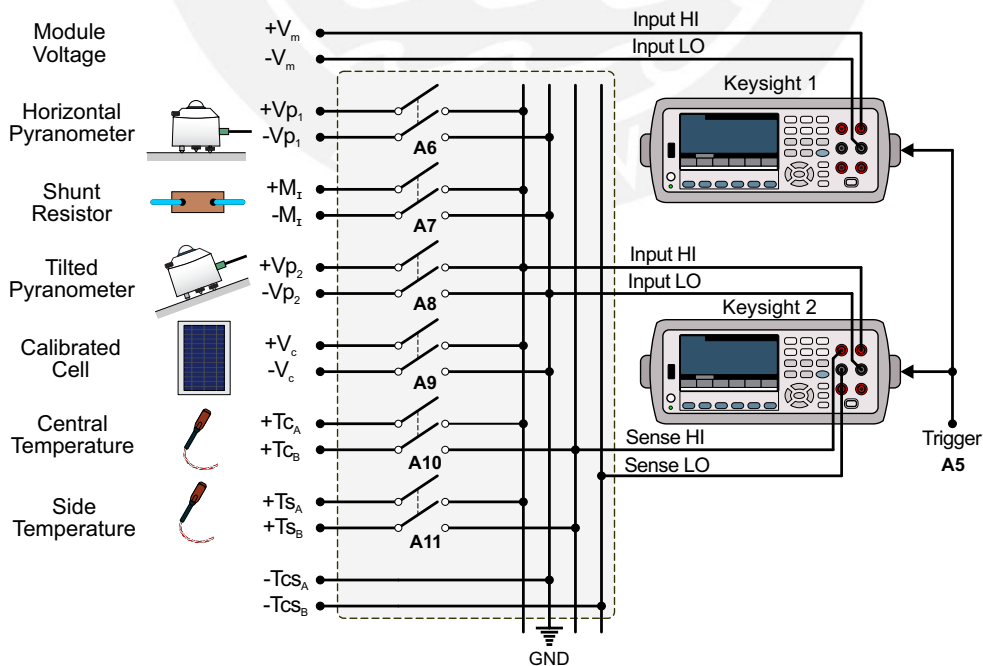


Figure 2.8: Connection diagram of the sensor card.

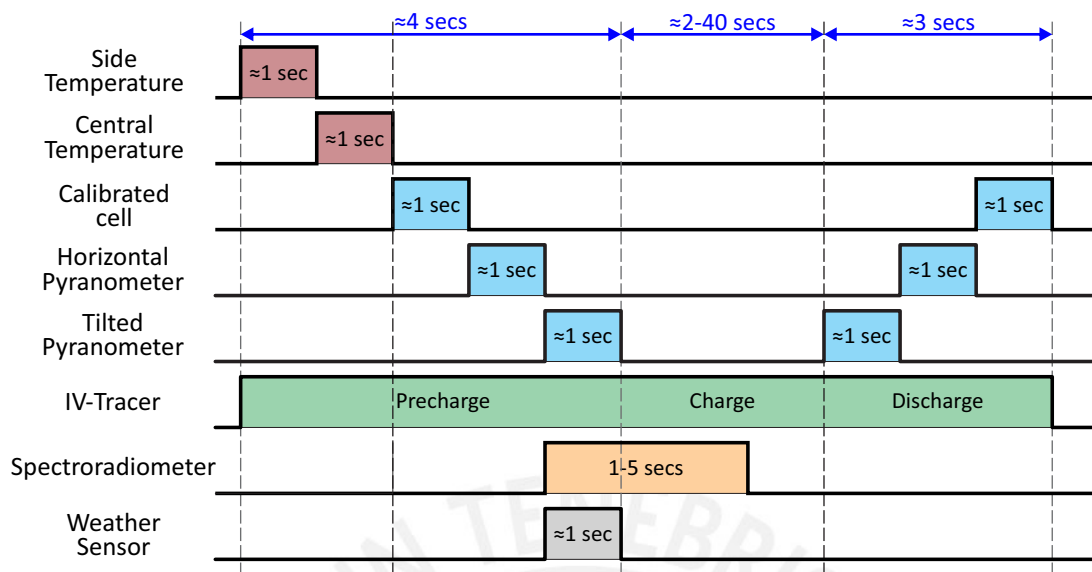


Figure 2.9: Timing diagram for I-V tracing and environmental measurements.

The timing chart in Figure 2.9 shows the measurement order of the instruments for tracing the I-V curve. Irradiance and temperature measurements with the Keysight 2 have to be performed sequentially while the measurements of the spectrum and the environmental conditions are independent.

The pre-charge phase of the capacitive load is carried out when the module temperatures and irradiance are measured within a period of about 4 seconds. The measurements of the spectrum and of the environmental conditions are made simultaneously with the inclined pyranometer measurement. The duration of the spectral measurements also depends on the irradiance level and ranges between 1 and 5 seconds at high and low levels, respectively.

The charging time is estimated with the temperature and irradiance data (Equation 2.1). During the charging phase, the current and voltage of the I-V curve are measured. The I-V tracing duration is between 2 and 40 seconds, depending on irradiance levels and the technology-dependent module currents. At high irradiance levels, the I-V tracing is quickest. Finally, in the discharge phase of about 3 seconds, the irradiance of the pyranometers is measured in parallel. All measurement data is stored in a local file.

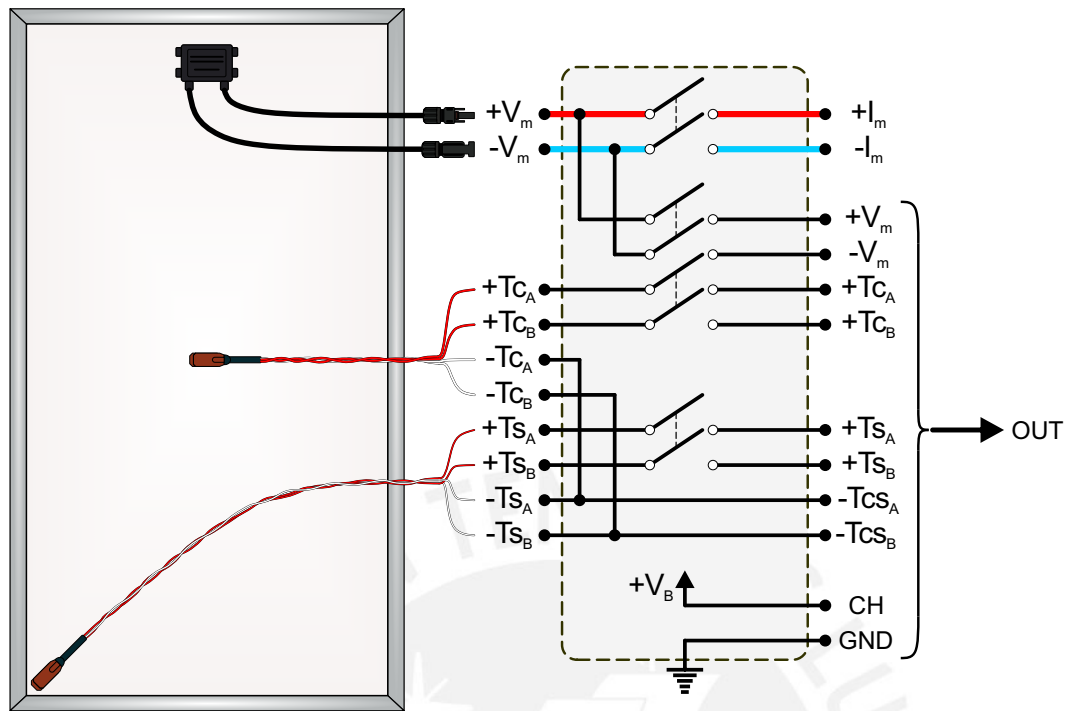


Figure 2.10: Schematic diagram of the Module Box.

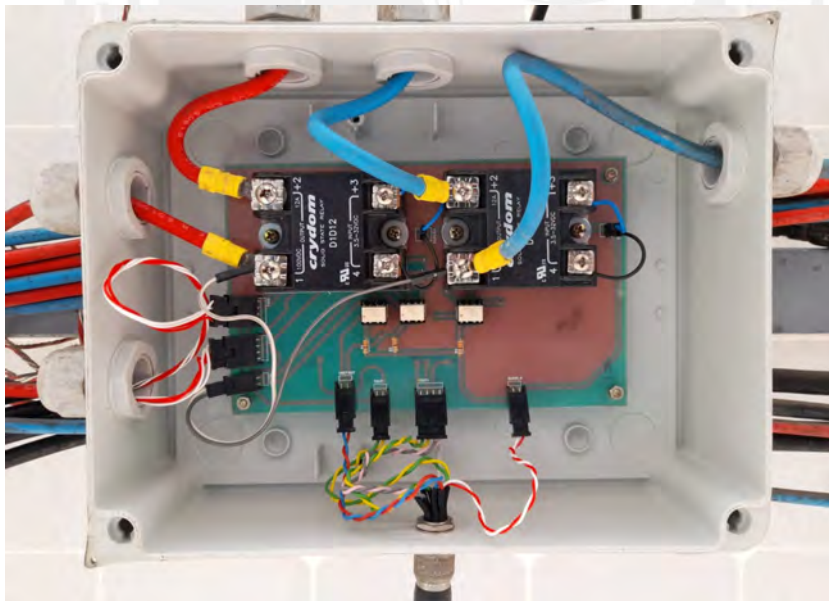


Figure 2.11: Photography of the Module Box.

For I-V curve measurement of multiple PV modules, a module box (B1, B2... B16) was implemented and installed to each PV module. The Module Box allows the selective passage of measuring the voltage and temperature of each PV module ($+I_m$, $-I_m$, and Meas Out). Fig-

Figure 2.10 shows the connection diagram of a Module Box. The PV Modules are connected to the $+V_m$ and $-V_m$ terminals. Two Pt100s are attached to the center and to the side of the PV module rear face. Each Pt100 has four terminals ($+T_A$, $+T_B$, $-T_A$, $-T_B$). When the Module Box is activated, the relays close and connect the selected PV module to the I-V tracer. $+I_m$ and $-I_m$ carry the PV module current while $+V_m$ and $-V_m$ is taken as reference for the voltage difference measurement. The positive terminals of the center and side Pt100 ($+T_{CA}$, $+T_{CB}$, $+T_{SA}$, $+T_{SB}$) are connected directly while the negative terminals are merged ($-T_{CSA}$, $-T_{CSB}$). The Figure 2.11 shows a photograph of a PV box.

Each box's activation is done by a multiplexer system (MUX 1x16). The advantage is that up to 16 PV modules with five wires (S0, S1, S2, S3, and E) can be controlled. Also, since the internal circuit has its own power source, voltage drops due to the distance between the laboratory and the station can be avoided. In the scheme of the multiplexer system of Figure 2.12, box B2 is activated. Figure 2.13 shows a photograph of the multiplexer system.

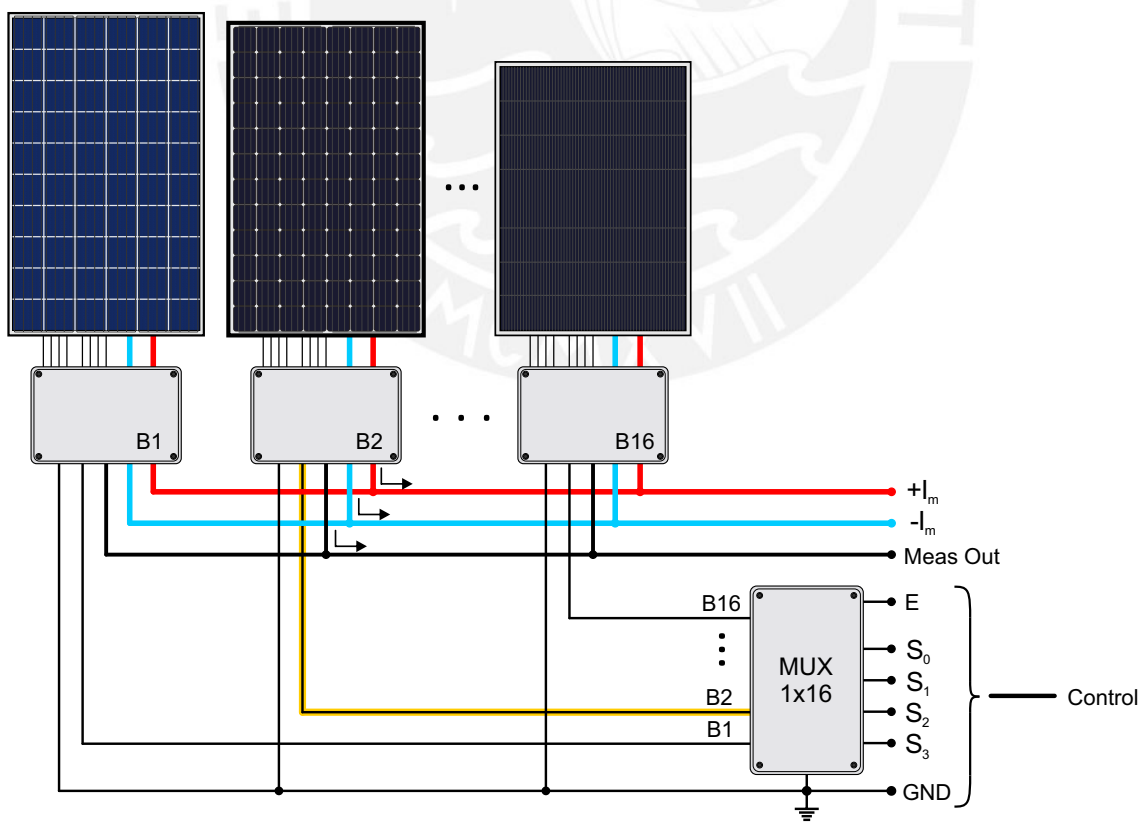


Figure 2.12: Multiplexer system diagram.

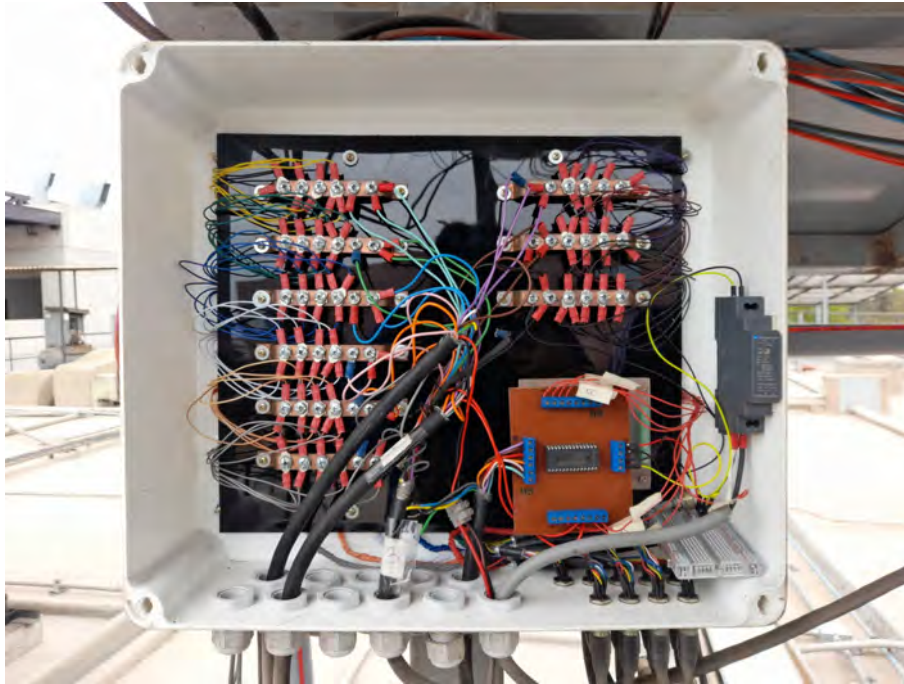


Figure 2.13: Photography of the Multiplexer System.

Table 2.2 shows the necessary combinations for the activation of each control box; 0 and 1 represent the logic voltages of 0 V and 5 V, respectively. Enable (E) is to activate or deactivates the multiplexer. The combinations of S3, S2, S1, and S0 values select the box to be activated (B1, B2, ..., B16). For example, to activate Box B2 (marked in orange), set E and S0 to 1.

Table 2.2: Combinations for the multiplexer circuit.

| INPUT | | | | | OUTPUT |
|----------|----------|----------|----------|----------|-----------|
| E | S3 | S2 | S1 | S0 | B |
| 1 | 0 | 0 | 0 | 0 | B1 |
| 1 | 0 | 0 | 0 | 1 | B2 |
| 1 | 0 | 0 | 1 | 0 | B3 |
| 1 | 0 | 0 | 1 | 1 | B4 |
| ⋮ | ⋮ | ⋮ | ⋮ | ⋮ | ⋮ |
| 1 | 1 | 1 | 1 | 0 | B15 |
| 1 | 1 | 1 | 1 | 1 | B16 |
| 0 | - | - | - | - | - |

Figure 2.14 shows the timing diagram for measuring eight PV modules in a five-minute cycle. This cycle will be repeated during all measurement hours. Each rectangle represents an

I-V curve tracing process that was shown in Figure 2.9. Blue and purple rectangles represents the c-Si and thin-film PV technologies, respectively. To maximize the amount of PV module measurements and based on preliminary tests, a fixed time was established for each one. This time is the time required for the process of tracing the I-V curve in the worst conditions (low irradiances). Longer times were set for thin-film than for c-Si PV technologies.

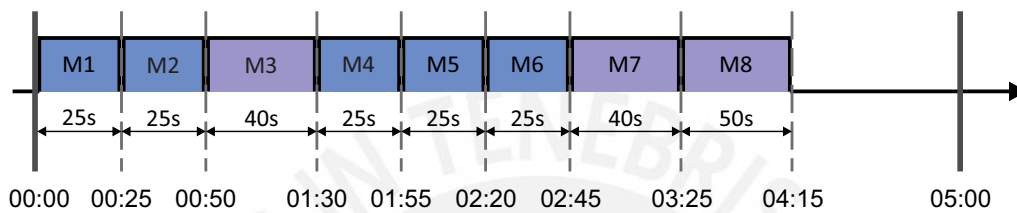


Figure 2.14: Timing diagram for eight PV modules.

2.3.2 Control Software

For the development of the system software in LabVIEW, a design platform known as State Machines was used [42]. Mainly five main states are implemented: INIT, MAIN, MEAS, ERROR and CLOSE. Figure 2.15 shows the state machine diagram used in the Control System. The INIT runs first, the configuration data is loaded, and all devices are initialized. If there is no error in the initialization, it will go to the MAIN state. The MAIN state is where the application will wait for any measurement requests. If a measurement is executed, the MEAS state is passed. All instruments start to work and the measurement results are displayed. When the measurement process is finished, the data is stored and it returns to the MAIN state. If an error is detected in any state, it will go to the ERROR state. The ERROR state stops the instruments, clears all errors found, and goes to the INIT state to restart all instruments. Finally, when it is required to stop the system correctly, it goes to the STOP state. In this state, the instruments are stopped and the data is reset to the default value.

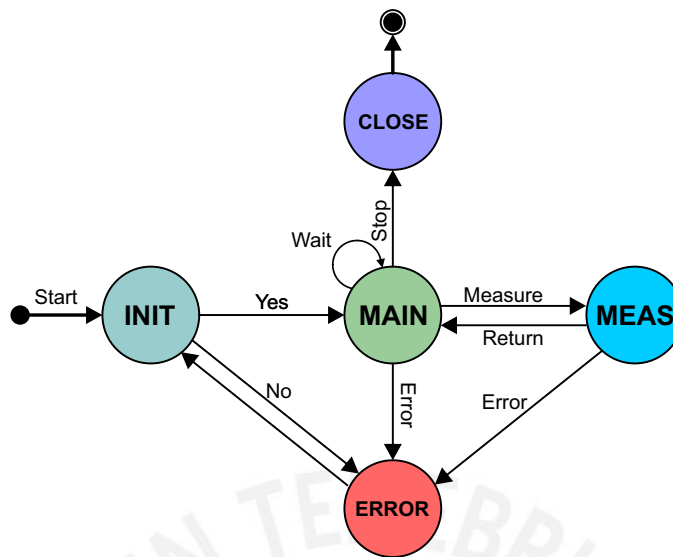


Figure 2.15: State machines for Control System software.

Figure 2.16 is a screen capture of the control interface. The left part shows the main indicators and controls. The central part shows the graphic results of the measurement, and the right part shows the numerical results of the measure. The section marked with number 1 shows the Connection section; each instrument has a box where serial port communication can be selected. If the box is colored green color, the instruments were initialized correctly; instead, they will be colored by red color. Section number 2 is the Test section. There are three buttons: the MEASURE button is to execute a I-V curve measurement process, the SAVE button is to save the previous measurement, and the STOP button is to stop the system and all instruments properly.

Figure 2.16 shows a measurement of an I-V curve with the environmental data and the solar spectrum. The Status section is section 3, shows the program's status (for example, when the program is starting, ready, measuring or error), the time, and the last measurement. Section number 4 is the Station section, where the button will activate the automatic measurements. There is a time filter for the active hours' range (Start and Final time), a minimum irradiance for the IV curve tracing, and the interval in seconds of the measurement cycle.

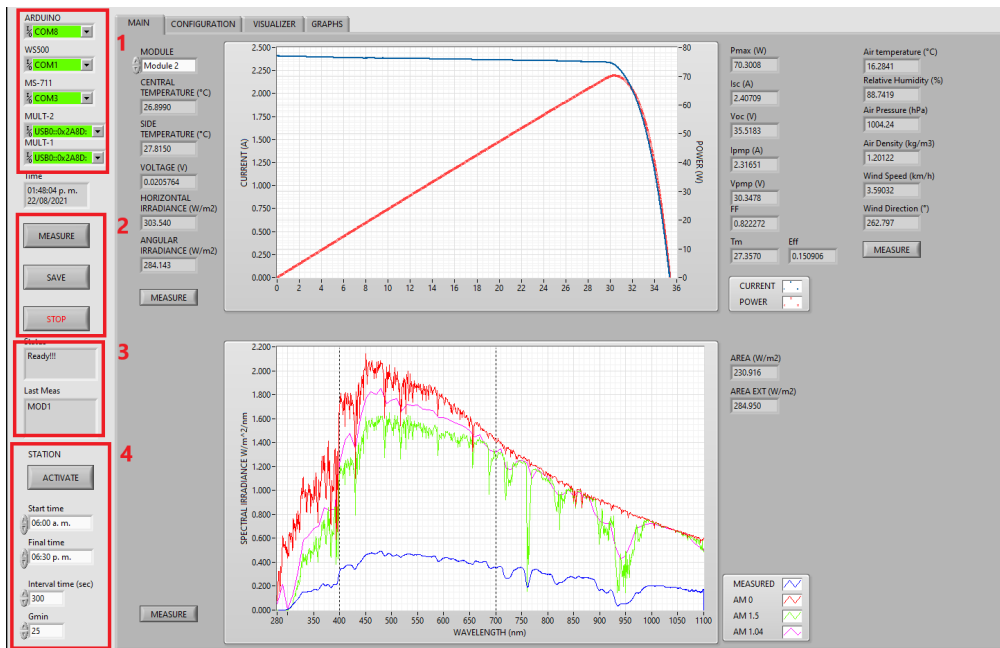


Figure 2.16: Control interface screen capture.

Figure 2.17 is a screenshot of the Chart tab. This section shows the historical data stored during the day, such as the air temperature, the measured irradiance or the maximum power generated by each module.

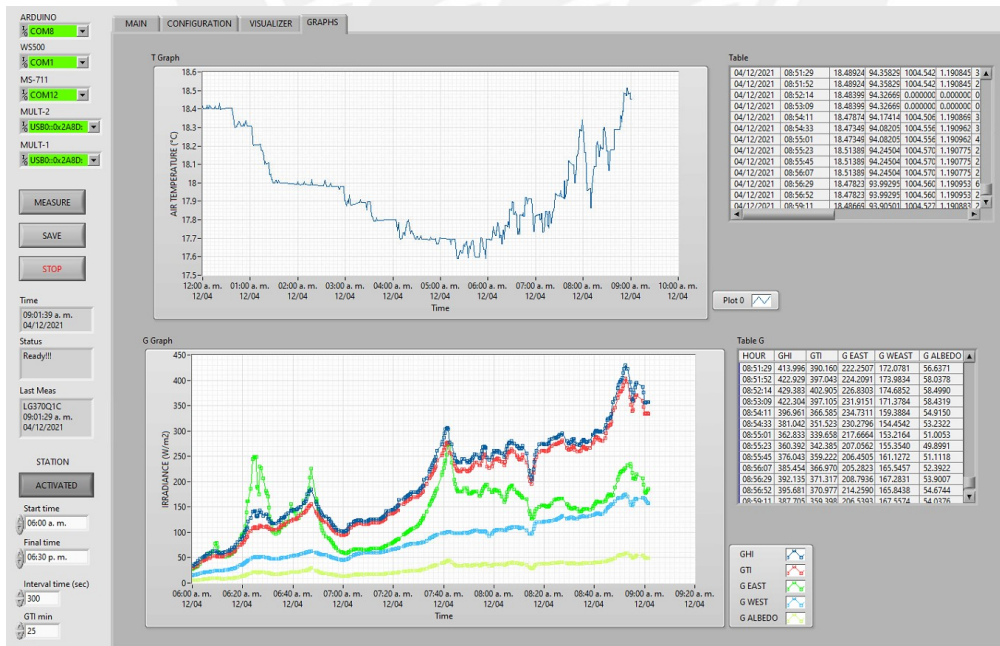


Figure 2.17: Graph Tab screen capture.

Figure 2.18 shows the Viewer tab. In this section, a saved I-V curve file can be loaded and displayed along with the solar spectrum and environmental variables.

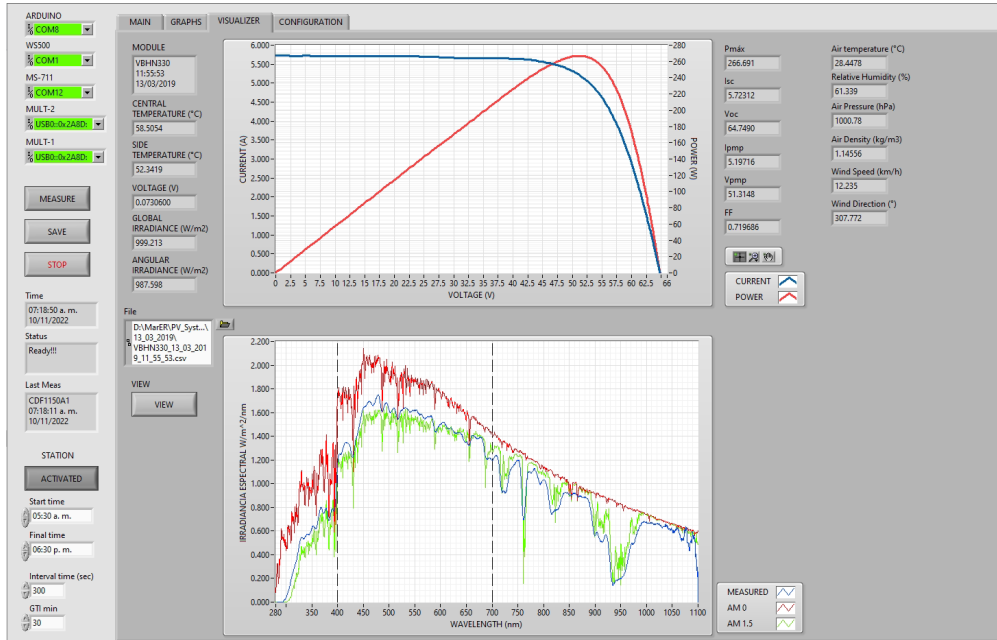


Figure 2.18: Viewer Tab screen capture.

Figure 2.19 shows the Configuration Tab. The tab contains a table where the data of the PV modules are entered and are extracted by the software for the correct tracing of the I-V curve.

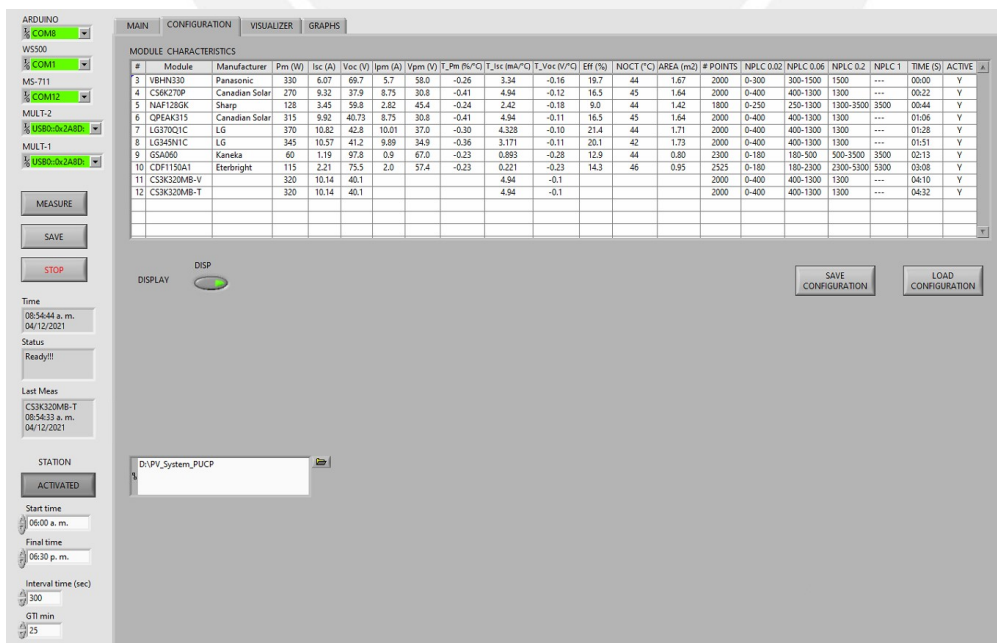


Figure 2.19: Configuration Tab screen capture.

2.4 Automated System Measurements

2.4.1 I-V Curve measurements

Figure 2.20 shows an example of the measurement of an I-V curve using the developed system. As can be seen, the I-V curve has some defects that are described below: (1) The PV module is in V_{OC} waiting for the I-V tracer circuit to connect. (2) Points captured when the voltage drops to a negative value. (3) Since the capacitor is negatively biased, a resulting current tail with a negative voltage is formed for a short time, which is the sum of I_{SC} and the capacitor current. (4) When the capacitor current and negative voltage are reduced to zero, the PV module I_{SC} current dominates while the PV module voltage is charging the capacitor. (5) The current decreases and the I-V curve is at the knee. (6) Finally, the current drops to zero and the I-V curve remains at V_{OC} , the tracer system is disconnected to continue with the discharge of the capacitor.

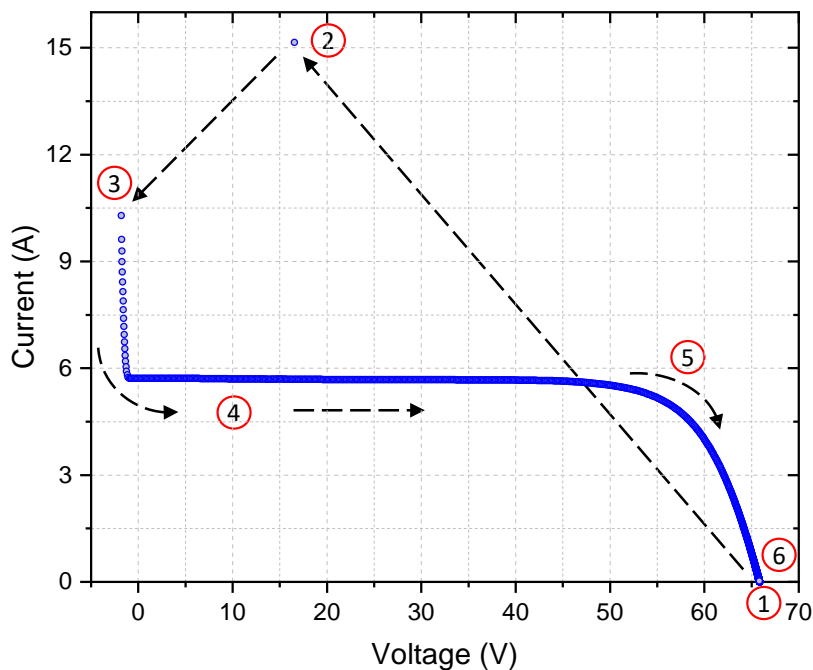
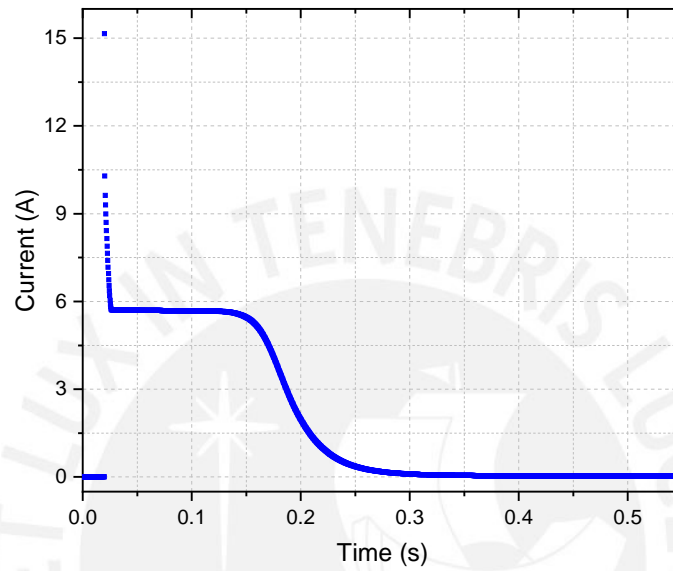
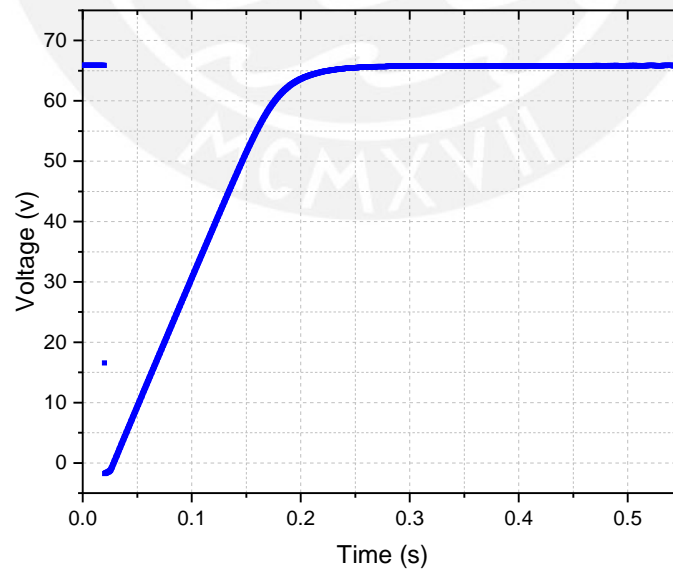


Figure 2.20: Result of the I-V curve measurement by a capacitive load.

Figure 2.21a and 2.21b show the current and voltage measurements as a function of time, respectively. As shown, the charging time is approximately 0.3 seconds. For the remaining time, the current is kept at 0, and the voltage at V_{OC} .



(a)



(b)

Figure 2.21: Measurement of (a) current and (b) voltage, as a function of time.

Figure 2.22 shows an I-V curve with partial shading. In some cases, the I-V curve does not start at I_{SC} . For the analysis of the following chapters, this kind of I-V curve is unsuitable and, thus, filtered out.

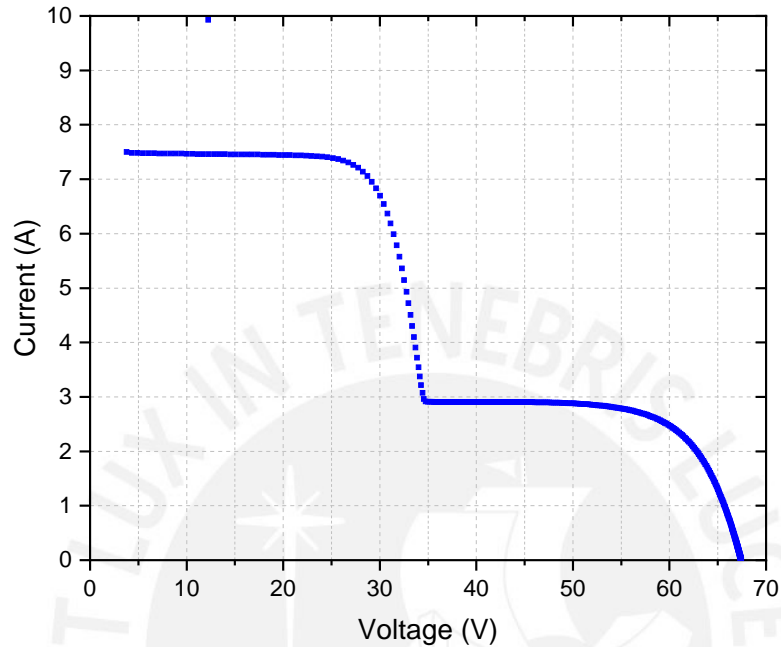


Figure 2.22: Incomplete I-V curve at the I_{SC} point and with partial shadow.

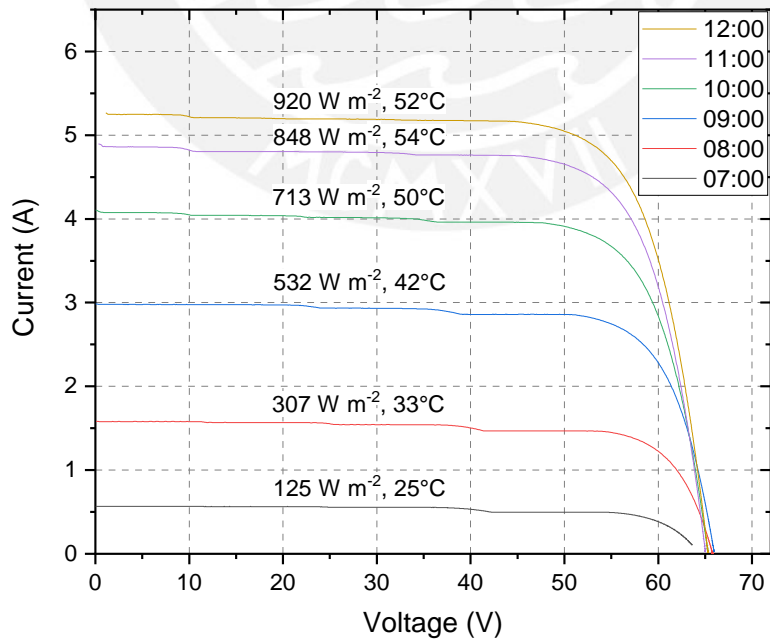


Figure 2.23: I-V curves under different levels of irradiance.

Figure 2.23 shows six I-V curves with respect to different levels of irradiance (125, 307, 532, 713, 848, 920, in $W m^{-2}$) and temperature (25, 33, 42, 50, 54, 52, in $^{\circ}C$) of a PV module.

2.4.2 Weather measurements

Figure 2.24 shows the air temperature, humidity, and irradiance measurements for an exemplary sunny summer day. The air temperature varies relatively little from $19.5^{\circ}C$ in the early morning to up to about $23.5^{\circ}C$ in the afternoon. The relative humidity is at 95 % highest at the lowest temperature and at about 76 % lowest at the highest temperature.

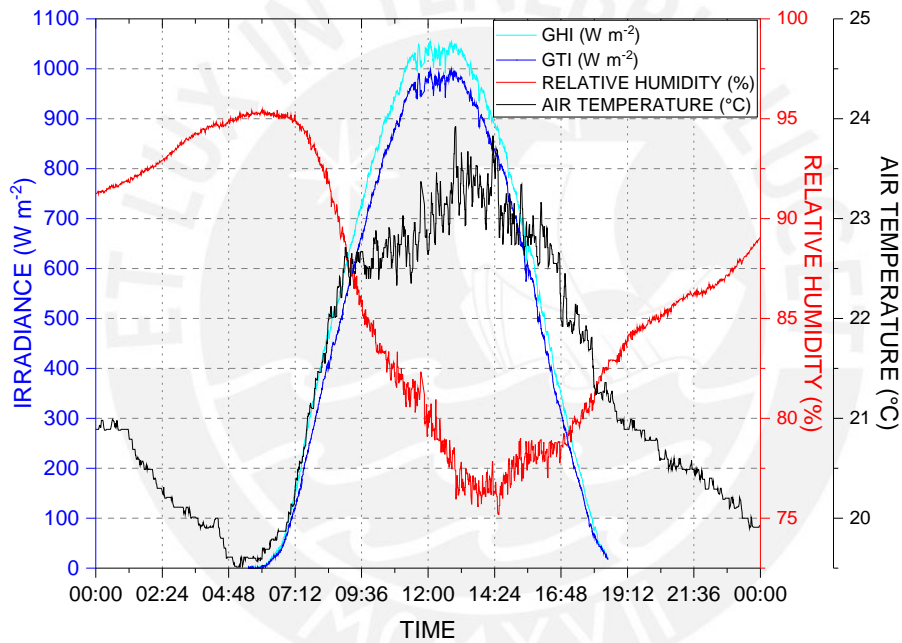


Figure 2.24: Variation of the air temperature, humidity and irradiance for a sunny summer day (13-Feb-2022).

2.4.3 Spectral measurements

Figure 2.25 shows six spectral distributions for a sunny day in Lima at different hours. Spectral irradiance distributions that were measured in a five-minute interval for irradiance levels greater than $25 W m^{-2}$ are shown in the Figure 2.26 for the sunny day.

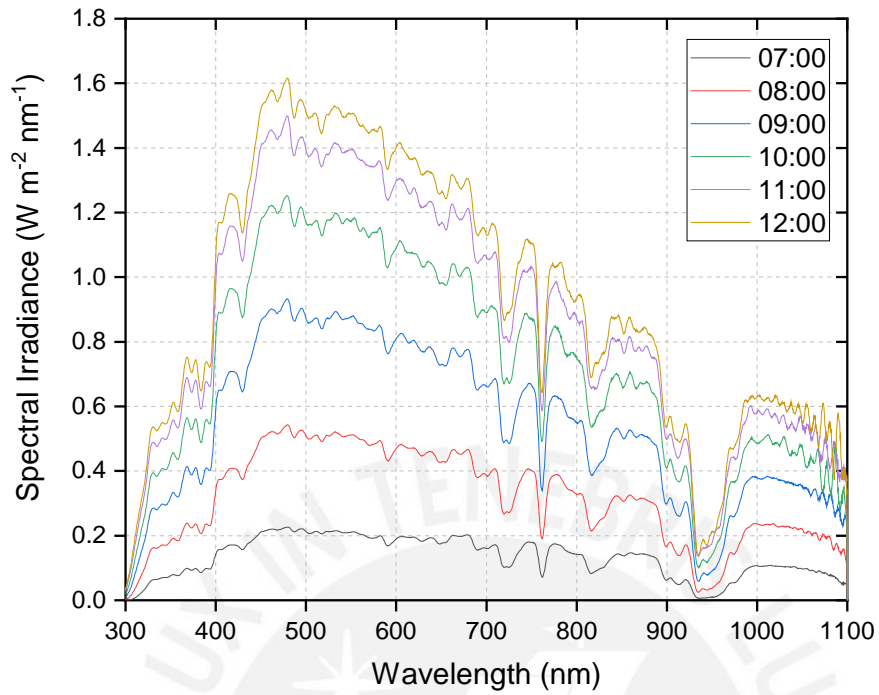


Figure 2.25: Spectral distributions by hours of a sunny day in Lima.

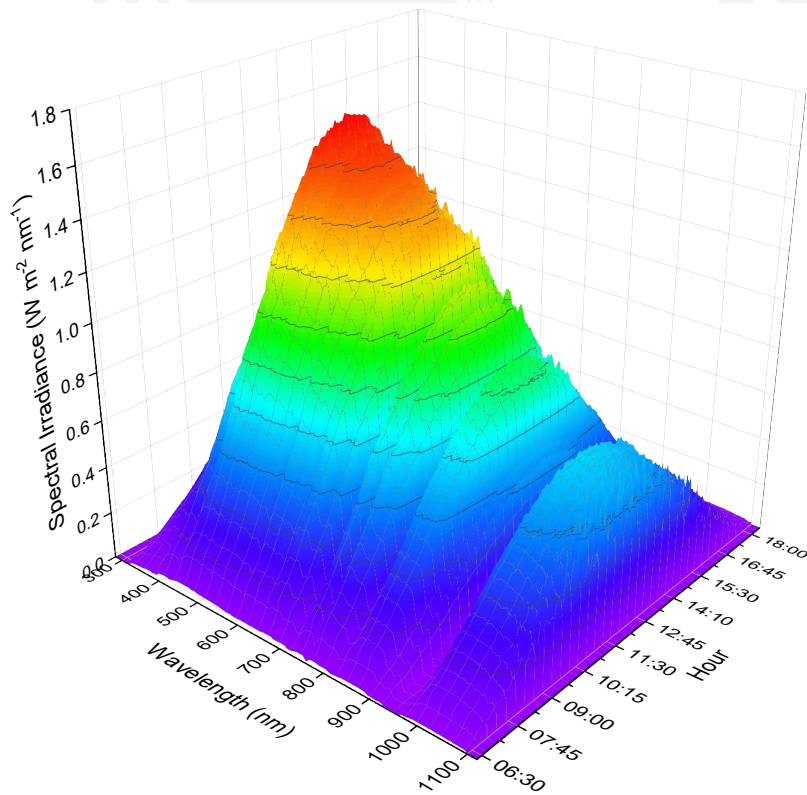
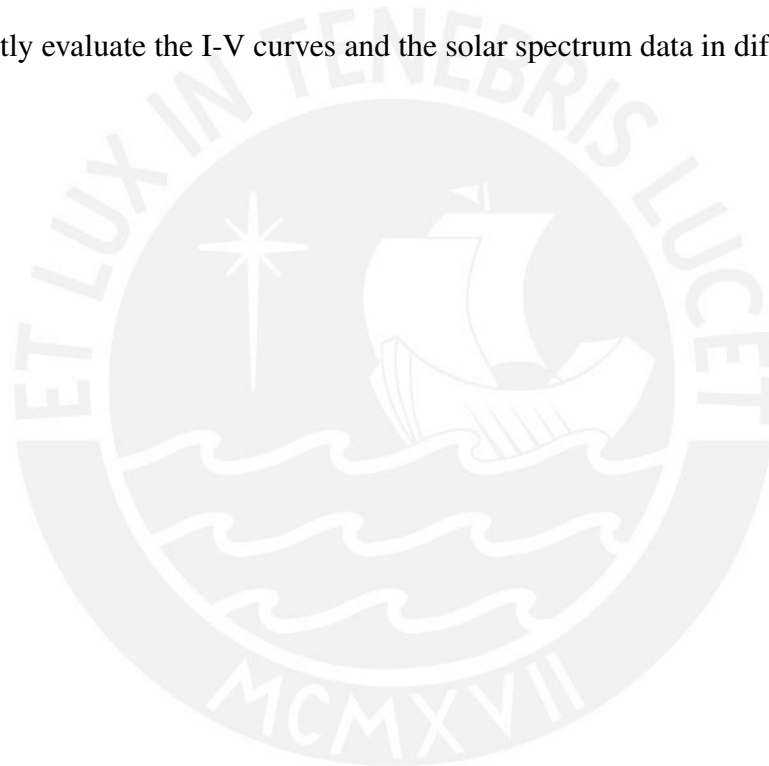


Figure 2.26: Spectral distributions for a sunny day in Lima in an interval of five minutes.

2.5 Conclusions

In this chapter, a detailed description of the measurement system was made, such as software and hardware. As shown in the measurement results, the system is capable of acquiring I-V curve data and other parameters such as the solar spectrum and environmental conditions. Therefore, the system is prepared to carry out long-term tests and is suitable for the characterization of PV modules of different technologies and electrical characteristics (P_M , I_{SC} , V_{OC}). The acquired data will be analyzed in the following chapters and filters will be shown that were designed to correctly evaluate the I-V curves and the solar spectrum data in different years.



Chapter III

Performance evaluation and characterization

3.1 Introduction

This chapter presents the performance and characterization analysis of seven different PV technologies: Heterojunction with Intrinsic Thin-Layer (HIT), Aluminum Back Surface Field (Al-BSF), Amorphous/microcrystalline silicon tandem (a-si/ μ c-Si), Interdigitated Back Contact (IBC), Passivated Emitter Rear Totally Diffused (PERT), Amorphous Silicon (a-Si), and Copper Indium Gallium Selenide (CIGS).

The estimation of the maximum power of a PV module or PV array is necessary for the evaluation of the energy performance [16]. For a correct analysis, a calibration of the maximum power is required to consider it as a reference [43]. Therefore, each PV module was previously calibrated in outdoor conditions, extrapolating the measured values to STC conditions.

To model the maximum power of Al-BSF, HIT and Tandem, during May 2019 - July 2019, two simple models were used: Osterwald and FF constant [31]. An extension of this study for a period of one year was published in [32].

To evaluate the energy conversion efficiency, the Performance Ratio was used in the seven PV technologies for two years (March 2020-February 2022). Monthly and annual time periods were taken and the effects of module temperature were considered.

3.2 Methodology

3.2.1 Experimental set-up

Table 3.1 indicates the main electrical parameters taken from the manufacturer's data sheet for each PV module. The γ , α , and β constants are the power, current, and voltage temperature coefficients, respectively.

Table 3.1: Main electrical parameters of the PV modules under study.

| PV Technology | P_M^* (W) | I_{SC}^* (A) | V_{OC}^* (V) | γ (%/°C) | α (%/°C) | β (%/°C) | η (%) |
|-------------------------|----------------|-------------------|-------------------|--------------------|--------------------|-------------------|---------------|
| HIT | 330 | 6.07 | 69.7 | -0.26 | 0.06 | -0.26 | 19.7 |
| Al-BSF | 270 | 9.32 | 37.9 | -0.41 | 0.05 | -0.32 | 16.5 |
| Tandem a-si/ μ C-Si | 128 | 3.45 | 59.8 | -0.24 | 0.07 | -0.30 | 9.0 |
| IBC | 370 | 10.82 | 42.8 | -0.30 | 0.04 | -0.24 | 21.4 |
| PERC | 345 | 10.57 | 41.2 | -0.36 | 0.03 | -0.27 | 20.1 |
| a-Si | 60 | 1.19 | 92.0 | -0.23 | 0.08 | -0.31 | 12.9 |
| CIGS | 110 | 2.07 | 77.2 | -0.23 | 0.01 | -0.31 | 14.3 |

3.2.2 Calibration

From the data collected, approximately 100 I-V curves were selected for each type of PV module, with the following criteria:

- Measured during the first days or month of outdoor exposure,
- on clear sky days at irradiances between 800-1100 W m⁻², and
- during central hours of the day.

These criteria allow conditions closer to STC and minimizing the losses associated with the angle of incidence or spectral losses [44].

P_M was extracted from each I-V curve. Equation 3.1 was applied to obtain the temperature-corrected Power ($P_{M,T \rightarrow 25}$) using the experimental values of P_M and T_m

$$P_{M,T \rightarrow 25} = \frac{P_M}{1 + \gamma (T_m - 25)} \quad (3.1)$$

Then, irradiance correction was applied with the experimental incident irradiance (G_i) to obtain, the temperature- and irradiance- corrected experimental power (P_{exp}^*)

$$P_{exp}^* = \frac{1000}{G_i} P_{M,T \rightarrow 25} \quad (3.2)$$

Finally, the experimental nominal power is obtained by averaging the corrected nominal power values, where $N = 100$.

$$P_{M,exp}^* = \frac{\sum_{i=1}^N P_{exp,i}^*}{N} \quad (3.3)$$

To obtain I_{exp}^* and V_{exp}^* corrected experimental values, the experimental values of I_{SC} and V_{OC} extracted from the I-V curves are used in the following equations:

$$I_{exp}^* = \frac{1000}{G_i} \frac{I_{SC}}{1 + \alpha (T_m - 25)} \quad (3.4)$$

$$V_{exp}^* = V_{OC} + \beta (T_m - 25) \quad (3.5)$$

Finally $I_{SC,exp}^*$ and $V_{OC,exp}^*$ are obtained by averaging 100 values of I_{exp}^* and V_{exp}^* , as in equation 3.3, respectively.

$$I_{SC,exp}^* = \frac{\sum_{i=1}^N I_{exp,i}^*}{N} \quad (3.6)$$

$$V_{OC,exp}^* = \frac{\sum_{i=1}^N V_{exp,i}^*}{N} \quad (3.7)$$

To compare the modeled with the experimental results and for information about the data scattering, statistical indices were used. The standard deviation (equation 3.8) and the coefficient of variation (equation 3.9) were calculated:

$$\sigma_I = \sqrt{\frac{\sum_i^N (X(i) - \bar{X})^2}{N}} \quad (3.8)$$

$$CV = \frac{\sigma_I}{\bar{X}} \times 100\% \quad (3.9)$$

3.2.3 Modeling the maximum Power

To verify with what fidelity simple analytical methods can provide an estimate of the outdoor performance of different PV technologies. Two known methods to translate the maximum power under outdoor conditions to STC were used:

- **Osterwald's method.** This is one of the known and straightforward methods, as demonstrated in [45]. The maximum power modeled is equal to

$$P_{M,Ost} = P_M^* \frac{G_i}{G_i^*} [1 - \gamma (T_m - 25)] \quad (3.10)$$

where P_M^* can be the nominal value at STC or the calibrated experimental value.

- **Constant Fill Factor (FF_k) method.** This method assumes that the FF remains constant in all operating conditions, and that the values of the I_{SC} and the V_{OC} vary linearly with the incident irradiance and the operating temperature, respectively. As was demonstrated in [46], the maximum power modeled is equal to,

$$P_{M,FFk} = FF^* I_{SC} V_{OC} \quad (3.11)$$

where I_{SC} and V_{OC} are calculated with equations 2.3 and 2.2, respectively. In addition, FF^* is calculated from the nominal values at STC or calibrated experimental values.

$$FF^* = \frac{P_M^*}{I_{SC}^* V_{OC}^*} \quad (3.12)$$

When comparing the values of $P_{M,Ost}$ and $P_{M,FFk}$ modeled with respect to the P_M experimental values, a correction factor κ was introduced. This factor compensates the experimental values of P_M when it is underestimated or overestimated by the method used. A corrected nominal power is obtained by applying the correction constant to the value of $P_{M,exp}^*$ and FF_{exp}^* :

$$P_{M,exp}^{*,corr} = \kappa \times P_{M,exp}^* \quad (3.13)$$

$$FF_{exp}^{*,corr} = \kappa \times FF_{exp}^* \quad (3.14)$$

where:

$$\kappa = \begin{cases} > 1, \text{ under-estimation} \\ = 1, \text{ correct prediction} \\ < 1, \text{ over-estimation} \end{cases} \quad (3.15)$$

The statistical parameters Normalized Root Means Square Error (*NRMSE*) and Normalized Mean Bias Error (*NMBE*) were calculated to evaluate each method's goodness after applying the correction factor. The *NRMSE* equation 3.16 provides information on the scattering of the modeled power values vs. the measured ones. In contrast, the *NMBE* equation 3.17 provides the average deviation of the modeled power values from the measured.

$$NRMSE = 100 \% \times \frac{\sqrt{\frac{\sum_{i=1}^N (P_{Ti} - P_{Oi})^2}{N}}}{\frac{1}{N} \sum_{i=1}^N P_{Oi}} \quad (3.16)$$

$$NMBE = 100 \% \times \frac{\frac{\sum_{i=1}^N (P_{Ti} - P_{Oi})}{N}}{\frac{1}{N} \sum_{i=1}^N P_{Oi}} \quad (3.17)$$

Where P_{Ti} is the i -th modeled power after applying the correction factor, P_{Oi} is the i -th measured power, and N is the number of modeled or measured values.

3.2.4 Module Performance Ratio

To evaluate the energy conversion efficiency, the Module Performance Ratio (PR_{mod}) was defined as the sum of the $P_M(i)$ divided by the sum of $G_i(i)$ simultaneously measured in a time interval [47]

$$PR_{mod} = \frac{G^* \sum P_M(i)}{P_M^* \sum G_i(i)} \quad (3.18)$$

The PR_{mod} corrected by temperature is also considered,

$$PR_{mod,T \rightarrow 25} = \frac{G^* \sum P_{M,T \rightarrow 25}(i)}{P_M^* \sum G_i(i)} \quad (3.19)$$

Here, $G^* = 1000 \text{ W m}^{-2}$, and as power reference, P_M^* in STC and $P_{M,exp}^*$ calibrated were evaluated. Also, the PR_{mod} was estimated in periods of months, PR_{mod}^m , and years, PR_{mod}^a .

3.3 Predicted vs. Modeled Power

3.3.1 Calibration results

Tables 3.2, 3.3, and 3.4 show the comparison of the calibration results of P_M^* , I_{SC}^* , V_{OC}^* , and FF^* with respect to the manufacturer's values of three PV modules: Al-BSF, HIT and Tandem a-si/ μC -Si. The calibration was carried out during the first weeks of May 2019, where the measurement system was fully operational. As shown in the tables, the low values of the standard deviation in the P_M^* , I_{SC}^* , V_{OC}^* , and FF^* , with respect to the manufacturer, indicated that most of the measurements were very close to the experimental calibration values. While the low values of the coefficient of variation indicated that there is a low dispersion and variability in the experimental measurements.

Table 3.2: Al-BSF calibrated electrical parameters.

| | Manufacturer | Experimental | Standard deviation | Coefficient of variation | Relative difference |
|----------------|--------------|--------------|--------------------|--------------------------|---------------------|
| P_M^* (W) | 270 | 269.2 | 1.87 | 0.7 % | 0.3 % |
| I_{SC}^* (A) | 9.32 | 9.45 | 0.13 | 1.4 % | -1.4 % |
| V_{OC}^* (V) | 37.9 | 37.2 | 0.15 | 0.4 % | 1.8 % |
| FF^* | 0.76 | 0.77 | 0.01 | 1.0 % | -0.1 % |

Table 3.3: HIT calibrated electrical parameters.

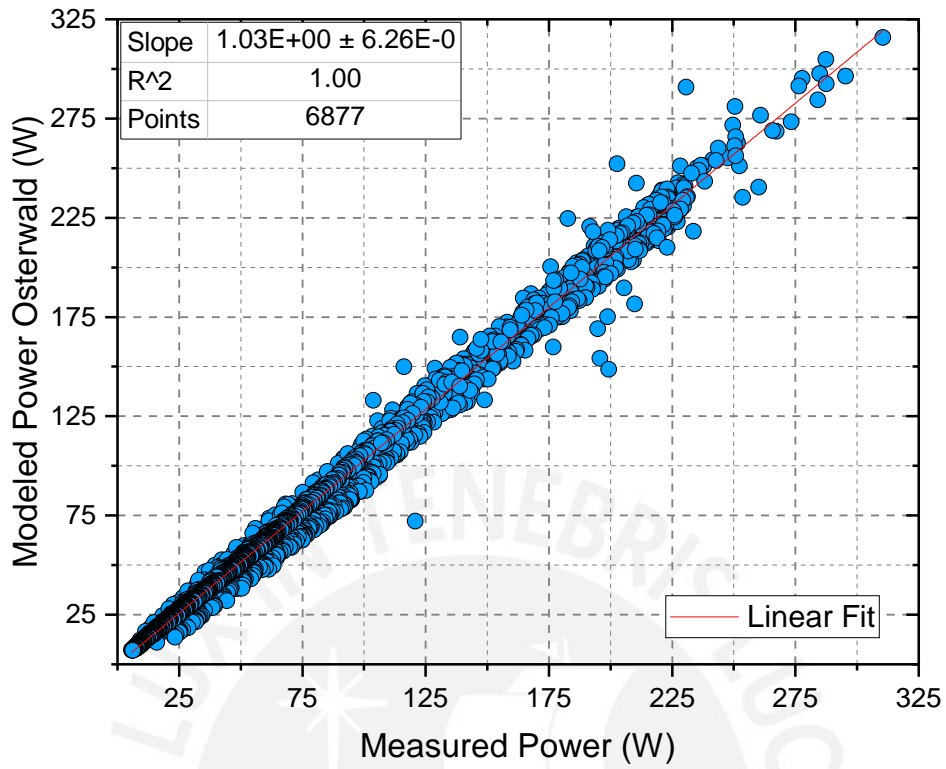
| | Manufacturer | Experimental | Standard deviation | Coefficient of variation | Relative difference |
|----------------|--------------|--------------|--------------------|--------------------------|---------------------|
| P_M^* (W) | 330 | 324.6 | 5.90 | 1.8 % | 1.6 % |
| I_{SC}^* (A) | 6.07 | 6.05 | 0.13 | 2.1 % | 0.3 % |
| V_{OC}^* (V) | 69.7 | 70.4 | 0.49 | 0.7 % | -0.9 % |
| FF^* | 0.78 | 0.76 | 0.01 | 1.3 % | 2.2 % |

Table 3.4: Tandem a-si/ μ c-Si calibrated electrical parameters.

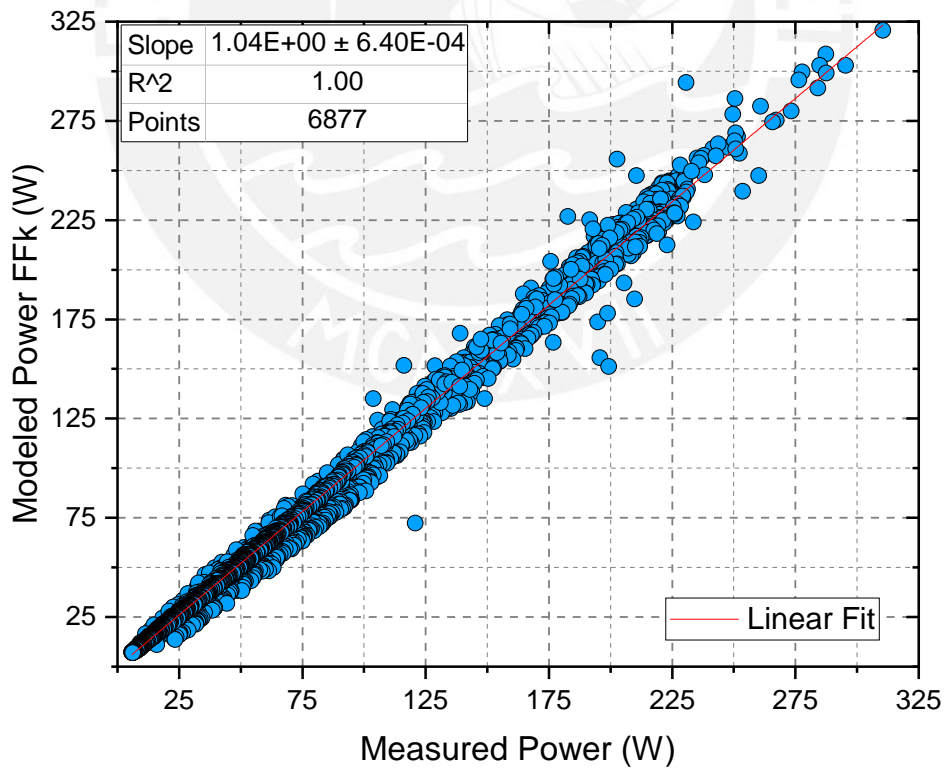
| | Manufacturer | Experimental | Standard deviation | Coefficient of variation | Relative difference |
|----------------|--------------|--------------|--------------------|--------------------------|---------------------|
| P_M^* | 128 | 127.9 | 2.08 | 1.6 % | 0.1 % |
| I_{SC}^* (A) | 3.45 | 3.32 | 0.07 | 2.0 % | 3.8 % |
| V_{OC}^* (V) | 59.8 | 59.1 | 0.17 | 0.3 % | 1.1 % |
| FF^* | 0.62 | 0.65 | 0.004 | 0.6 % | -5.1 % |

3.3.2 Modeling results compared with experimental results

Figures 3.1, 3.2, and 3.3 show the linear fit of $P_{M,Ost}$ and $P_{M,FFk}$ vs. the power measured for Al-BSF, HIT, and Tandem, respectively, between May 2019 to July 2019. For this evaluation, the experimental $P_{M,exp}^*$ and FF_{exp}^* values were used in equations 3.10 and 3.11, respectively. The slope value of the linear correlation and the determination coefficient (R^2) are close to or equal to 1. So the Osterwald and FFk methods can reasonably estimate the power. However, the value of the slope is slightly greater or less than 1, which indicates that the Osterwald or FFk method overestimates or underestimates the value of the modeled power.

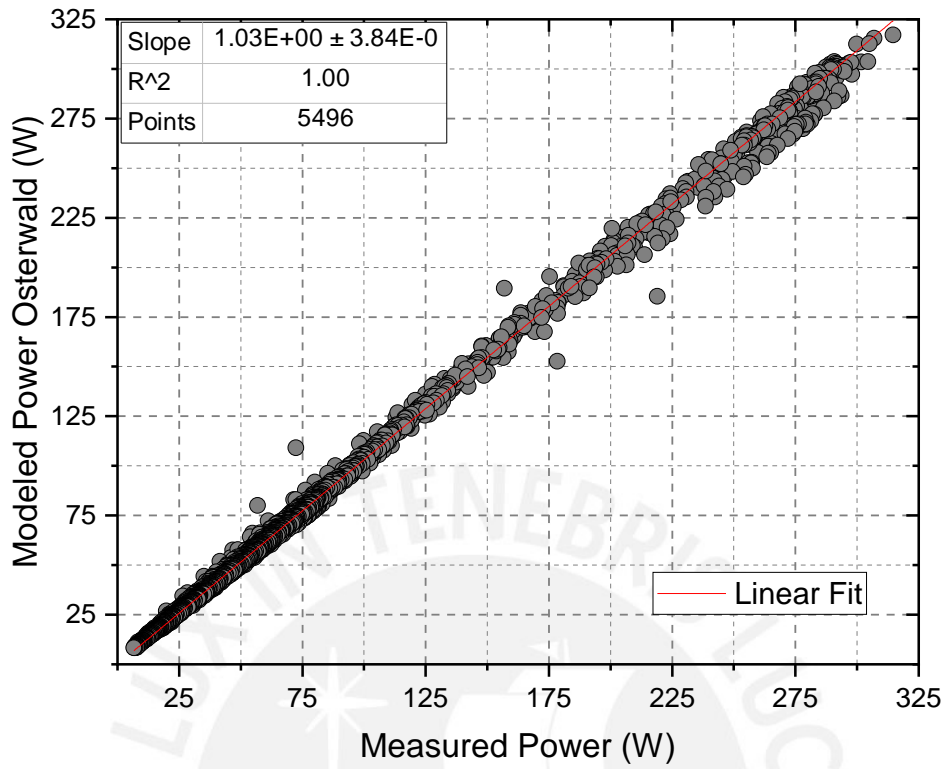


(a)

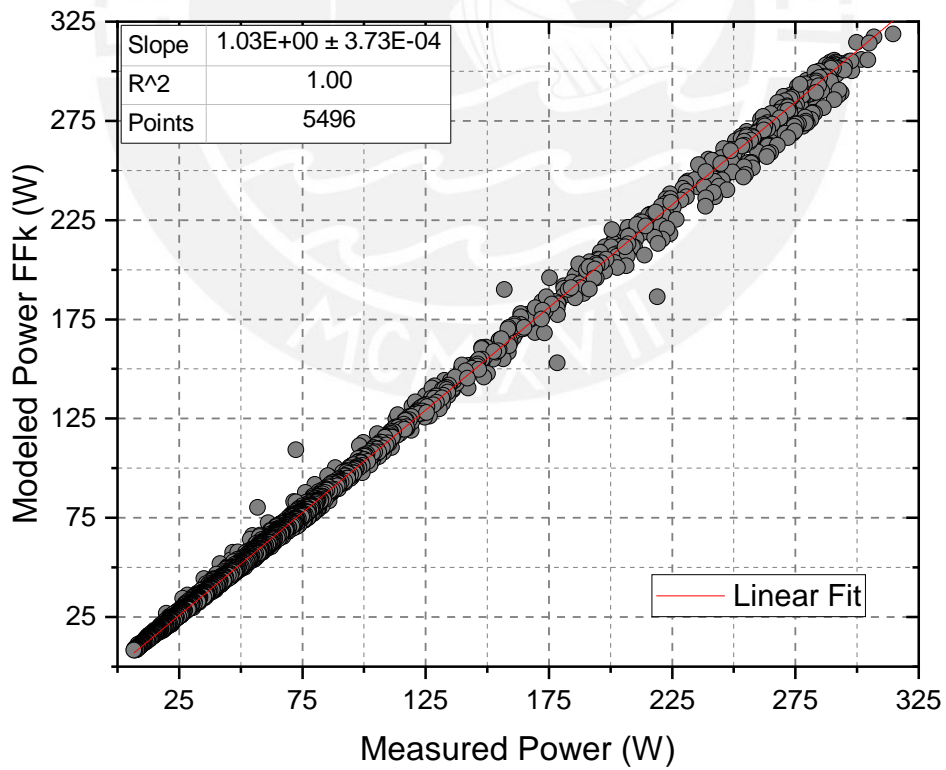


(b)

Figure 3.1: AI-BSF Modeled Power by the method (a) Osterwald and (b) FFk.

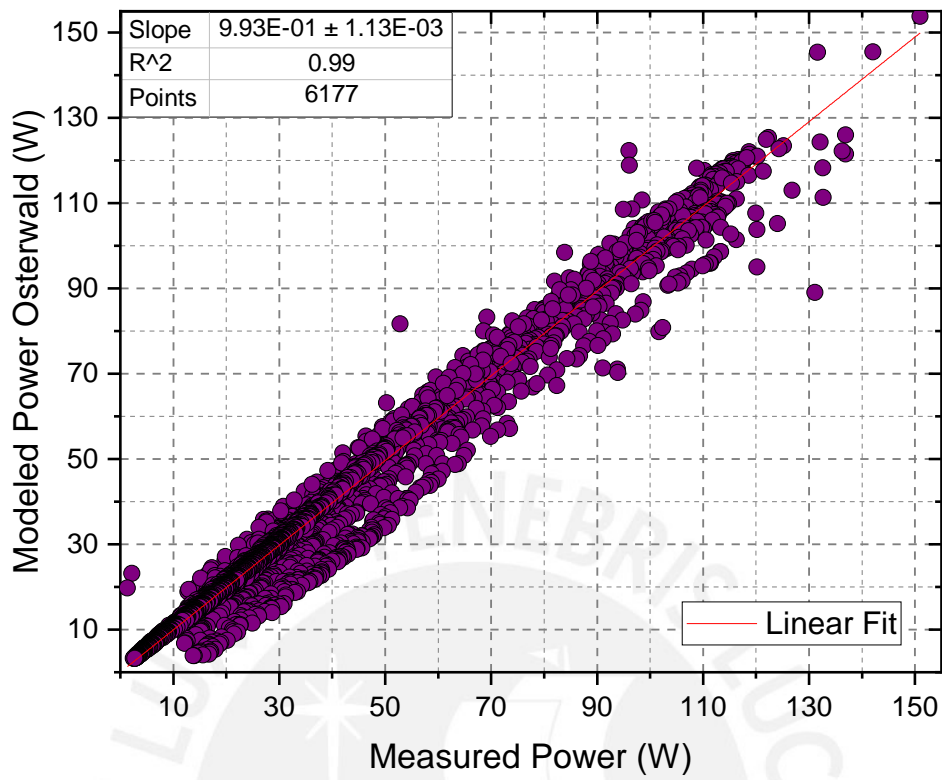


(a)

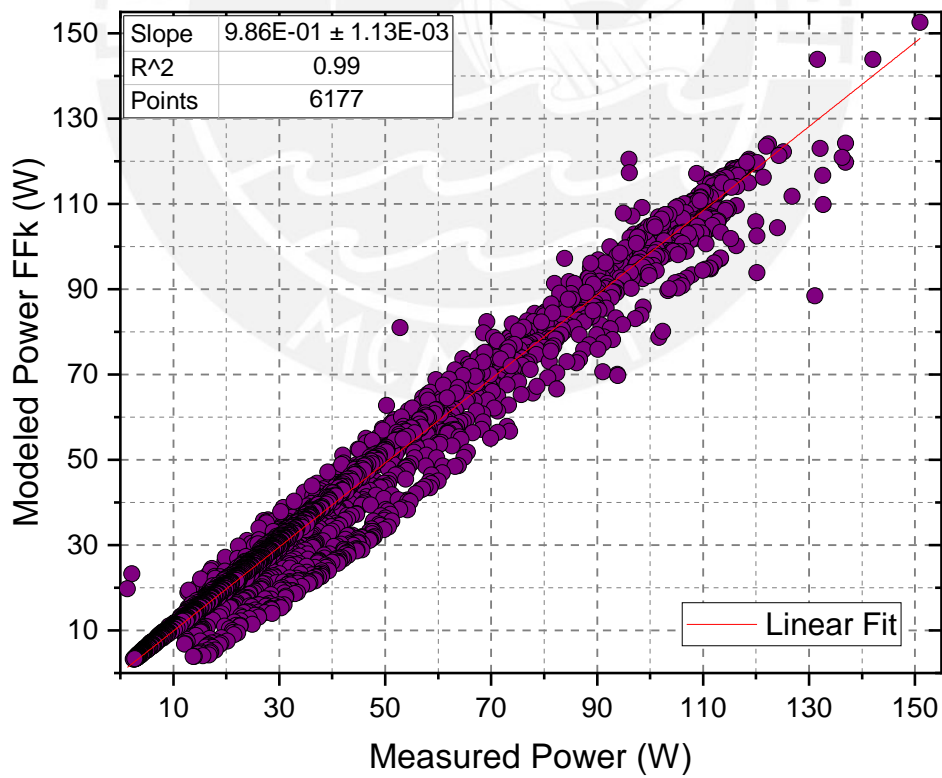


(b)

Figure 3.2: HIT Modeled Power by the method (a) Osterwald and (b) FFk.



(a)



(b)

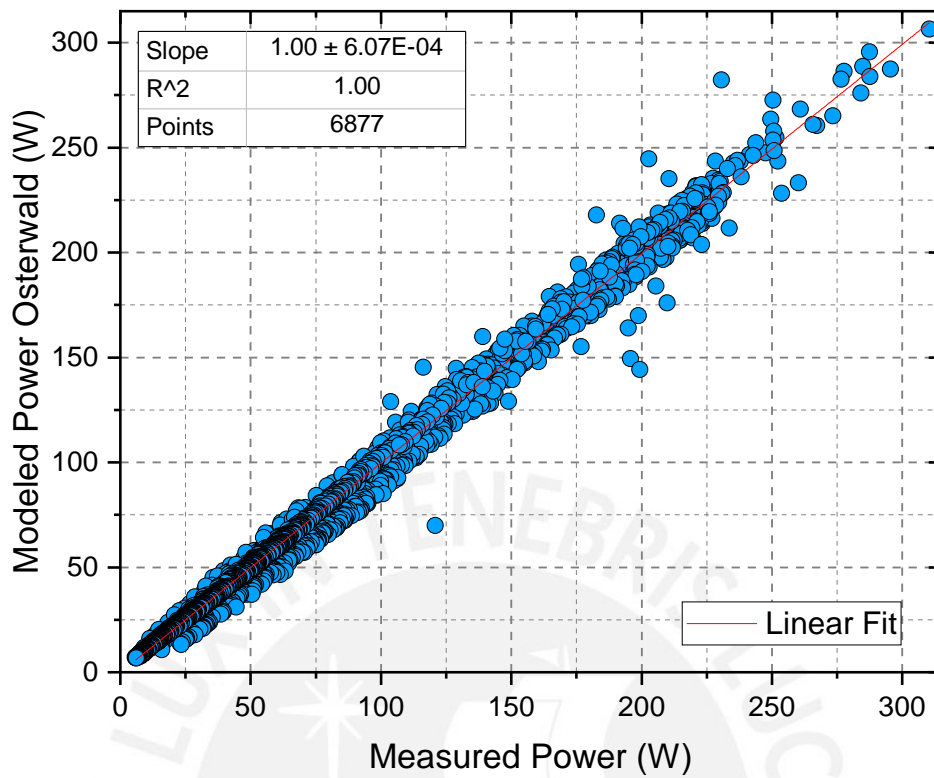
Figure 3.3: Tandem Modeled Power by the method (a) Osterwald and (b) FFk.

Table 3.5 shows the κ correction factors, in three months, for the P_M and FF applying the Osterwald and the FFk methods, respectively. Also, shows the corrected experimental nominal values $P_{M,exp}^{*,corr}$ and $FF_{exp}^{*,corr}$ when applying the correction factor to the experimental nominal values. For Al-BSF, the correction factor less than 1 implies that the Osterwald and FFk methods are overestimated the power, and, for its value, Osterwald method is better than the FFk method. Whereas for HIT, there is no difference in using either of the two methods. For tandem, the methods are underestimated the power, and Osterwald method is better than the FFk method.

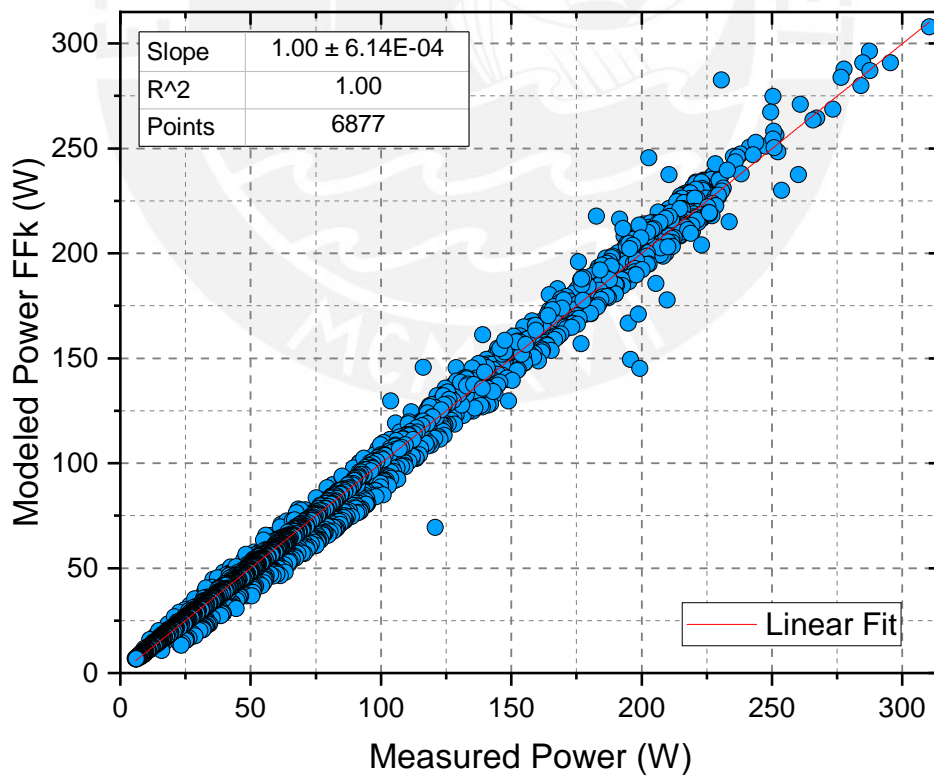
Table 3.5: Experimental Power and FF corrected by the Osterwald and FFk method

| PV technology | Method | Experimental value | Correction factor κ | Corrected value |
|----------------------------|----------------------------|--------------------|----------------------------|-----------------|
| Al-BSF | P_M^* (W) (Osterwald) | 269.24 | 0.97 | 261.17 |
| | FF^* (FFk) | 0.77 | 0.96 | 0.73 |
| HIT | P_M^* (W) (Osterwald) | 324.60 | 0.97 | 314.86 |
| | FF^* (FFk) | 0.76 | 0.97 | 0.74 |
| Tandem a-si/ μ c-Si | P_M^* (W) (Osterwald) | 127.93 | 1.01 | 129.21 |
| | FF^* (FFk) | 0.65 | 1.02 | 0.66 |

Figures 3.4, 3.5, and 3.6 show the linear fit of the power modeled by the Osterwald and FFk methods using the corrected experimental values $P_{M,exp}^{*,corr}$ and $FF_{exp}^{*,corr}$ vs. the experimental power values for each PV technology.

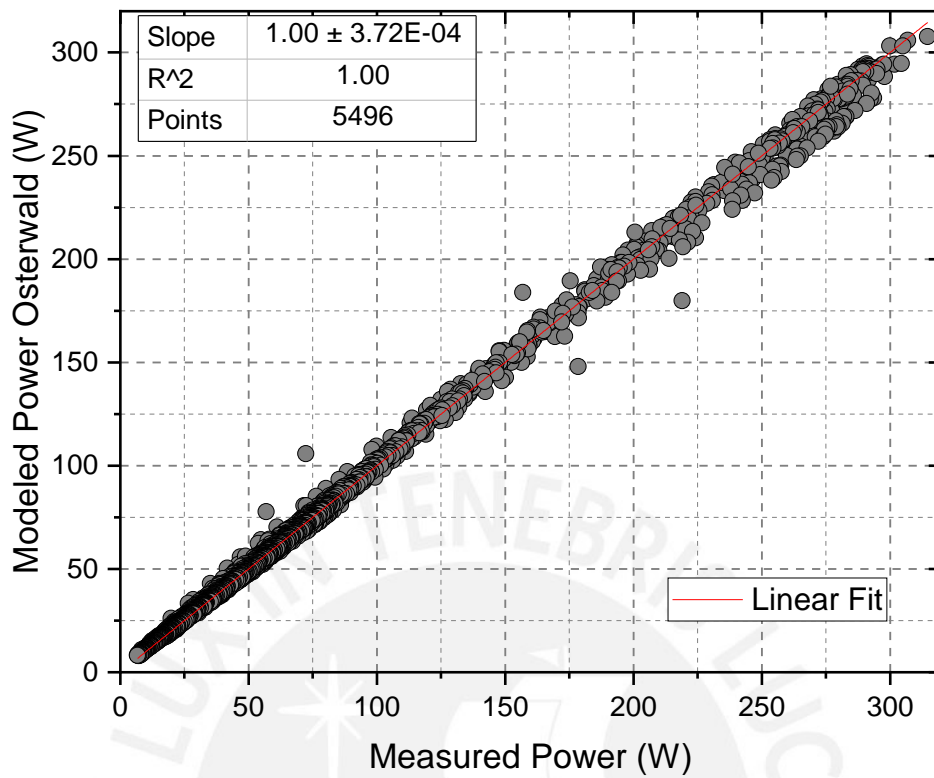


(a)

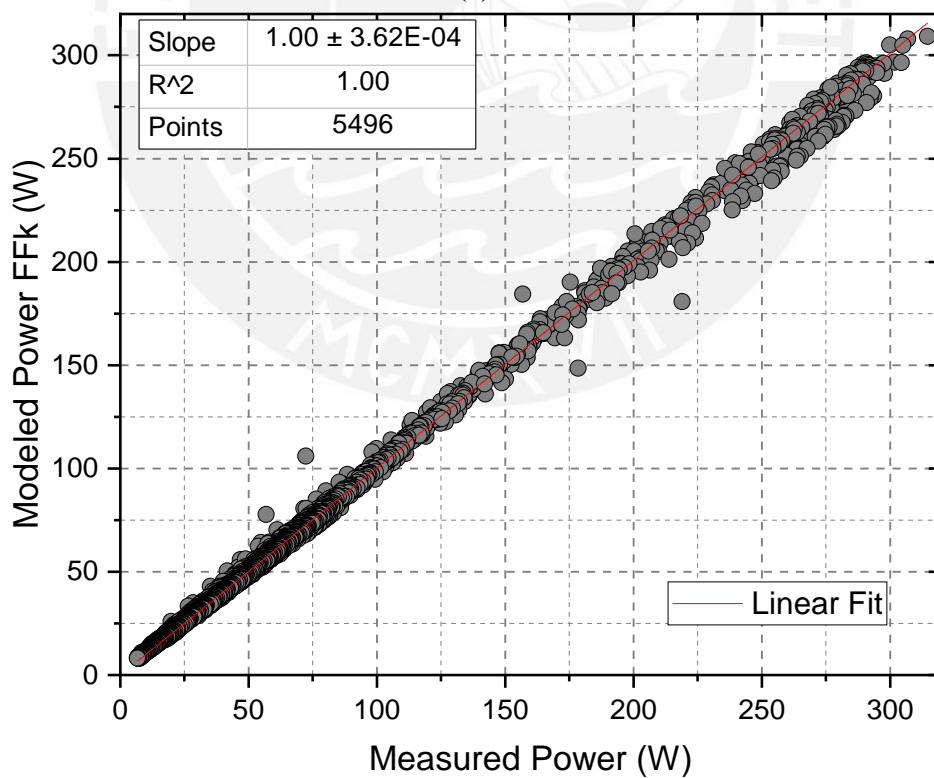


(b)

Figure 3.4: AI-BSF Modeled Power corrected by the method (a) Osterwald and (b) FFk.

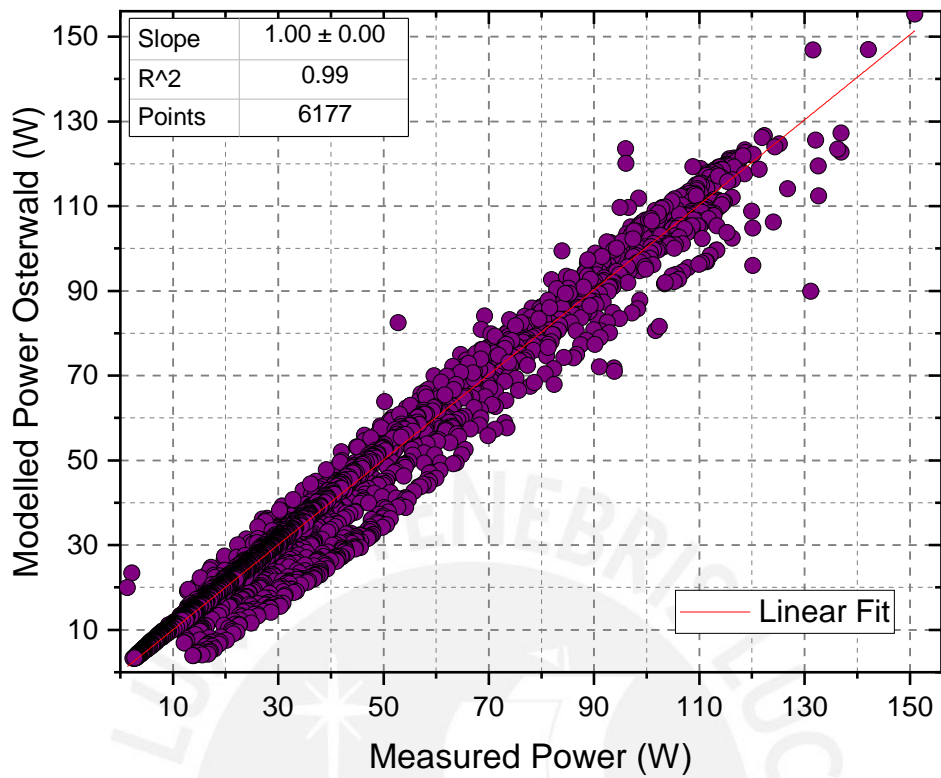


(a)

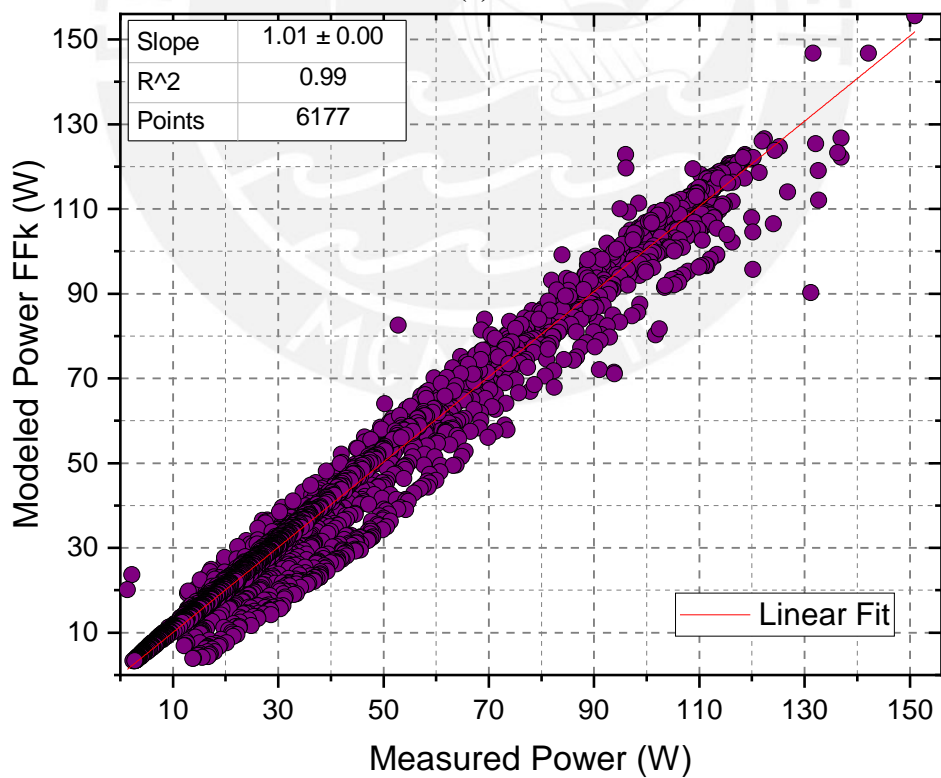


(b)

Figure 3.5: HIT Modeled Power corrected by the method (a) Osterwald and (b) FFk.



(a)



(b)

Figure 3.6: Tandem Modeled Power corrected by the method (a) Osterwald and (b) FFk.

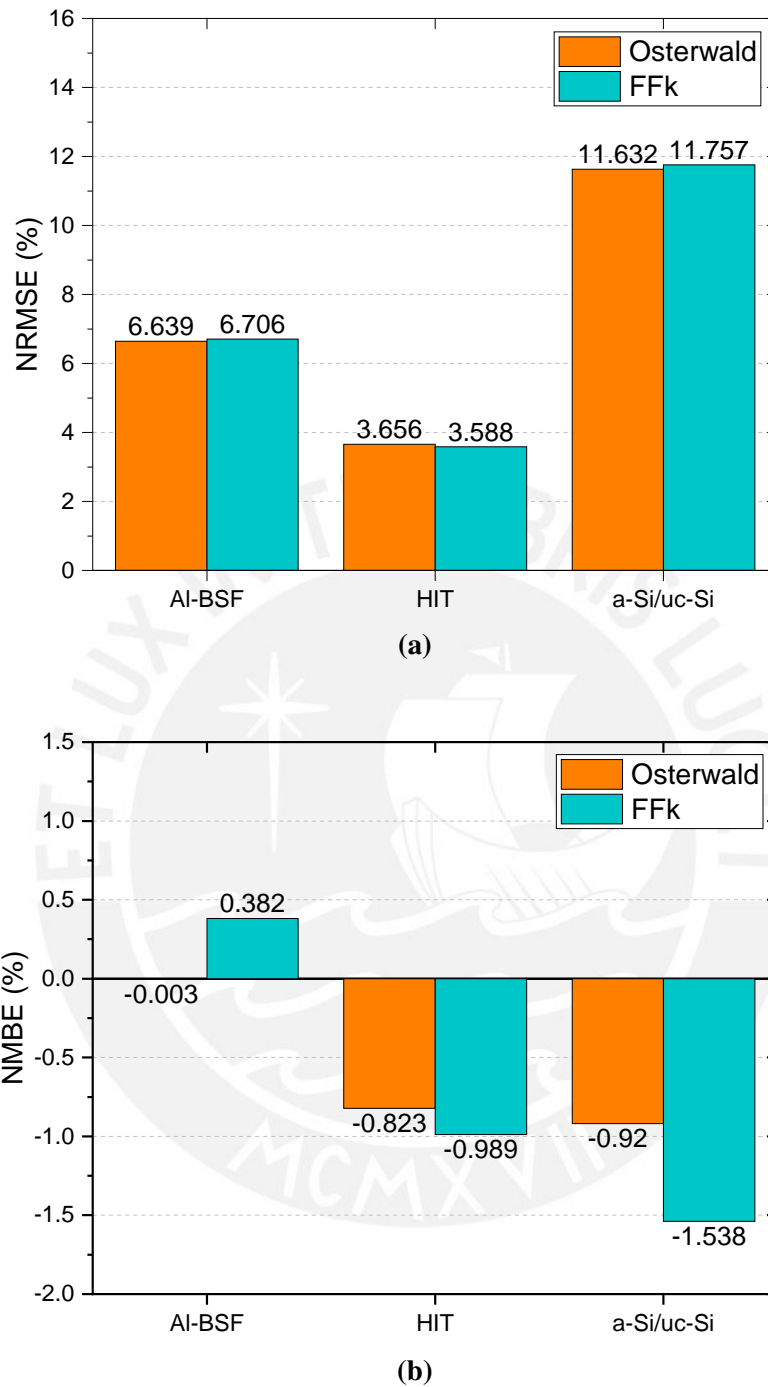


Figure 3.7: (a) NRMSE and (b) NMBE, comparing the methods of Osterwald and FFk.

Figure 3.7a shows the *NRMSE* values for the different PV technologies after applying the Osterwald and the *FFk* model. HIT module is the PV technology with a lowest *NRMSE* and, thus, dispersion. This may indicate that this PV technology is less susceptible to environmental conditions not considered by the models and that may be dominant in Lima between the autumn

and winter months. On the other hand, the a-si/ μ c-Si module is the technology with the highest *NRMSE* and, thus, highest dispersion. This is in accordance with results presented in [48], probably these technologies based on thin-films and tandems are more dependent on external effects that are not considered in these models such as the spectral effect [49].

Figure 3.7b shows the *NMBE* values for the different applied PV technologies and models. The values less than 1% mostly for the Osterwald model and the *FFk* in the different PV technologies indicate that the two models interpret the measurement system very well, with a lower error for Al-BSF and a higher error for a-si/ μ c-Si.

3.4 Module Performance Ratio results

3.4.1 Calibration results of nominal power

Table 3.6 shows the P_M^* in STC, $P_{M,exp}^*$, and calibration results, of seven different PV modules following the procedure in section 3.2.2. This process was carried out in March 2020 and again in February 2021 to verify the stability of each PV module. The HIT, Al-BSF, and Tandem a-Si/ μ c-Si modules have been exposed to the weather since 2019. While the IBC, PERT, a-Si, and CIGS modules were installed in 2020 when the first calibration was done.

The IBC module showed the greatest difference in $P_{M,exp}^*$ (-6.9%) with respect to its P_M^* values in STC, while in the second calibration, the difference increased slightly (-7.2%). The PERT module showed stable $P_{M,exp}^*$ values between the first and second calibration, with a deviation of -2% and -1.9% , respectively, with respect to P_M^* . The a-Si module showed a high $P_{M,exp}^*$ ($+13.2\%$) with respect to its P_M^* values in STC for the first calibration. For the second calibration, it decreased to $+7.2\%$. This stabilization behavior of a-Si is known as the Staebler-Wronski effect [50]. The CIGS module showed a difference in $P_{M,exp}^*$ of -6% with respect to P_M^* values in STC for the first calibration. While in the second calibration, the deviation decreased to -1.3% , possibly due to metastability [51].

Table 3.6: Calibration of power in seven PV technologies in March 2020 and February 2021.

| PV Technology | P_M^* (W) | $P_{M,exp}^*$ (W) (Mar 2020) | Deviation (%) | $P_{M,exp}^*$ (W) (Feb 2021) | Deviation (%) | Δ (%) |
|-------------------------|----------------|---------------------------------|------------------|---------------------------------|------------------|--------------|
| HIT | 330 | 310.37 | -5.95 | 314.99 | -4.55 | +1.40 |
| Al-BSF | 270 | 253.80 | -6.0 | 254.40 | -5.78 | +0.22 |
| Tandem a-si/ μ c-Si | 128 | 126.43 | -1.23 | 126.60 | -1.09 | +0.14 |
| IBC | 370 | 344.66 | -6.85 | 343.36 | -7.2 | -0.35 |
| PERC | 345 | 338.09 | -2.0 | 338.43 | -1.91 | +0.09 |
| a-Si | 60 | 67.92 | +13.2 | 64.32 | +7.2 | -6.0 |
| CIGS | 110 | 103.45 | -5.96 | 108.55 | -1.32 | +4.64 |

3.4.2 Monthly and Annual Module Performance Ratio results

The PR_{mod}^m analysis was performed from March 2020 to February 2022. By taking the $P_{M,exp}^*$ from the first week of March 2020 as reference for calculating PR_{mod}^m , we can observe how deviations from the operating conditions during the calibrations impact the PR_{mod}^m in the subsequent months. Figure 3.8 and Figure 3.9, separated into crystalline silicon (c-Si) and thin-film (TF) PV technologies, respectively, show: monthly PR (PR_{mod}^m), monthly PR corrected for temperature ($PR_{mod,T \rightarrow 25}^m$), the monthly average of the PV module temperature (\overline{T}_m) and the air temperature (\overline{T}_a), and the monthly average of daily irradiation (\overline{H}_m). Due to a malfunction of the measurement system, there are two spacing's in March and August 2022.

Figure 3.8, PR_{mod}^m is higher in the colder winter months (July-September) except in 2020, when there was no regular cleaning campaign due to the quarantine period. On the other hand, in the hot summer months (December-February), the PR_{mod}^m has lower values.

The HIT almost always shows a higher PR_{mod}^m value than other technologies, except in November 2020. This high performance is probably due to its low-temperature coefficient. Furthermore, it can be seen that the PR_{mod}^m of Al-BSF has a lower value compared to the other technologies. Perhaps because it has a high-power temperature coefficient and is more affected by low irradiance in the winter months. The IBC initially appears to have a high PR_{mod}^m with respect to the other technologies, almost equal to the HIT. But in the following months a decline is seen until it is almost equal to Al-BSF and PERT, probably due to a stabilization process. The

PERT module has an intermediate behaviour between HIT and Al-BSF in the first year. Still, in the second year, its PR_{mod}^m is more similar to Al-BSF.

For $PR_{mod,T \rightarrow 25}^m$ in the first months of 2020, similar values are seen for all technologies since in this month the calibration was done and where the IBC and PERT modules came into operation. In the following months of 2020 there was no similar trend among all technologies. Probably because the measurement system was left without proper maintenance and cleaning in the quarantine months, in addition to possible losses due to low irradiance in the winter months. Then in 2021, a similar trend of $PR_{mod,T \rightarrow 25}^m$ is seen in all technologies. Also, it can be seen that $PR_{mod,T \rightarrow 25}^m$ values greater than 1 were obtained for April 2021, which could be due to better conditions in this month, like spectral gain, than in March 2020 where the calibration was made.

Figure 3.9, the PR_{mod}^m in all TF technologies have similar behaviors and oscillatory variations in the months of 2020 and 2021. TF PV modules typically have a low-temperature coefficient and are spectrally sensitive [52].

Tandem a-si/ μ c-Si shows a stable oscillatory behavior between 0.90 to 0.92 in the first year and 0.90 to 0.96 in the second year since this module was in operation a year ago. The a-Si module shows a decay of the PR_{mod}^m from the first five months of operation until July 2020, when it begins to stabilize and have an oscillatory behaviour. This is because a high initial value (March 2020) for the calibrated $P_{M,exp}^*$ of a-Si was taken as a reference. In the second year, the a-Si shows a more significant decline. The CIGS module shows a slight increase in PR_{mod}^m in the first three months of operation, then presents an oscillatory behaviour. The CIGS performs better than the other TF modules, with values close to 1. This could be because a low $P_{M,exp}^*$ value was considered as a reference or due to more favourable conditions than the calibration month.

No significant increases are shown for the $PR_{mod,T \rightarrow 25}^m$ since the TF technologies are not significantly affected by temperature. The CIGS shows values greater than 1 that could be due to better-operating conditions concerning the calibration month or due to spectral gains.

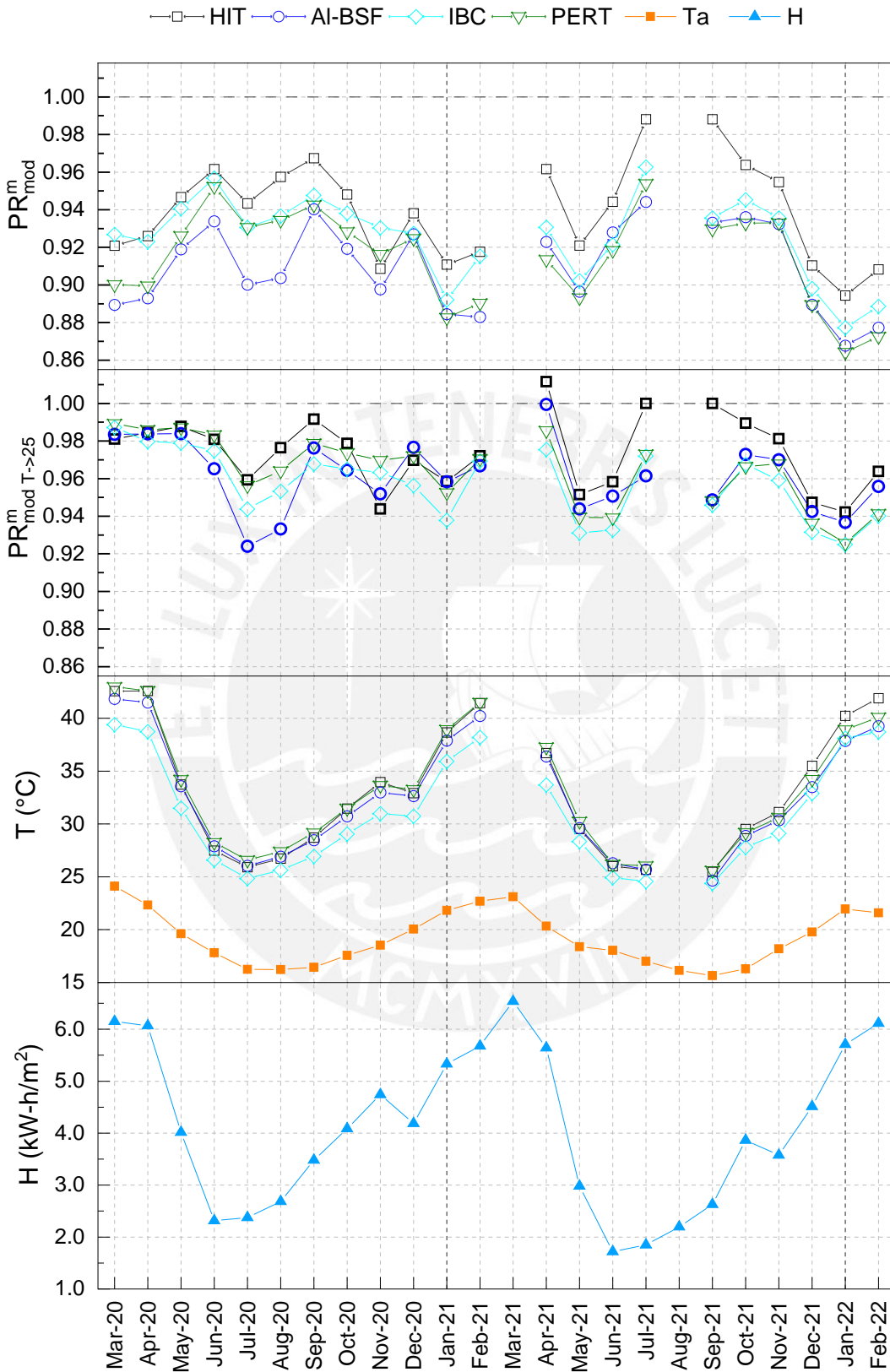


Figure 3.8: PV technologies based in c-Si: (a) PR (b) PR corrected by temperature (c) Monthly average of the module temperature and air temperature (d) Monthly average of daily irradiation.

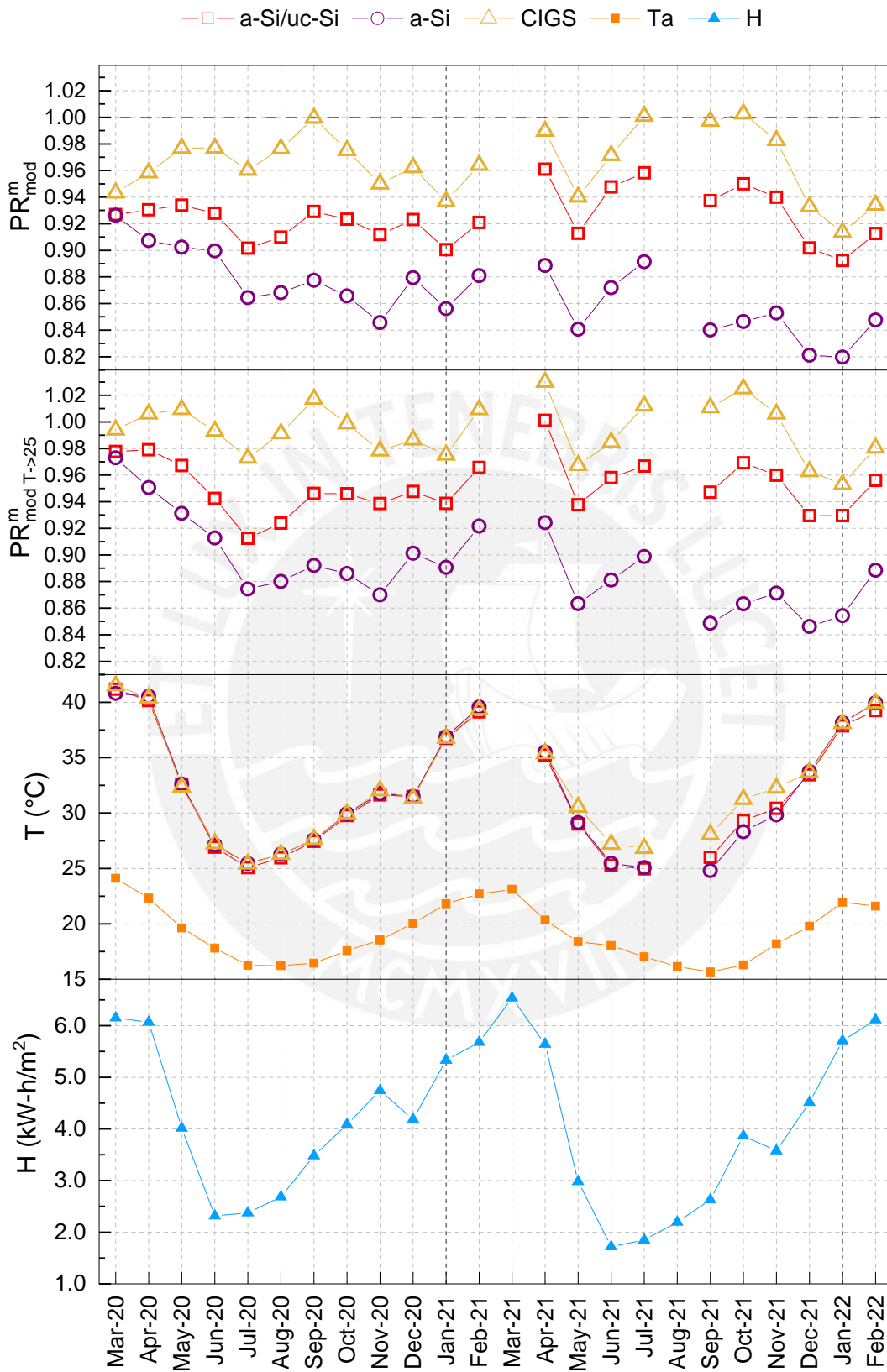


Figure 3.9: PV technologies based in TF: (a) PR (b) PR corrected by temperature (c) Monthly average of the module temperature and air temperature (d) Monthly average of daily irradiation.

For the annual PR_{mod}^a the $P_{M,exp}^*$ calibrated in March 2020 and the P_M^* in STC served as reference. For the average in 2021, the months of March and August were not considered. Figure 3.10 and Figure 3.11 show the PR_{mod}^a and $PR_{mod,T \rightarrow 25}^a$ for crystalline silicon and thin-film PV technologies, respectively, with respect to the $P_{M,exp}^*$.

The HIT does not show a considerable change in the PR_{mod}^a and $PR_{mod,T \rightarrow 25}^a$ from the first to the second year. Al-BSF has the lowest PR_{mod}^a performance among the c-Si technologies in the first year. However, when corrected for temperature, Al-BSF ranks equal to the other c-Si technologies. For the second year, there is no variation in PR_{mod}^a and a slight decrease in $PR_{mod,T \rightarrow 25}^a$. IBC and PERT show an intermediate performance between HIT and Al-BSF in PR_{mod}^a for the first year. On the other hand, $PR_{mod,T \rightarrow 25}^a$, IBC and PERT equal Al-BSF and HIT, respectively. In the second year, there was a similarly scaled decrease, about 1% in PR_{mod}^a , and 2% in $PR_{mod,T \rightarrow 25}^a$, for both IBC and PERT.

In Figure 3.11, the PR_{mod}^a and $PR_{mod,T \rightarrow 25}^a$ of the tandem do not show a considerable change between the first and second years. The a-Si shows the worst performance with respect to the other TF technologies since a high $P_{M,exp}^*$, possibly still unstabilized value, was taken as a reference at the beginning of its exposure. So, it can be seen that there was a decrease in PR_a in the second year due to stabilization. The CIGS module has a better performance than the other TF technologies. It shows a small decrease of < 1% in PR_{mod}^a and $PR_{mod,T \rightarrow 25}^a$ between the first and second years.

Figure 3.12 shows the PR_{mod}^a with respect to the P_M^* values in STC for c-Si technologies. The HIT and Al-BSF show a similar PR_{mod}^a and $PR_{mod,T \rightarrow 25}^a$ in the first and second years. The IBC showed a reduction of 1.4 and 1.9 of the PR_{mod}^a and $PR_{mod,T \rightarrow 25}^a$, respectively. PERT shows a better performance of PR_{mod}^a and $PR_{mod,T \rightarrow 25}^a$ in the first and second year. This could be due to the fact that, as could be seen in the calibrations in Table 3.6, PERT showed a deviation of less than 2% with respect to P_M^* . Therefore, this behavior could have been extended throughout the year.

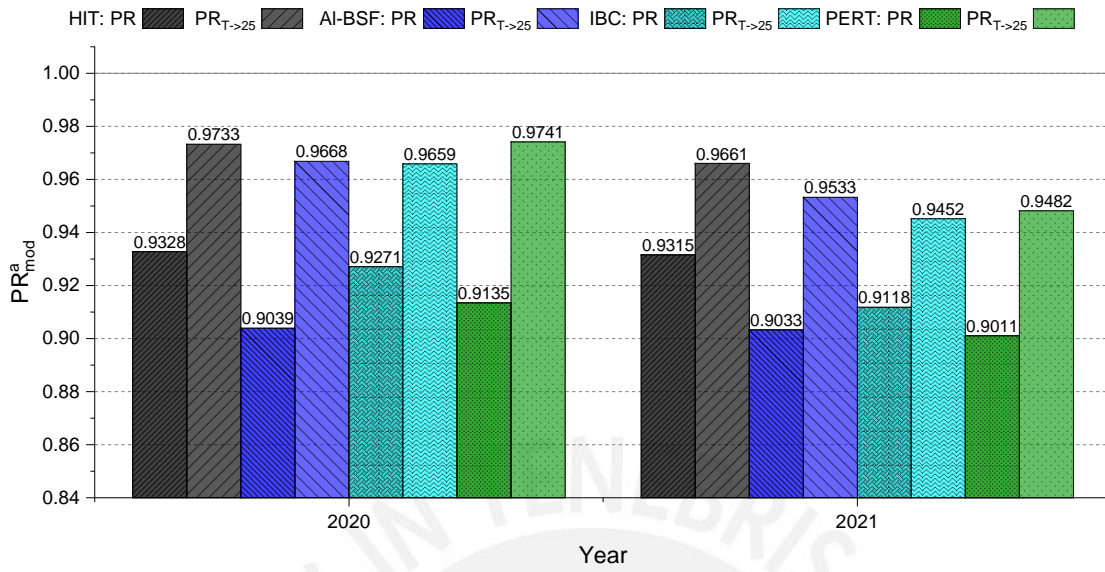


Figure 3.10: PR_{mod}^a and $PR_{mod,T \rightarrow 25}^a$ for c-Si technologies with respect to $P_{M,exp}^*$ from March 2020.

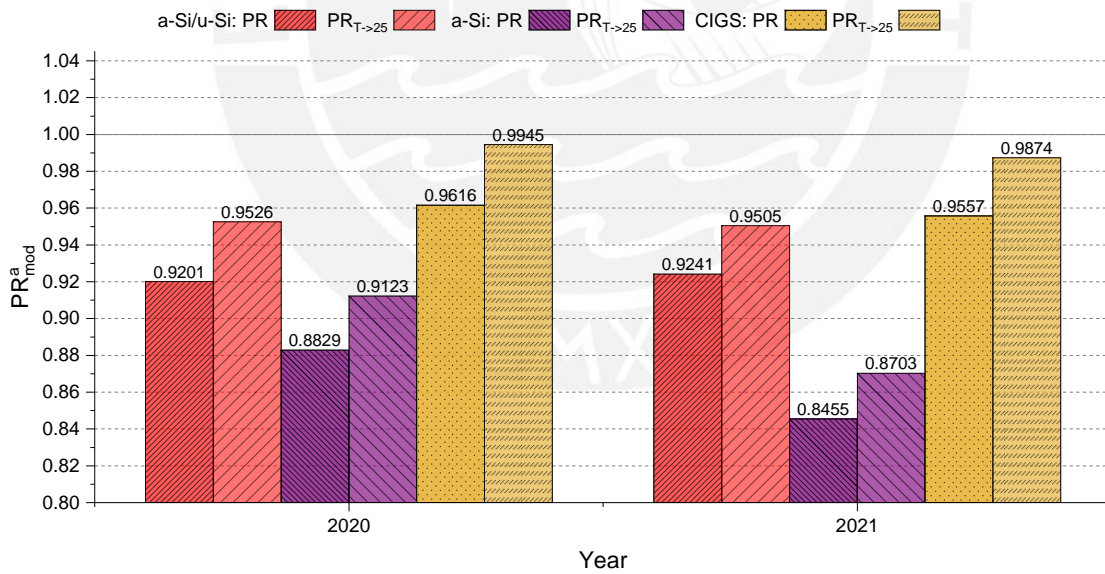


Figure 3.11: PR_{mod}^a and $PR_{mod,T \rightarrow 25}^a$ for TF technologies with respect to $P_{M,exp}^*$ from March 2020.

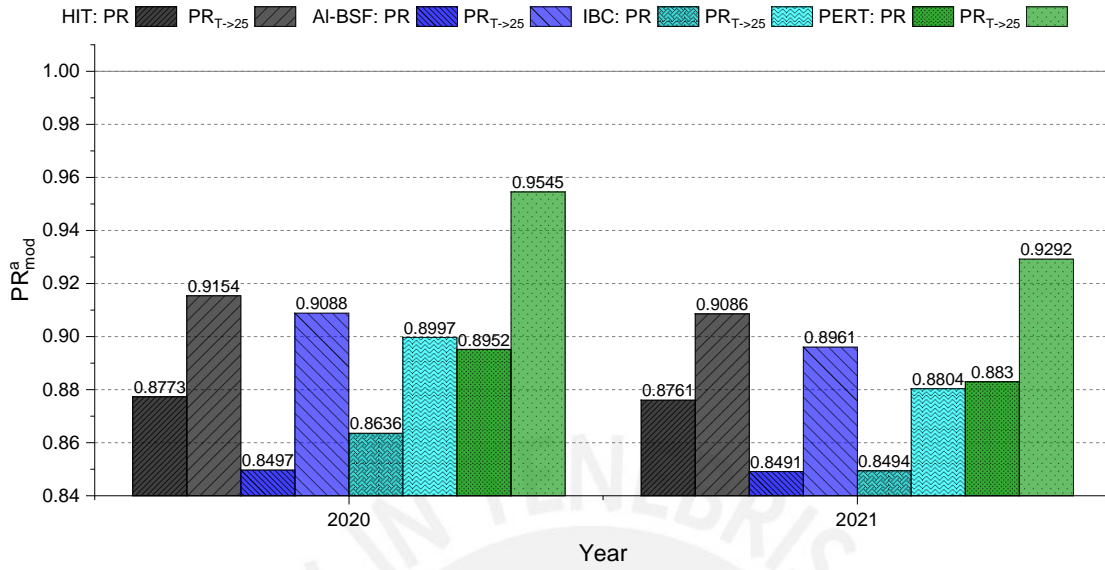


Figure 3.12: PR_{mod}^a and $PR_{mod,T \rightarrow 25}^a$ for c-Si technologies with respect to P_M^* in STC.

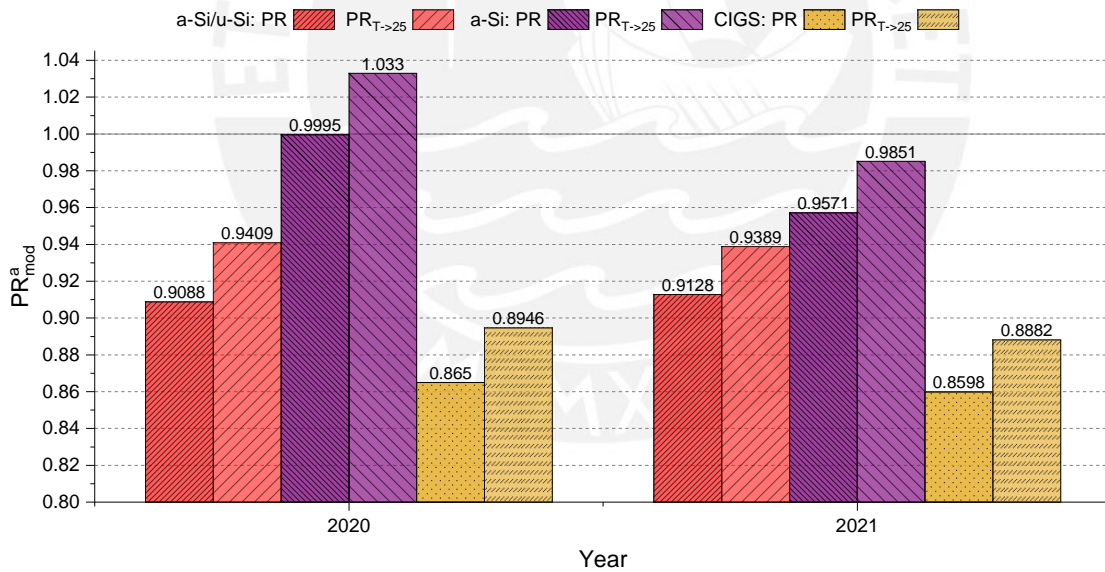


Figure 3.13: PR_{mod}^a and $PR_{mod,T \rightarrow 25}^a$ for TF technologies with respect to P_M^* in STC.

Figure 3.13 shows the PR_{mod}^a with respect to the P_M^* values in STC for TF technologies. The a-Si had the best performance and showed values of PR_{mod}^a and $PR_{mod,T \rightarrow 25}^a$ equal to and greater than 1, respectively, in the first year; since this module presented high P_M with respect to P_M^* in its first months of exposure. In the second year, PR_{mod}^a and $PR_{mod,T \rightarrow 25}^a$ decrease can

be seen due to stabilization processes. The a-si/ μ c-Si tandem shows an intermediate PR_{mod}^a between a-Si and CIGS and does not change between the first and second years. The CIGS module has a lower performance compared to the other TF technologies. It does not show a considerable variation in PR_{mod}^a and $PR_{mod,T \rightarrow 25}^a$ between the first and second years.

3.5 Conclusions

In this chapter, as a previous step to carry out any analysis of performance and characterization of different PV technologies, an experimental calibration process of the electrical parameters of the PV modules has been carried out in the climate conditions of Lima. This analysis confirmed that the experimental outdoor results reasonably comply with the indoor data of electrical parameters provided by the module manufacturers.

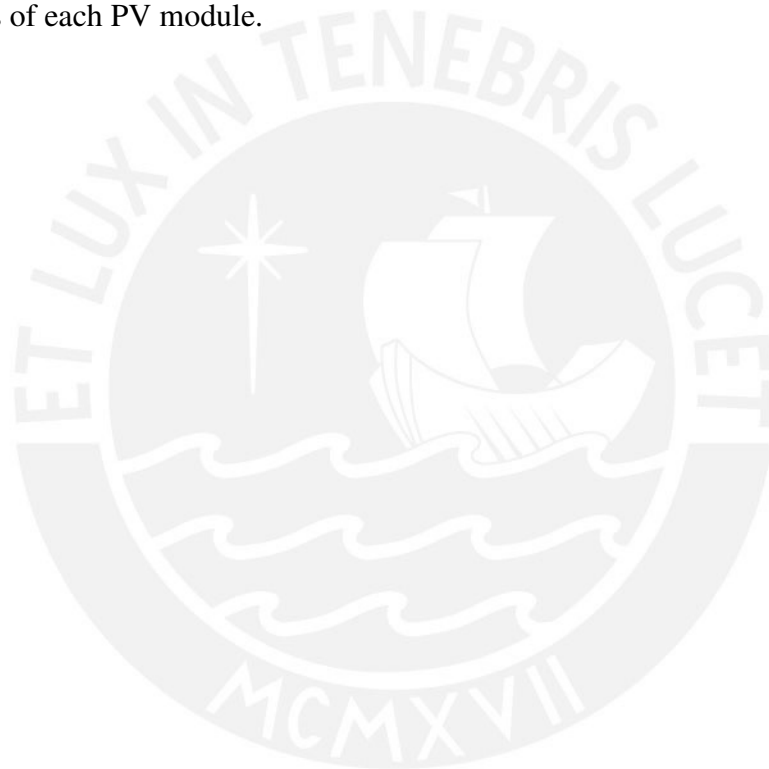
An experimental study has been carried out for the period between May 2019 to July 2019 to investigate the applicability and validity of two analytical methods: Osterwald and Constant Fill Factor. When comparing the modeled powers with the experimental measurements, the indexes of linear correlation (≈ 1) and of coefficient of determination ($R^2 > 0,98$) indicate good reliability of the prediction of the methods. Furthermore, the correction factors were > 1 for Tandem a-si/ μ c-Si and < 1 for Al-BSF and HIT. This indicated that the applied methods for modeling power might underestimate for Tandem and overestimate for Al-BSF and HIT in local climatic conditions.

For the period between March 2020 to February 2022, the energy conversion efficiency of seven different PV technologies was analyzed utilizing the PR . The analysis was made considering the calibrated nominal power and correcting it in temperature. Other losses, such as spectral response, angular response, or soiling, are not considered. Annually it was found that modules based on c-Si (HIT, Al-BSF, PERT, and IBC) showed a more significant loss in temperature than technologies based on TF (Tandem a-si/ μ c-Si, a-Si, and CIGS).

During this period, there was no continuous cleaning campaign. This could cause more

significant uncertainty in the measurement of the module temperature and irradiance. So these results will mainly be affected by irradiance levels, module temperature, and dust deposition. A deeper analysis is required, including other types of loss such as spectral effects, soiling, angles of incidence, and degradation. Also, analyzing other electrical parameters such as, I_{SC} , V_{OC} , FF , and efficiency to detect significant changes in any of these.

Finally, an indoor characterization with a solar simulator is necessary for a more complete study. An electroluminescence analysis could also be performed to find out the internal fractures and damaged cells of each PV module.



Chapter IV

Spectral analysis and characterization

4.1 Introduction

In the previous chapter, an analysis of the losses from temperature and irradiance in energy conversion efficiency was made. This chapter analyzes the ground-based, spectrally-resolved experimental irradiance data taken with a spectroradiometer experimentally monitored during one year (March 2019-February 2020) and studies the influence that the spectrum exerts on the performance of different PV module technologies. The spectral distribution of the irradiance varies according to location, time of day, and season [53]. It is mainly affected by the air mass (AM), aerosol optical depth (AOD), and precipitable water (PW, in cm) [54]. Modeling software, such as SMARTS2 (Simple Model of Atmospheric Radiative Transfer of Sunshine), can simulate spectral distributions; however, these require a good quality atmospheric input data to ensure simulation accuracy [55].

The effects of spectral variations on the energy yield have been investigated in several places, for example, Freiburg (Germany) [56], Madrid (Spain) [57], Jaen (Spain) [52], Rome (Italy) [58], Kusatsu (Japan) [59], Singapore [60], Phitsanulok (Thailand) [61], Assu and Florianópolis (Brazil) [62], Sao Paulo (Brazil) [63], and a more recent study where a world experimental and simulated analysis was done in more than 28 locations [64].

The studies mentioned above have mostly been made in mid- and high- latitude locations, which present considerable climatic variation throughout the year, except for Singapore, Thai-

land, and Brazil. Few studies have reported on the spectral effects for low-latitude sites with desert-coastal climatic conditions, such as Lima [33][64][65][66].

Two indexes were used to quantify the spectral distribution and its impact on PV performance in this chapter: The average photon energy (APE) and the spectral mismatch factor (MM). The APE is calculated as a representative parameter to evaluate the spectral distributions and the MM enables an estimation of the spectral gains of distinct PV technologies.

4.2 Methodology

4.2.1 Extrapolation of spectra

The wavelength range of the spectroradiometer EKO MS-711 is between 300-1100 nm. It was extrapolated to a full spectral distribution of 300-4000 nm following the methodology in [67], which was also employed in [52], [68], and [69].

Figure 4.1 and Figure 4.2 show an experimental spectrum ($E(\lambda)$) and the standard AM1.5G spectrum ($E^*(\lambda)$) with the shaded areas A and A^* between 700 nm and 1100 nm, respectively. R is equivalent to:

$$R = \frac{A}{A^*} \quad (4.1)$$

The extrapolated section of E is equal to the multiplication of the constant R at each value of the spectrum E in the range of 1100-4000 nm.

$$E_{ext}(\lambda = 1100 - 4000 \text{ nm}) = R \times E^*(\lambda = 1100 - 4000 \text{ nm}) \quad (4.2)$$

Figure 4.3 shows the complete spectrum between 300-4000 nm, where the experimental spectrum meets the extrapolated spectrum.

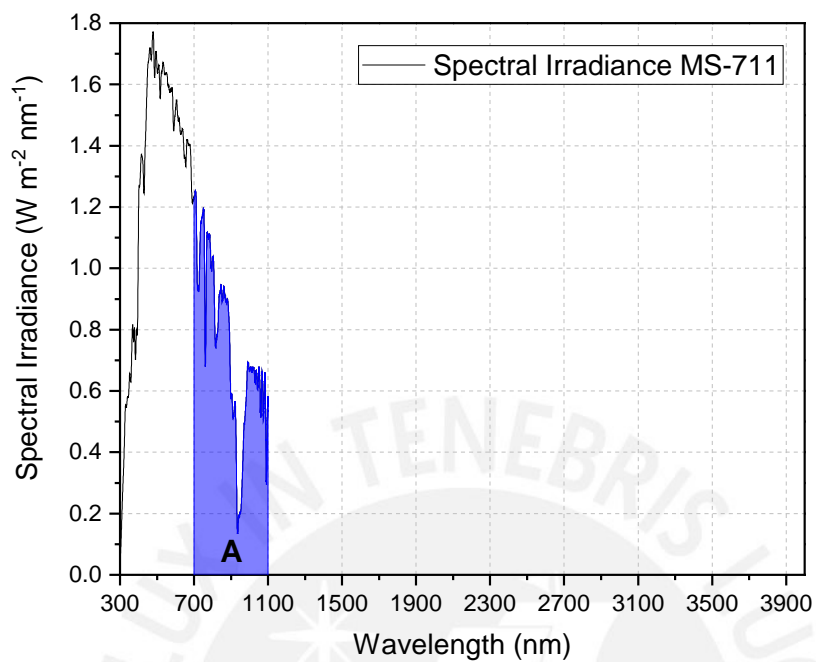


Figure 4.1: Shaded area between 700-1100 nm of an experimental spectrum.

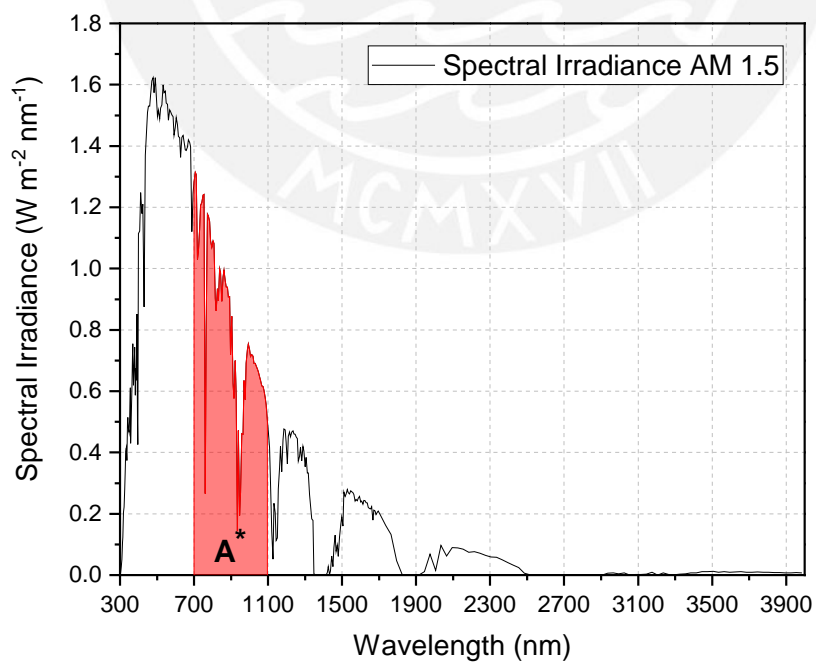


Figure 4.2: Shaded area between 700-1100 nm of AM1.5G spectrum.

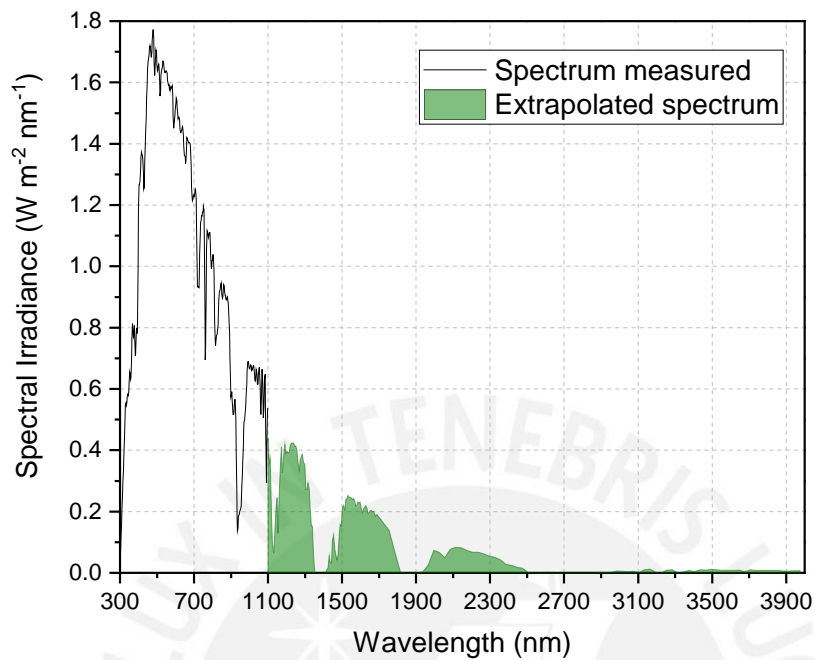


Figure 4.3: Resulting extrapolated experimental spectrum.

4.2.2 Gaussian Fit

Figure 4.4 shows the relative spectral responses (SR_r) of seven PV modules that were used in this work: Amorphous silicon (a-Si), Perovskite, Cadmium telluride (CdTe), multi-crystalline silicon (multi-Si), Copper indium gallium selenide with different bandgaps from two manufacturers (CIGS-1 and CIGS-2), monocrystalline silicon (mono-Si), and the normalized spectral irradiance AM1.5G. The PV modules' spectral responses have different bands of absorption that vary according to manufacturing technology and material [70]. The spectral responses were adjusted using Gaussian functions. Since the spectral response of any PV device fits very well with Gaussian functions, as demonstrated in [71]. See APPENDIX 2 for more information on each spectral response's Gaussian fit procedure.

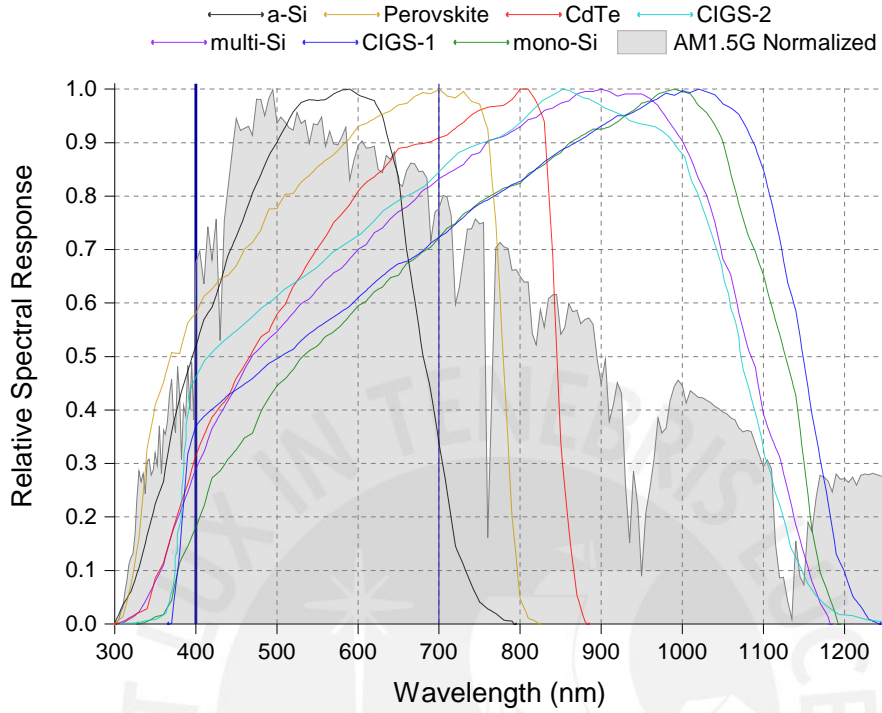


Figure 4.4: Relative spectral responses of PV modules and the normalized spectral irradiance AM1.5G.

4.2.3 Angle of incidence

The cosine of the AOI for a north-facing surface in the southern hemisphere is [72]:

$$\cos(AOI) = \sin(L + \beta) \sin(\delta) + \cos(L + \beta) \cos(\delta) \cos(h) \quad (4.3)$$

where L is the local latitude ($12^{\circ}4'17.85''S$), β is the surface tilt angle from the horizontal (20°), δ is the solar declination, and h is the hour angle. To reduce the influence of high AOI in PV modules, such as the increased surface reflection [73] or the decrease of light coupled [74], measurements with an AOI over 50° were discarded.

4.2.4 Average Photon Energy

Average Photon Energy (APE) [eV], which Jardine [75] and Williams [76] first introduced, quantitatively characterizes a spectral distribution by a single parameter. It is calculated by dividing the integral of the spectral irradiance by the integral of the photon flux:

$$APE = \frac{\int_{\lambda_a}^{\lambda_b} E(\lambda) d\lambda}{q \int_{\lambda_a}^{\lambda_b} \phi(\lambda) d\lambda} \quad (4.4)$$

where q is the electron charge constant (1.602×10^{-19} C), $\phi(\lambda)$ [$\text{m}^{-2} \text{nm}^{-1} \text{s}^{-1}$] is the photon flux density, λ_a [nm] and λ_b [nm] are the lower and upper wavelength integration limits. The integration intervals were considered between 350 nm and 1050 nm in this work. The APE in this interval for the standard AM1.5G spectrum ($APE_{AM1.5G}$) is 1.880 eV, so that this value is taken as a reference. When APE is higher or less than 1.880 eV, the spectral distribution is considered blue-rich/shifted, and red-rich/shifted, respectively.

Figure 4.5 shows three instances of measured solar spectra and the standard AM1.5G. These three spectra correspond to dates of different seasons in Lima: Summer (11-Feb-2020), Autumn (04-May-2019), and Winter (22-Aug-2019) with APE values of 1.924 eV, 1.912 eV, and 1.904 eV, respectively. These were taken around noon under clear skies when the pyranometer simultaneously measured a broadband irradiance of $(1000 \pm 2) \text{ W m}^{-2}$.

The exemplary measured spectral distributions are blue-shifted with respect to the standard AM1.5G spectrum, as seen in their respective APE values. The blue shift can be clearly observed in the respective irradiance distributions: short-wavelengths -below ~ 650 nm in the UV and VIS- are enhanced when compared to long-wavelengths -above ~ 700 nm in the IR [77].

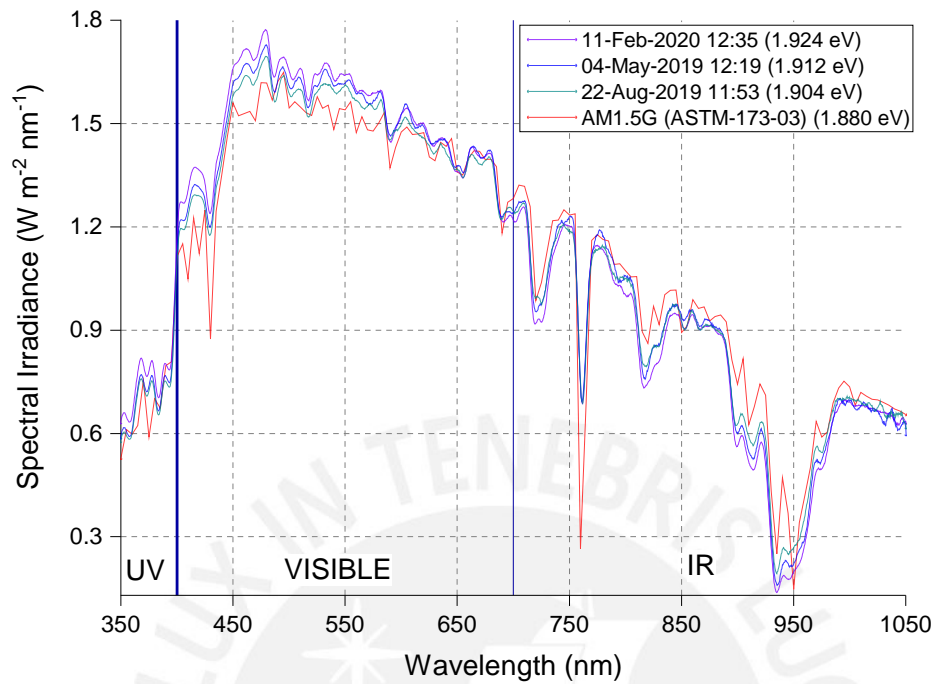


Figure 4.5: Examples of spectral irradiance distributions measured in Lima.

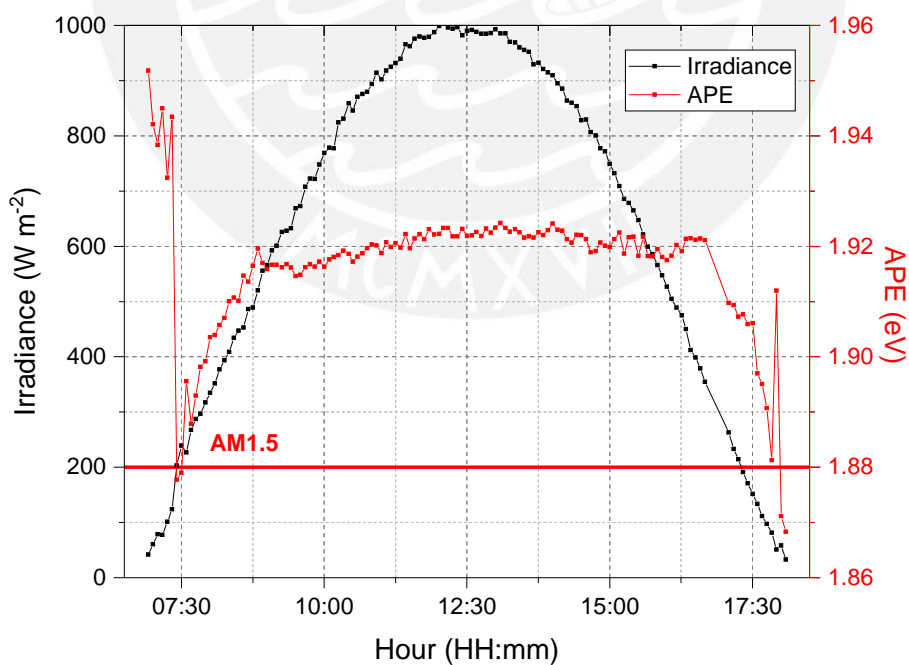


Figure 4.6: Irradiance and *APE* for a sunny day in Lima.

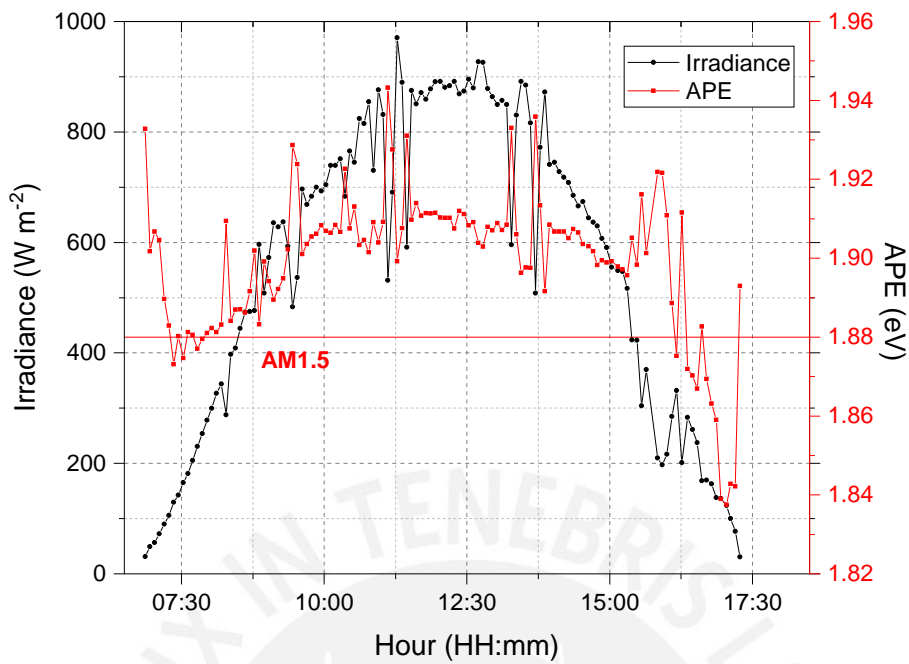


Figure 4.7: Irradiance and APE for a partially cloudy day in Lima.

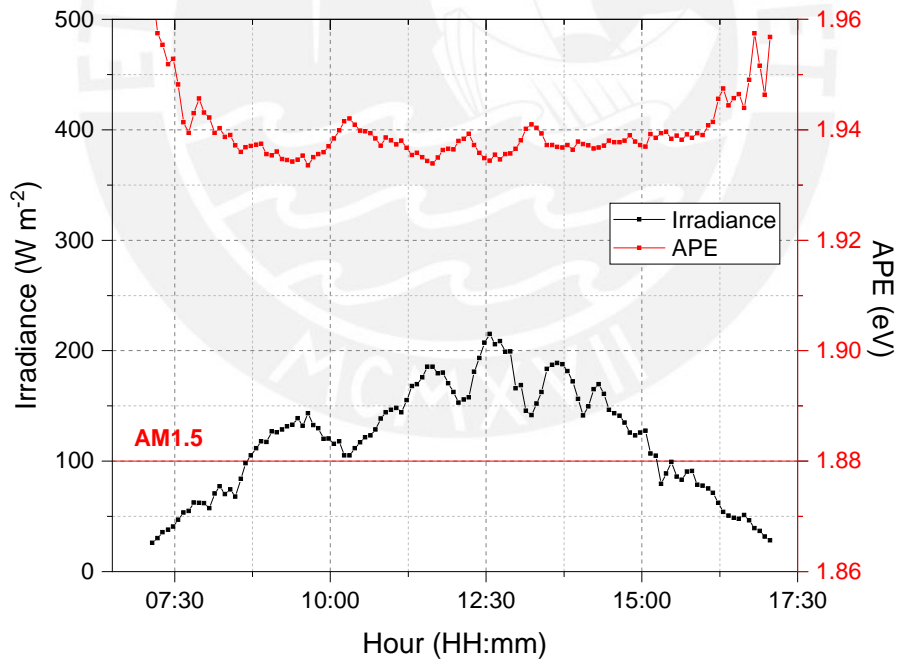


Figure 4.8: Irradiance and APE for a cloudy day in Lima.

The figures 4.6, 4.7, and 4.8 compare the irradiance measurement with the APE on a clear, partly cloudy, and cloudy day, respectively. For the three cases, the APE is always above the $APE_{AM1.5G}$. For the sunny day, the irradiance measurements present a well-defined curve. The

APE presents high and low values at sunrise and sunset, respectively. For intermediate hours of the day, between 9 and 5 hours, the *APE* presents an almost constant value of 1.920 eV. For the partially cloudy day, when there are drops in the irradiance values, mainly due to clouds, peaks in the *APE* are observed. On cloudy days, with maximum irradiances of 200 W m^{-2} , the *APE* remains at average values of 1.940 eV.

4.2.5 Spectral Mismatch Factor

The Spectral Mismatch Factor (*MM*), according to the IEC 60904-7 standard [78], allows the quantification of spectral gains between a reference device and a test device. When the reference is a pyranometer, *MM* is given by:

$$MM = \frac{\int_{\lambda_1}^{\lambda_2} E(\lambda) SR_r(\lambda) d\lambda \int_{\lambda_3}^{\lambda_4} E^*(\lambda) d\lambda}{\int_{\lambda_1}^{\lambda_2} E^*(\lambda) SR_r(\lambda) d\lambda \int_{\lambda_3}^{\lambda_4} E(\lambda) d\lambda} \quad (4.5)$$

where $SR_r(\lambda)$ is the relative spectral response of the PV device under test, λ_1 [nm] and λ_2 [nm] are the lower and upper limits of the wavelength, respectively, where the PV device is spectrally active, λ_3 [nm] and λ_4 [nm] are the lower and upper limits of the full-range spectral distribution (300-4000 nm). *MM* values that are greater or less than 1 indicate a spectral gain or loss, respectively.

To estimate the spectral gains of a PV system on daily, monthly, and annual timescales [68], equations 4.6, 4.7, and 4.8 were used to express the *MM* weighted with the broadband irradiance *G* at daily, monthly, and annual intervals, respectively:

$$MM_d = \frac{\sum_{i=1}^{N_d} MM_i \cdot G_i}{\sum_{i=1}^{N_d} G_i} \quad (4.6)$$

$$MM_m = \frac{\sum_{i=1}^{N_m} MM_i \cdot G_i}{\sum_{i=1}^{N_m} G_i} \quad (4.7)$$

$$MM_a = \frac{\sum_{i=1}^{N_a} MM_i \cdot G_i}{\sum_{i=1}^{N_a} G_i} \quad (4.8)$$

where MM_i is the instantaneous mismatch factor calculated according to equation 4.5. From MM_d , MM_m , and MM_a , the spectral gains are given by:

$$\text{daily spectral gains} = (MM_d - 1) \times 100 \% \quad (4.9)$$

$$\text{monthly spectral gains} = (MM_m - 1) \times 100 \% \quad (4.10)$$

$$\text{yearly spectral gains} = (MM_a - 1) \times 100 \% \quad (4.11)$$

For example, a MM_d , MM_m or MM_a value of 1.02 indicates that the PV module should have an estimated spectral gain of 2% in its energy production during the respective time interval, with respect to the reference spectral irradiance AM1.5G.

4.3 Average Photon Energy in Lima Results

Figure 4.9 shows a histogram of the APE_i values (class width = 0.01 eV) of the 23,000 spectra measured for one year. The highest percentage of data (around 40%) occurs within 1.920-1.930 eV, and a negligible amount of values were found close to the $APE_{AM1.5G}$ (1.880-1.890 eV). This implies that the blue-shifted spectra prevail in Lima and that spectra with a distribution similar to the AM1.5G spectrum will rarely be found in Lima.

Figure 4.10 shows the APE_d (blue points), APE_m (green points), and APE_a (black line) in one year. The time axis is divided into months and seasons. All APE_d , APE_m and APE_a values are well above $APE_{AM1.5G} = 1.880$ eV (red line), for instance, the value of $APE_a = 1.923$ eV.

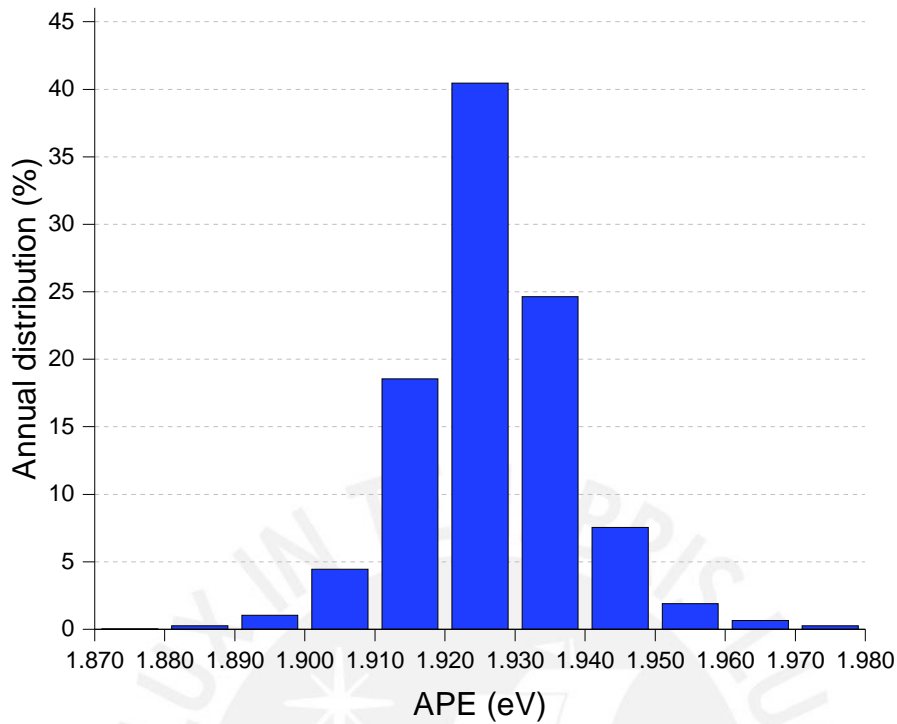


Figure 4.9: Annual distribution of APE_i of about 23,000 spectra recorded from March 2019 to February 2020 as a function of APE .

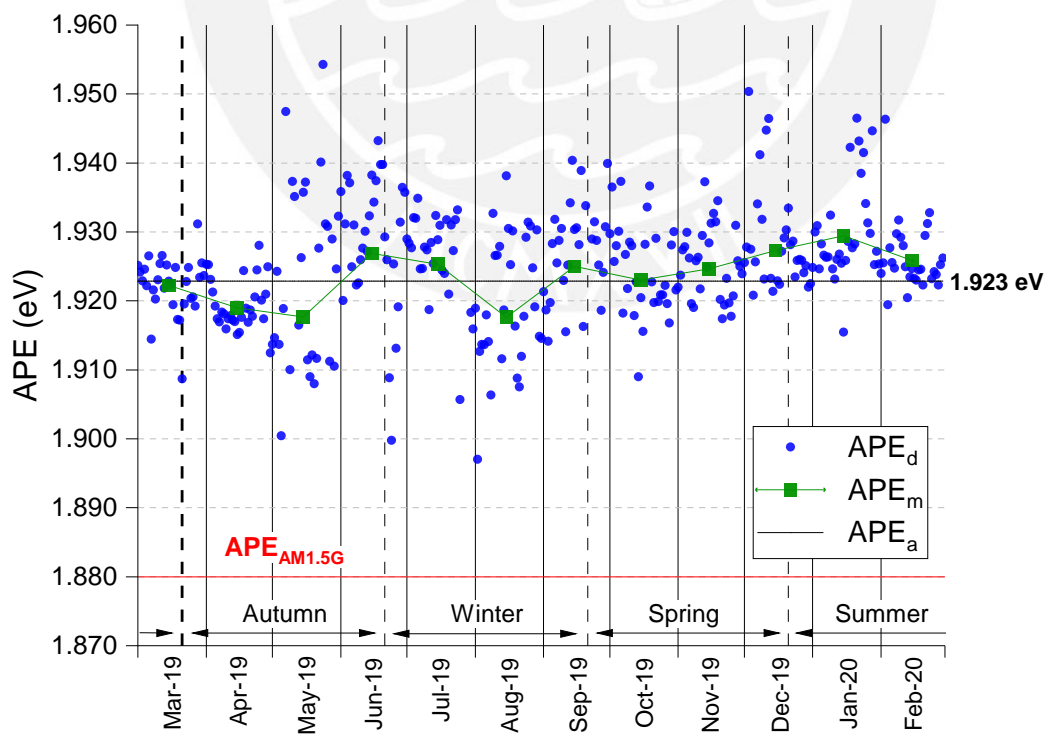


Figure 4.10: Daily, monthly and annual irradiance weighted APE in one year.

During spring and summer months the APE_d and APE_m values are mostly above APE_a . During these months, clear skies and higher irradiances dominate Lima's climate [79]. With the higher sun elevation, lower AM values predominate, thus, favoring the passage of blue-rich spectra to the surface [80].

By contrast, during autumn and winter months, lower APE_d and APE_m values are expected due to the lower sun's elevation, which is conducive to an increase of AM values [62]. For April, May, and August, this is the case when the APE_m values are below the APE_a . With exception to the months of June and July, when the APE_m values are above the APE_a . This is probably caused by the predominant dense cloud cover in Lima between June and November [81]. This dense cloud cover acts as a filter for infrared radiation and increases the diffuse irradiance component, thus causing a blue-bias effect in the spectrum, as reported in [82] and [83].

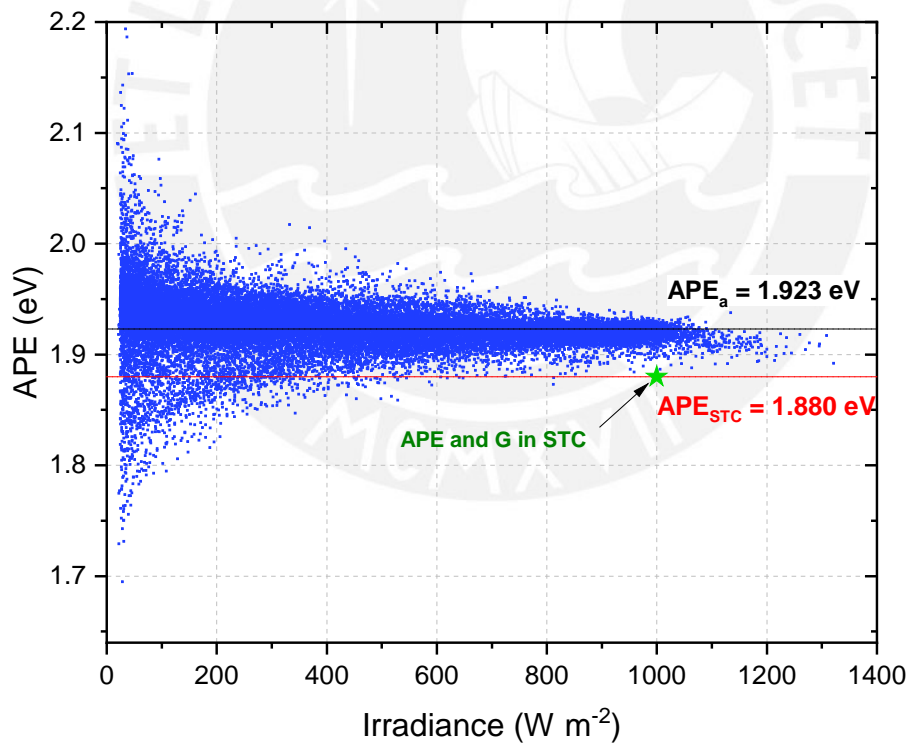


Figure 4.11: APE_i with respect to G_i . The APE_a and $APE_{AM1.5G}$ are indicate as reference.

The highest APE_m value was found in January (1.929 eV), -the beginning of summer- and June (1.927 eV), -the end of autumn-. The lowest APE_m values (1.918 eV) were found in May

and August, mid-autumn, and mid-winter, respectively. The difference between the maximum and minimum monthly value of the APE_m is 0.011 eV. This implies that no clear seasonality of APE_m throughout the year is observed in Lima.

Figure 4.11 shows the APE_i with respect to the experimental values of the G_i . This graph indicates APE_a (black line) and $APE_{AM1.5G}$ (red line). Most of the APE_i are concentrated close to the APE_a values, while very few measurements are close to STC conditions. At low irradiances, the APE_i presents maximum and minimum values around 2.150 eV and 1.700 eV, respectively.

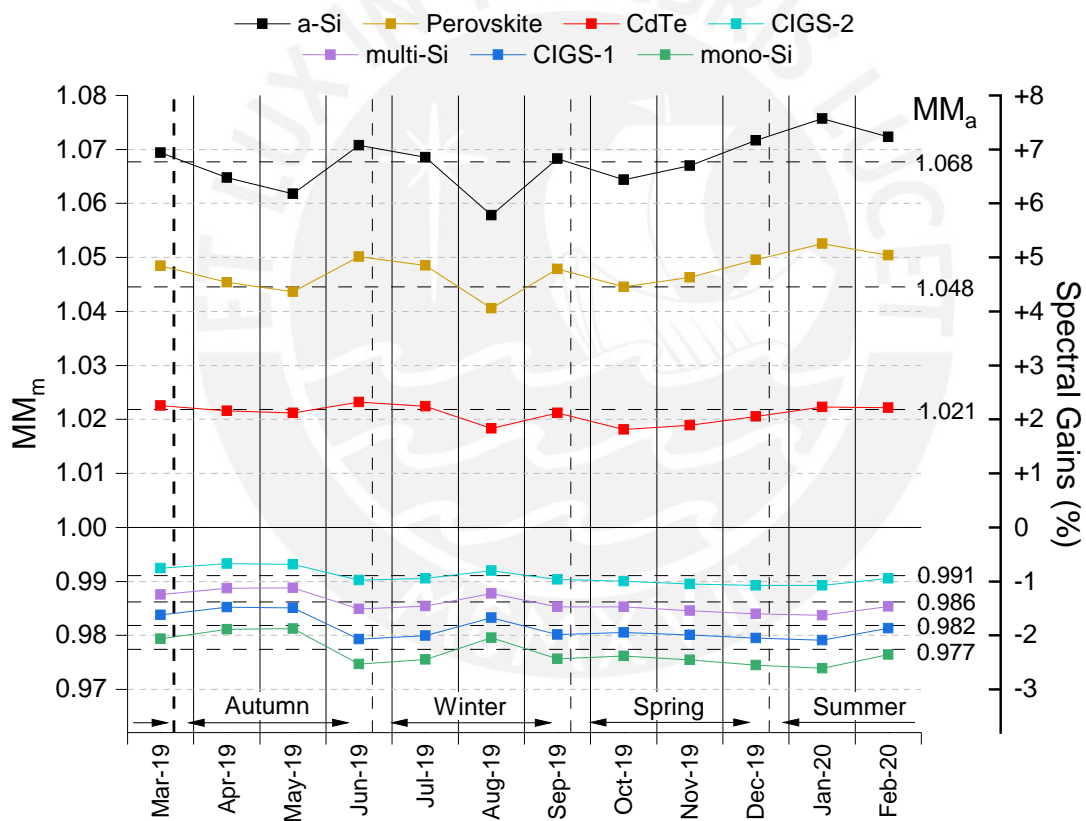


Figure 4.12: Monthly and annual MM averages evaluated for different PV technologies in one year in Lima.

4.4 Spectral Mismatch Factor for PV modules Results

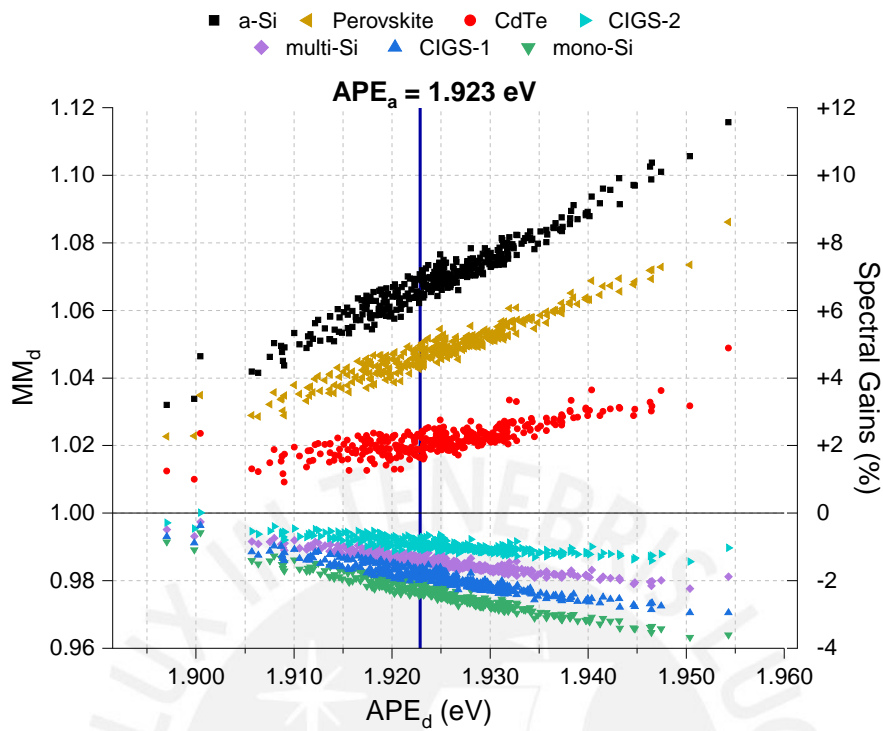
Figure 4.12 shows the values of MM_m (solid lines) and MM_a (dashed lines) for the seven PV technologies studied in Lima in one year. The time axis is divided into months and seasons.

The highest value of $MM_m = 1.076$ was reached by a-Si in January, which corresponds to a spectral gain of 7.6 %, and by the Perovskite with $MM_m = 1.053$ and, thus, a spectral gain of 5.3 %, when also the highest $APE_m = 1.929$ eV was found (Figure 4.12). In contrast, the lowest MM_m and spectral gain for a-Si (5.8 %) and Perovskite (4.1 %) was found in August, when the $APE_m = 1.918$ eV was lowest. The values of MM_m for CdTe, CIGS-2, multi-Si, CIGS-1, and mono-Si showed small variations with respect to the MM_a value in each PV technology. Therefore, not much variation or seasonal behavior was found for any PV technology.

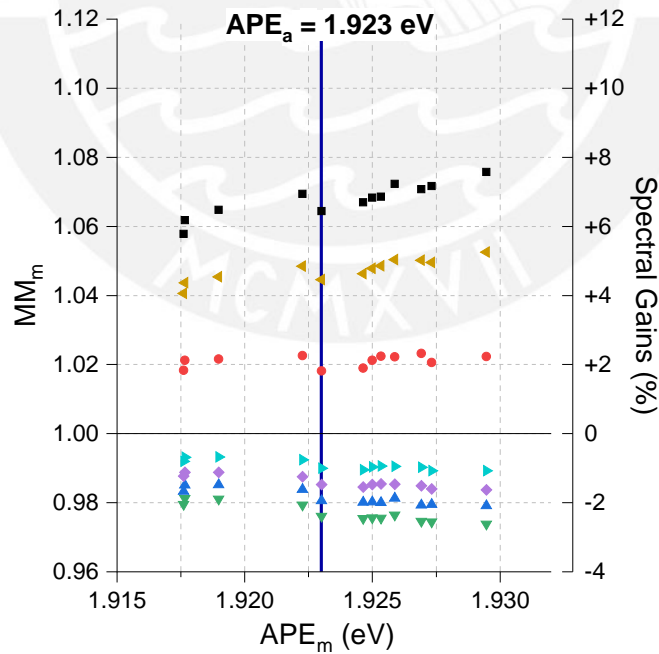
On a yearly basis, a-Si shows the highest $MM_a = 1.068$, which corresponds to a spectral gain of +6.8 %, followed by Perovskite with $MM_a = 1.048$ (+4.8 %) and CdTe with $MM_a = 1.021$ (+2.1 %). On the other hand, CIGS-2, multi-Si, CIGS-1, and mono-Si technologies exhibit annual spectral losses. CIGS-2, with $MM_a = 0.991$, shows the lowest spectral loss of -0.9 %, followed by multi-Si with $MM_a = 0.986$ (-1.4 %), CIGS-1 with $MM_a = 0.982$ (-1.8 %) and mono-Si with $MM_a = 0.977$ (-2.3 %). These results are similar to the simulations reported in [84], where this effect is attributed to environmental conditions and the location that produce spectra rich in blue.

If spectral effects are only considered –although the analysis applied here cannot be used for double-junction PV technologies [60]– this could well explain the good performance of a-Si/ μ c-Si tandem TF PV installations in Lima, as reported in [13] and [31].

Figure 4.13 shows MM vs. APE to study a possible correlation. This graph correlates APE_d with MM_d (Figure 4.13a) and APE_m with MM_m (Figure 4.13b), where a quasi-linear relationship was found. This relationship was also found experimentally in [52], [85], [86], and [87].



(a)



(b)

Figure 4.13: Correlation between the APE and MM weighted by irradiance of each PV technology with (a) daily and (b) monthly values. The APE_a is indicate as a reference.

Figure 4.13a shows that the increase in APE_d significantly influences the MM_d gains in a-Si, followed by Perovskite and CdTe. On the contrary, for CIGS-2, multi-Si, CIGS-1, and mono-Si, when APE_d increases, their MM_d decrease [88]. If the APE increases, it has higher blue components in the spectrum, so the performance of technologies with SR_r (Figure 4.4) biased towards shorter wavelengths would benefit. This is the case for a-Si, CdTe, and Perovskite. Whereas when SR_r is biased towards longer wavelengths, it would benefit from a red-shifted APE , as is the case for CdTe, CIGS-2, multi-Si, CIGS-1, and mono-Si [89].

Figure 4.13b relates the values of MM_m and APE_m . Here, a similar tendency can be observed as for daily values. This relationship could be used to estimate the MM_m and MM_a for other months and year intervals that are not shown in this study, from only the APE_m and APE_a data for these months and year intervals, respectively. Therefore, the APE for the case of Lima could be a good indicator of the spectral impact on the performance of PV modules of different technologies [90], although this is still under discussion for different locations [56][91].

4.5 Conclusions

In this chapter, the spectral impact on different PV technologies in Lima-Peru, was investigated. Through an experimental campaign of one year (March 2019-February 2020), the spectral distribution was characterized using the APE .

It was found that the APE_a has a value of 1.923 eV, which is well above the $APE_{AM1.5G}$ (1.880 eV). The APE_m values show small variations between months and seasons. Thus, it can be concluded that Lima has a spectrum with a blue shift throughout the year with scarcely relevant seasonality. This is in contrast to similar studies performed at other locations in the world, particularly at higher latitudes. We propose that this almost absent seasonality can be attributed to the relatively low latitude and, thus, low AM of Lima during the predominantly sunny summer and spring months, as well as its particular climate with prevailing cloudy autumn and winter months. Hence, these conditions are conducive to blue-biased spectral distributions dur-

ing all seasons.

The influence of the spectral distribution on the performance of seven different PV technologies was evaluated utilizing MM . In MM_a , this leads to positive spectral gains of +6.8 %, +4.8 %, and +2.1 % for a-Si, Perovskite, and CdTe, respectively. Spectral annual gains turn negative for lower-bandgap materials. Specifically, -0.9 %, -1.4 %, -1.8 %, and -2.3 % are found for CIGS-2, multi-Si, CIGS-1, and mono-Si, respectively. As discussed above, such results are attributable to the prevailing blue-shifted spectra in Lima.

The correlation between APE_d-MM_d and APE_m-MM_m was evaluated, where a quasi-linear behavior was found. The influence of the APE variation in MM is due to the spectral response and the band-gap of each PV technology. This quasi-linear relationship between the APE_d and MM_d may allow to estimate the MM_m and MM_a for any month or annual interval.

Since the spectral effects do not present either a considerable variation or a seasonal behavior, these results could be considered as a constant to estimate the spectral gains in the performance ratio of PV installations in Lima. To better understand the insignificant seasonality of the parameters studied in Lima, a more extensive experimental campaign is being carried out considering other environmental conditions such as the diffuse spectral irradiance ratio.

Chapter V

Conclusions and Future Lines

This section shows the conclusions reached in the development of this Doctoral Thesis and also the future lines of research. These conclusions are related to the objectives and hypotheses that were raised in the introduction.

The general objective was to implement an Outdoor-PV Laboratory at the PUCP to investigate PV technologies' performance behavior in Lima-Peru, which was successfully achieved.

This Outdoor-PV Laboratory is the country's first to have the appropriate instrumentation to perform calibration processes and energy rating of PV modules, under the operating climate conditions of the city of Lima. By the end of this thesis, there are 12 PV technologies installed, such as c-Si, TF, and bifacial modules, of which seven were analyzed for this work.

With respect to the specific objectives, an outdoor calibration was carried out with three different PV technologies. The resulting experimental nominal power of the modules was reasonably close to the nominal power at STC reported by the manufacturer, thus, confirming the validity of the measured electrical parameters, irradiance, and module temperature by the monitoring system. Furthermore, in terms of long-term maximum power monitoring, the two simple models by Osterwald and Constant Fill Factor gave very reasonable predictions, confirming the suitability of the monitoring system for long-term characterization as well.

For long-term energy rating, the instantaneous PR was analyzed for two years. To this end, an initial calibration was made to obtain the experimental nominal power of seven PV modules, four based on c-Si and three on TF technologies. In general, the c-Si technologies showed monthly PR_{mod}^m with a slight seasonal variation of $\pm 2.65\%$, and the TF technologies showed a slight oscillatory variation of $\pm 1.89\%$. In both cases, the oscillations were predominantly caused by temperature differences between the summer and winter. The a-Si technology showed initial signs of gradual stabilization, possibly degradation. After the temperature corrections, the oscillations of the $PR_{mod,T \rightarrow 25}^m$ were further reduced for c-Si technologies to $\pm 1.89\%$ and, demonstrating relatively stable performances throughout both years.

The characterization of the solar spectrum for one year demonstrated that the Spectrum in Lima is blue-shift with respect to the AM1.5G spectrum. This is likely due to the low latitude and the cloudy winter sky. The monthly irradiance-weighted APE showed slight seasonal variation, the same as the monthly irradiance-weighted MM for the seven evaluated PV technologies. This is in accordance with the slight variation also observed in the monthly $PR_{mod,T \rightarrow 25}^m$. On the one hand, the blue-shifted solar spectrum favors PV technologies with larger bandgaps, such as a-Si and Perovskite. On the other hand, c-Si and CIGS technologies experience a slight spectral loss due to their smaller band gap.

The development and implementation of the research laboratory made it possible to carry out characterization studies of different PV technologies for the first time in Lima. Based on these first promising results, future lines of research have been established.

Figure 5.1 shows the state of the Outdoor-PV Laboratory at the end of this thesis, composed of three stations. The measurement system described in chapter 2 of this thesis is the first station. Currently, in the I-V curve tracer, 10 PV modules are being analyzed, as recently, a PERC PV module and two mono-Si PERC bifacial PV modules were added. Figure 5.2a and Figure 5.2b shows four EKO MS-80M digital pyranometers, were added to measure irradiance tilted at 15° , albedo, and east and west directions.



Figure 5.1: PV Research Laboratory at PUCP.

The second station are three grid-connected systems of three PV technologies (HIT, PERC, and CIGS). This system has been replicated in five different regions of Peru (Lima, Arequipa, Chachapoyas, Puno and Tacna). The objective is to compare the performance of PV systems under different climates. The acquisition software is based on the software that was previously developed in the first station.

The third station is a bifacial PV module system (Figure 5.2a and Figure 5.2b). In this system, the PV modules are in two different positions, tilted 15° to the north and vertically to the east-west. The objective is to know the behavior of the bifacial modules under the climatic conditions in Lima for different positions. For the evaluation, pyranometers were also included in different positions for a correct analysis. Irradiance measurements from digital pyrometers were also added to the first station's software to a synchrony between all measurements.



(a)



(b)

Figure 5.2: (a) Vertical and (b) tilted, bifacial PV modules and pyranometers.

Finally, an automatic shading system was installed to the EKO MS-711 spectroradiometer to measure the diffuse horizontal spectrum, and a MS-80S digital pyranometer with a shadow ring was installed to measure the diffuse horizontal irradiance, as seen in Figure 5.3. The irradiance and diffuse spectrum measurement software was also adapted and added to the software of the first station.



Figure 5.3: Diffuse horizontal measurement systems of the solar spectrum and irradiance.

Figure 5.4 shows the schematic diagram of the current state of the entire Outdoor-PV Laboratory. The Laboratory is automated and adapted, by the software that was developed, for continuous measurements of different instruments and PV systems throughout the day. Therefore, the laboratory has become even more versatile for PV research and adaptable for different analyses. One future aim will be to achieve accreditation for PV module characterization.

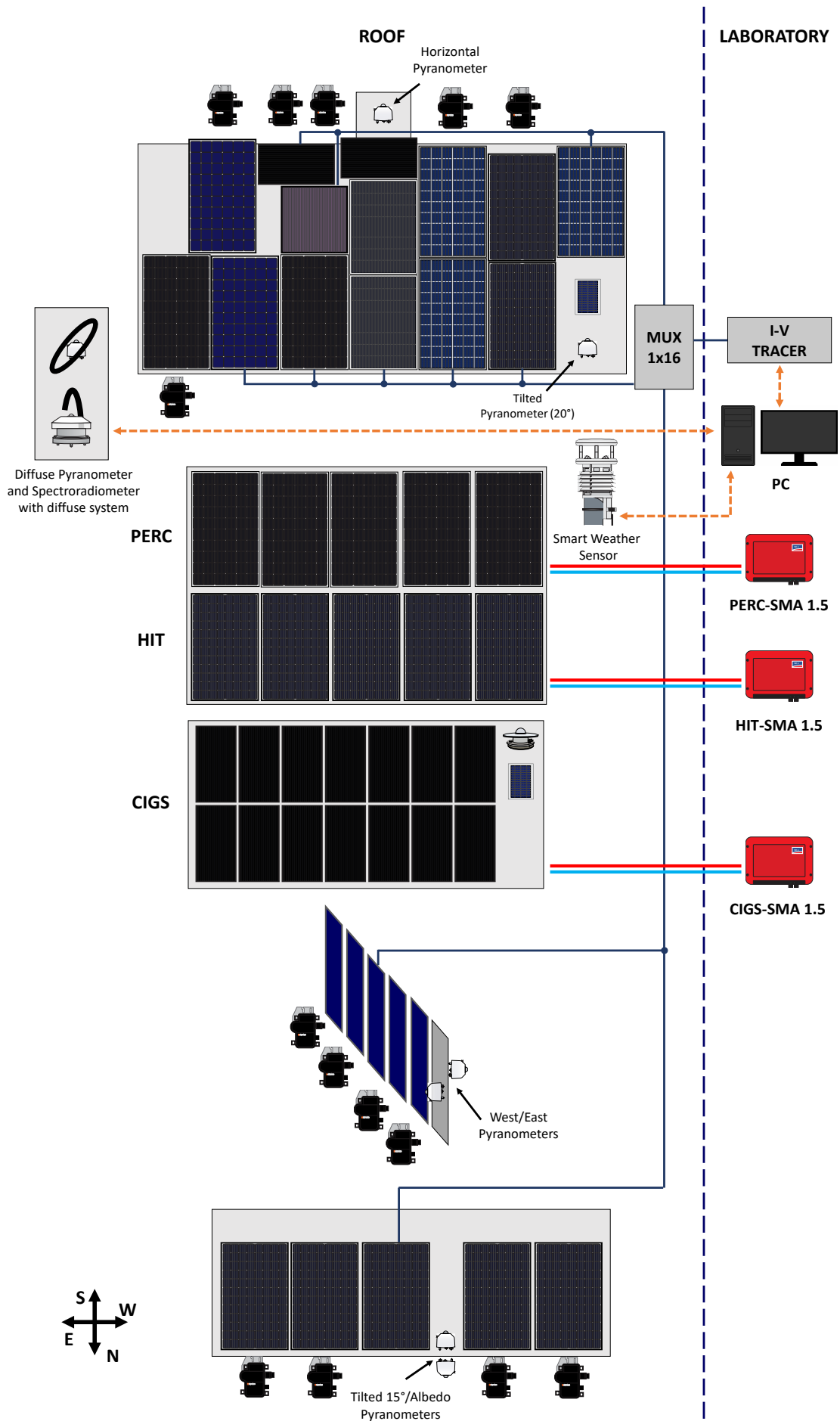


Figure 5.4: Schematic diagram of the current state of the entire Outdoor-PV Laboratory.

Appendix A: Complementary information of the measurement system

This appendix will describe the schematic circuits, components and software development for the measurement system described in Chapter 2 of this Doctoral Thesis.

The main component of the control system is made up of an Arduino Mega 2560, which is a development board based on the ATmega2560 microcontroller and among some of its characteristics has 54 digital inputs/outputs (A1, . . . , A54). The digital outputs control all the components like the multiplexers, relays, optocouplers and the trigger of the multimeters.

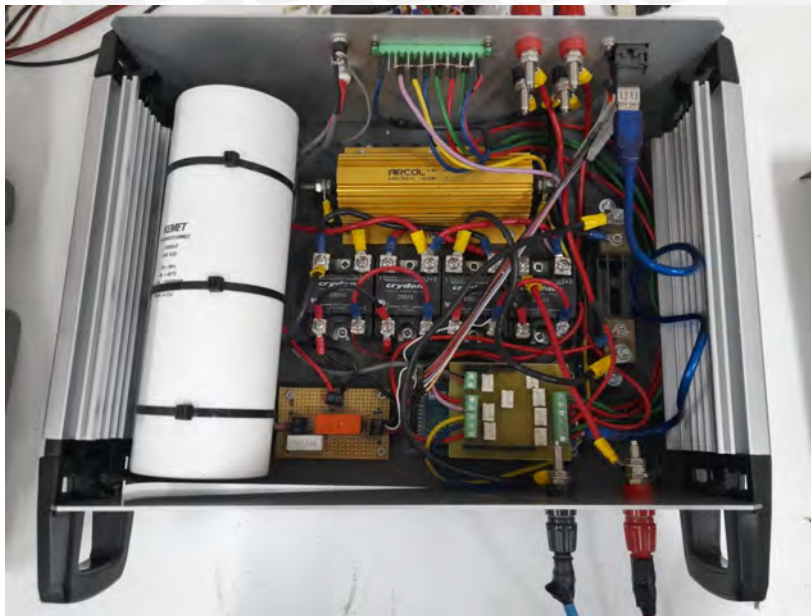


Figure A. 1: Photograph of I-V tracer

I-V Tracer

The following Table details the components used for the I-V tracer and sensor card.

| | Component | Model | Manufacturer |
|----------------------|------------------------|--------------------|-----------------|
| R_1, R_2, R_3, R_4 | Solid State Relay | D5D10 | Crydom |
| R_{sh} | Shunt resistor | YN01-04751BS000000 | Sifam Tinsley |
| R_d | Discharge resistor | HS30025RJ | Arcol |
| P | Relay | RTE24005 | TE Connectivity |
| C | Electrolytic Capacitor | PEH200SX5150MU2 | KEMET |
| V_p | Pre-charge source | 175-3270 | RS PRO |
| M_I, M_V | Multimeter | 34465A | Keysight |

Figure A.2 shows the circuit diagram of the I-V tracer indicating the digital inputs. A49 enable R_1 and R_2 (for the charge phase), A51 enable R_3 and R_4 (discharge phase), and A53 enable P (pre-charge phase).

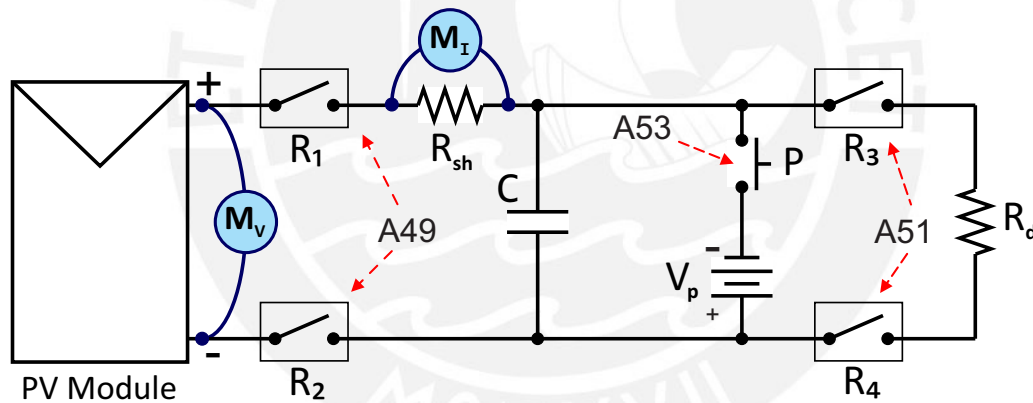


Figure A. 2: Diagram for the I-V curve tracer

The table indicates the number and function of each digital output for each I-V tracer phase.

| Digital Output | Function |
|----------------|------------|
| A49 | Charge |
| A51 | Discharge |
| A53 | Pre-charge |

The following figure shows the PCB for the Sensor card. The relays are activated by the digital output of the Arduino and allow the connection of the irradiance, temperature and current sensors to the Multimeter 2. It is also used as a trigger for the two Multimeters.

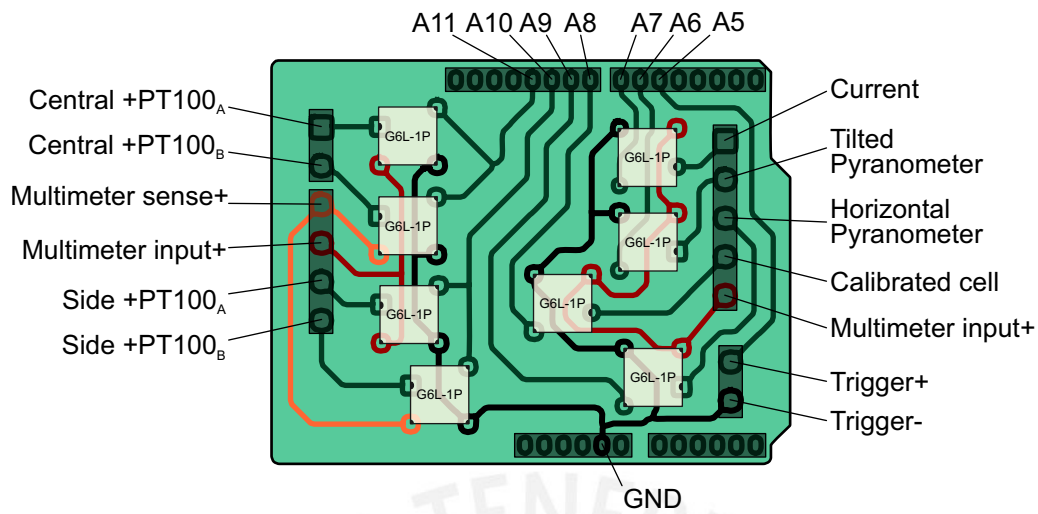


Figure A. 3: PCB for the sensor card.

The table indicates the number and function of each digital output for the Sensor Card.

| Digital Output | Function |
|----------------|------------------------|
| A5 | Trigger+ |
| A6 | Horizontal pyranometer |
| A7 | Current |
| A8 | Tilted pyranometer |
| A9 | Calibrated cell |
| A10 | Side +PT100 |
| A11 | Central +PT100 |

Multiplexer System

The multiplexer system allows the measurement of the I-V curve for multiple PV modules. It mainly consists in Module PV Boxes (Figure A.4) and the Analog Multiplexer (Figure A.6).

The following table details the components used for the Multiplexer system

| | Component | Model | Manufacturer |
|------------|-------------------|----------|------------------|
| D1, D2 | Solid State Relay | D5D10 | Crydom |
| G1, G2, G3 | Relay Optocoupler | G3VM532C | Omron |
| MUX | Multiplexer | DG406DJ+ | Maxim Integrated |

The current flow from the PV modules is connected to relays D_1 and D_2 . The PV module voltage, the center Pt100 and side Pt100 are connected to relays G_1 , G_2 , and G_3 . The PV Module Box is activated by a voltage difference on B_x .

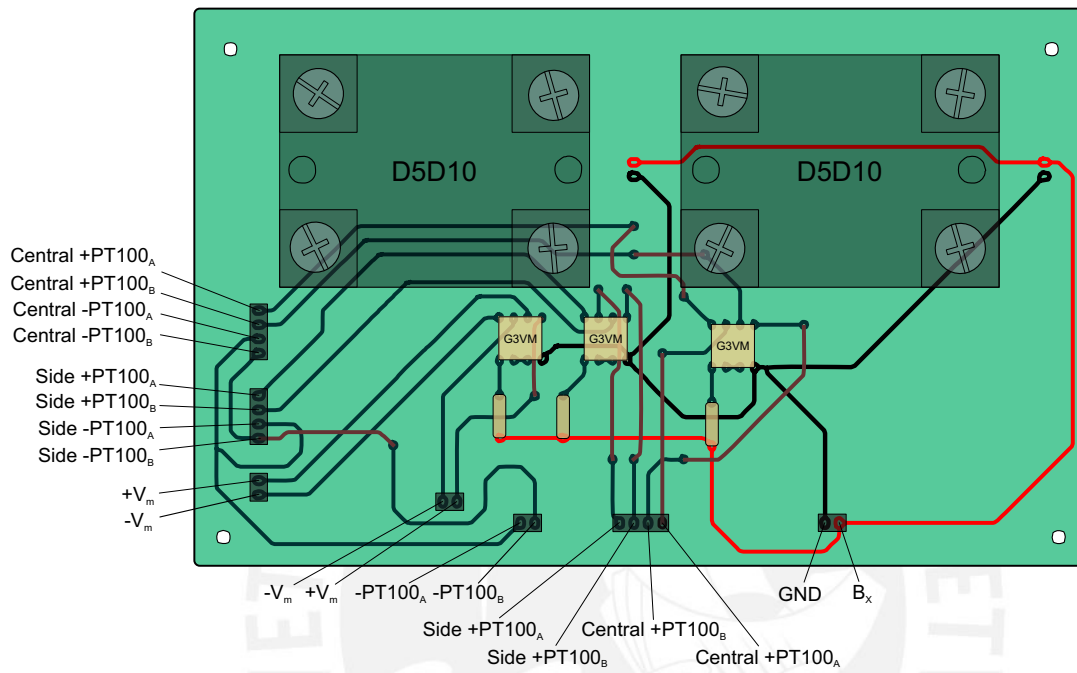


Figure A. 4: PCB for the Box circuit.

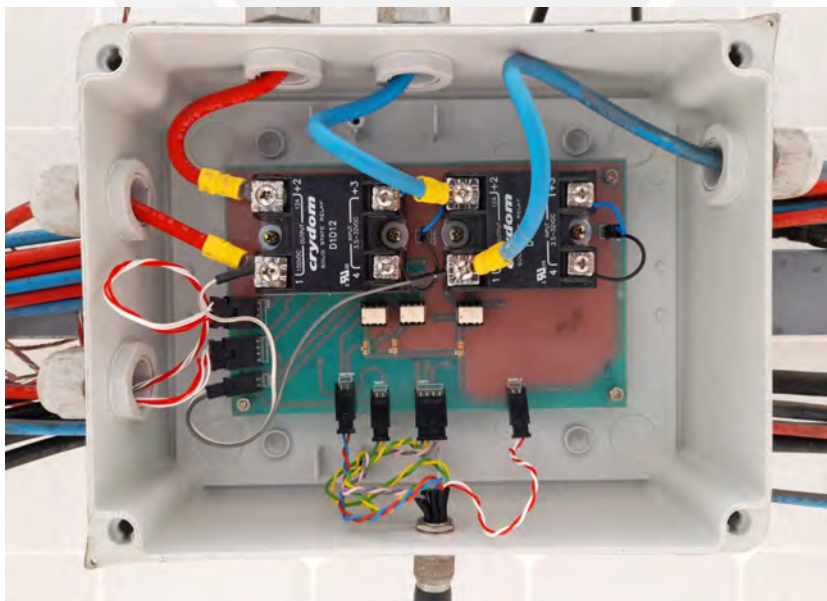


Figure A. 5: Photography of the PV Box circuit.

The Analog Multiplexer DG406 controls 16 output channels (B1, B2, ..., B16) via four input controls (S1, S2, S3, S4). The PV Module boxes are connected to the output channels. The digital outputs of the Arduino were connected to the control inputs. The enable (EN) allows the multiplexer circuit to be turned on or off.

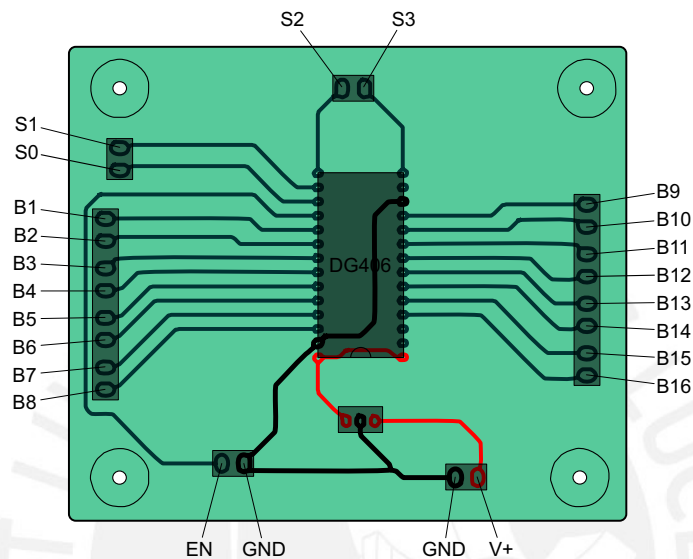


Figure A. 6: PCB for the multiplexer circuit.

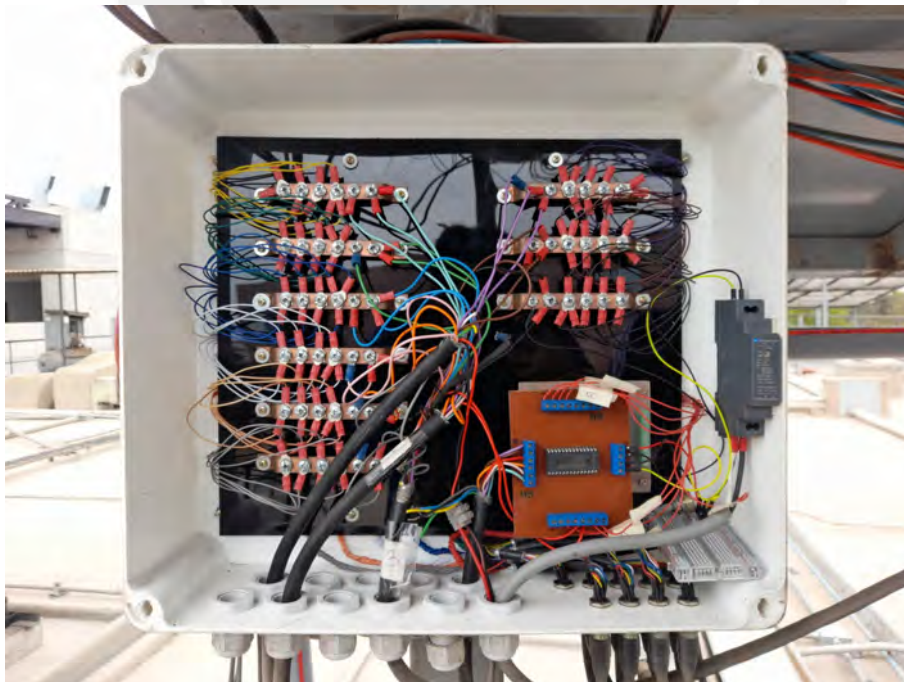


Figure A. 7: Photography of the multiplexer system.

The table indicates the number and function of each digital output for Multiplexer System.

| Digital Output | Function |
|----------------|-------------|
| A44 | EN (Enable) |
| A46 | S3 |
| A48 | S2 |
| A50 | S1 |
| A52 | S0 |

The flowchart in Figure A.9, corresponds to the automated control and storage of the measurement system software.

When the software starts, it checks that the instruments are working correctly and check if the automated station is activated. Then the time filter, that is set between 5:30 and 18:30 hours, is checked. Outside of this range, the weather station will continue to measure environmental parameters.

After the hourly filter, the temperature of the selected PV module and the irradiance are measured. Simultaneously with the irradiance, the solar spectrum and environmental parameters are also measured. The I-V curve is drawn if it is verified that the GTI is greater than 25 W m^{-2} .

The charging time is calculated with the PV module temperature and irradiance data. The charging time is used to configure the measurement speed of the multimeters. In the charging phase, the trigger is activated to measure the I-V curve. In the discharging phase, the irradiance is measured again to ensure no significant variation at the beginning and at the end of the I-V curve tracing. Finally, the data is saved in .CSV files.

The following list details each step of the automated measurement process:

1. **Active Station?:** Constantly is verified.
2. **Time Filter:** Range of hours where the I-V curve is measured.
3. **Select PV:** The characteristic data is loaded from the configuration table (2.19).

4. **Active multiplexer:** The multiplexer is activated depending on the number of PV module to which it is connected according to the configuration table.
5. **Pre-charge:** Pre-charge voltage is activated (5 V - -12V).
6. **Temperature:** Measurement module temperature.
7. **Spectrum:** Measurement spectrum.
8. **Irradiance:** Measurement V_g , GHI, GTI.
9. **Weather:** Measurement weather conditions.
10. **GTI:** If not greater than 25 W m^{-2} , the spectrum measurement is discarded.
11. **GTI:** If not greater than 25 W m^{-2} , the I-V measurement is discarded.
12. **Calculating Charging time:** It is calculated based on the module temperature and irradiance.
13. **Select NPLC:** Number of power-line cycles (NPLC) indicates the accuracy with which a voltage or current is displayed on an instrument. NPLC for the Keysight 34465A at a frequency of 60 Hz is shown in Table 3, according to the manufacturer's data sheet [92]. The calibration of the (NPLC) was made with respect of each PV module's charging time (Table 2).

| NPLC | Integration time | Reading/s |
|----------|-------------------|-----------|
| 1 PLC | 16.7 ms | 60/50 |
| 0.2 PLC | 3 ms | 333 |
| 0.06 PLC | 1 ms | 1000 |
| 0.02 PLC | 300 μs | 3333 |

14. **Configure Multimeters:** SCPI commands provided by the Keysight Multimeter Operation Guide [92].

| Command | Description |
|-----------------------|---|
| CONF:VOLT:DC | Configure DC voltage measurements |
| VOLT:DC:RANG:AUTO OFF | Disable autorange |
| VOLT:DC:RANG ... | Set the range in 1 for multimeter 1 and 1000 for multimeter 2 |
| VOLT:DC:NPLC ... | Set NPLC value depending on table 1 |
| VOLT:DC:ZERO:AUTO OFF | Disable autozero mode |
| SAMP:COUN ... | Set the number of measurements depending on the module |
| TRIG:COUN 1 | Set the trigger count to 1 measurement |
| TRIG:DEL:AUTO OFF | Disable the automatic trigger delay |
| TRIG:DEL 0 | Set the trigger delay in 0 |
| TRIG:SOUR EXT | Set make a measurement using an external trigger |
| TRIG:SLOP POS | Set a positive signal to start the measurements |
| INIT | Set the state to “wait-for-trigger”, for start the measurements |

15. **Wait:** Once everything is ready, preload is deactivated while waiting for the trigger (A5).

16. **Charge:** I-V curve is measured

17. **Discharge:** Discharge the capacitor

18. **Irradiance:** GTI and GHI is measured

19. **Store:** The data storage for each measurement is saved in three files in CSV format. For the I-V data format: Module_Day_Month_Year_Hour_Minute_Second.csv.

| Date | H | V | I | P | λ | E | T _s | T _c | V _g | GHI | GTI | Ta | Hr | Pr | Da | Ws | Wd |
|-------------|----------------|----------------|----------------|----------------|-------------|----------------|----------------|----------------|-----------------|------------------|------------------|-----------------|-----------------|-----------------|-----------------|-----------------|-----------------|
| D/M/Y | H ₁ | V ₁ | I ₁ | P ₁ | λ_1 | E ₁ | T ₁ | T ₂ | V _{g1} | GHI ₁ | GTI ₁ | Ta ₁ | Hr ₁ | Pr ₁ | Da ₁ | Ws ₁ | Wd ₁ |
| Module | H ₂ | V ₂ | I ₂ | P ₂ | λ_2 | E ₂ | | | V _{g2} | GHI ₂ | GTI ₂ | | | | | | |
| # Points | E _t | ∴ | ∴ | ∴ | ∴ | ∴ | | | | | | | | | | | |
| Charge time | | ∴ | ∴ | ∴ | ∴ | ∴ | | | | | | | | | | | |
| NPLC | | ∴ | ∴ | ∴ | ∴ | ∴ | | | | | | | | | | | |
| | | ∴ | ∴ | ∴ | ∴ | ∴ | | | | | | | | | | | |
| | | V _p | I _p | P _p | λ_n | E _n | | | | | | | | | | | |

Weather data format: WS500_Day_Month_Year.csv

| Date | Hour | Ta | Hr | Pr | Da | Ws | Wd |
|-------|----------------|-----------------|-----------------|-----------------|-----------------|-----------------|-----------------|
| D/M/Y | H ₁ | Ta ₁ | Hr ₁ | Pr ₁ | Da ₁ | Ws ₁ | Wd ₁ |
| | ∴ | ∴ | ∴ | ∴ | ∴ | ∴ | ∴ |

Spectrum data format: MS-711_Day_Month_Year.csv

| Date | Hour 1 | G ₁ | | Hour 2 | G ₂ | | # | Tc | λ ₁ | λ ₂ | ... | λ ₂₀₄₈ |
|-------|----------------|------------------|------------------|----------------|------------------|------------------|---|------|----------------|----------------|-----|-------------------|
| D/M/Y | H ₁ | GHI ₁ | GTI ₁ | H ₂ | GHI ₂ | GTI ₂ | 1 | tttt | E ₁ | E ₂ | ... | E ₂₀₄₈ |
| | ⋮ | ⋮ | ⋮ | ⋮ | ⋮ | ⋮ | ⋮ | ⋮ | ⋮ | ⋮ | ⋮ | ⋮ |

The timing diagram in figure A.8 is for the measurement of an I-V curve. Each color corresponds to the same process in the flowchart.

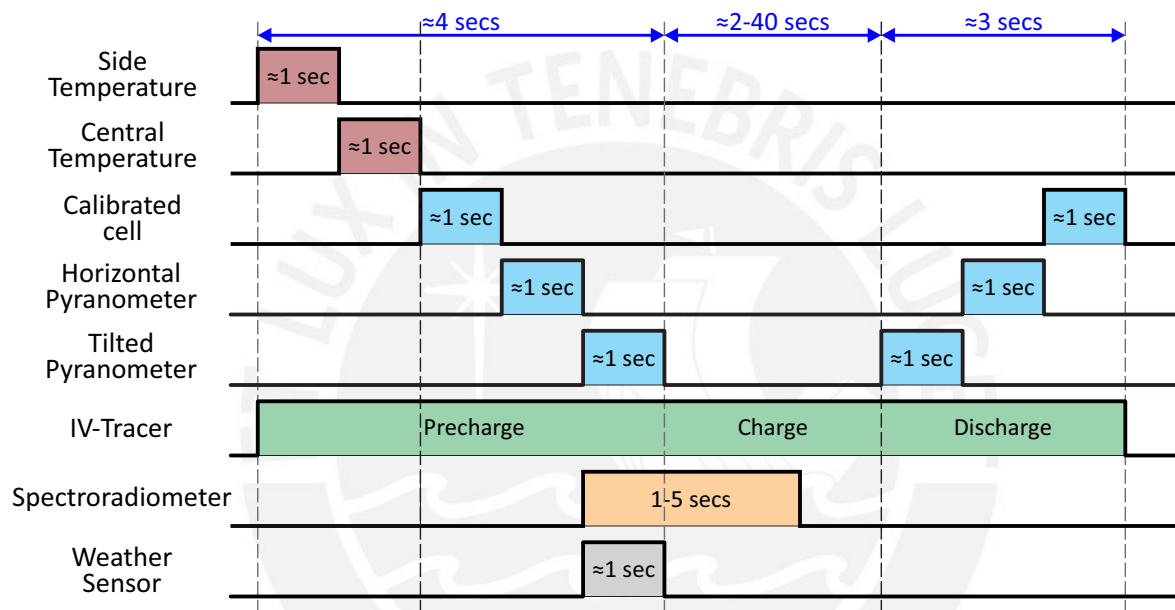


Figure A. 8: Timing diagram for I-V tracing and environmental measurements.

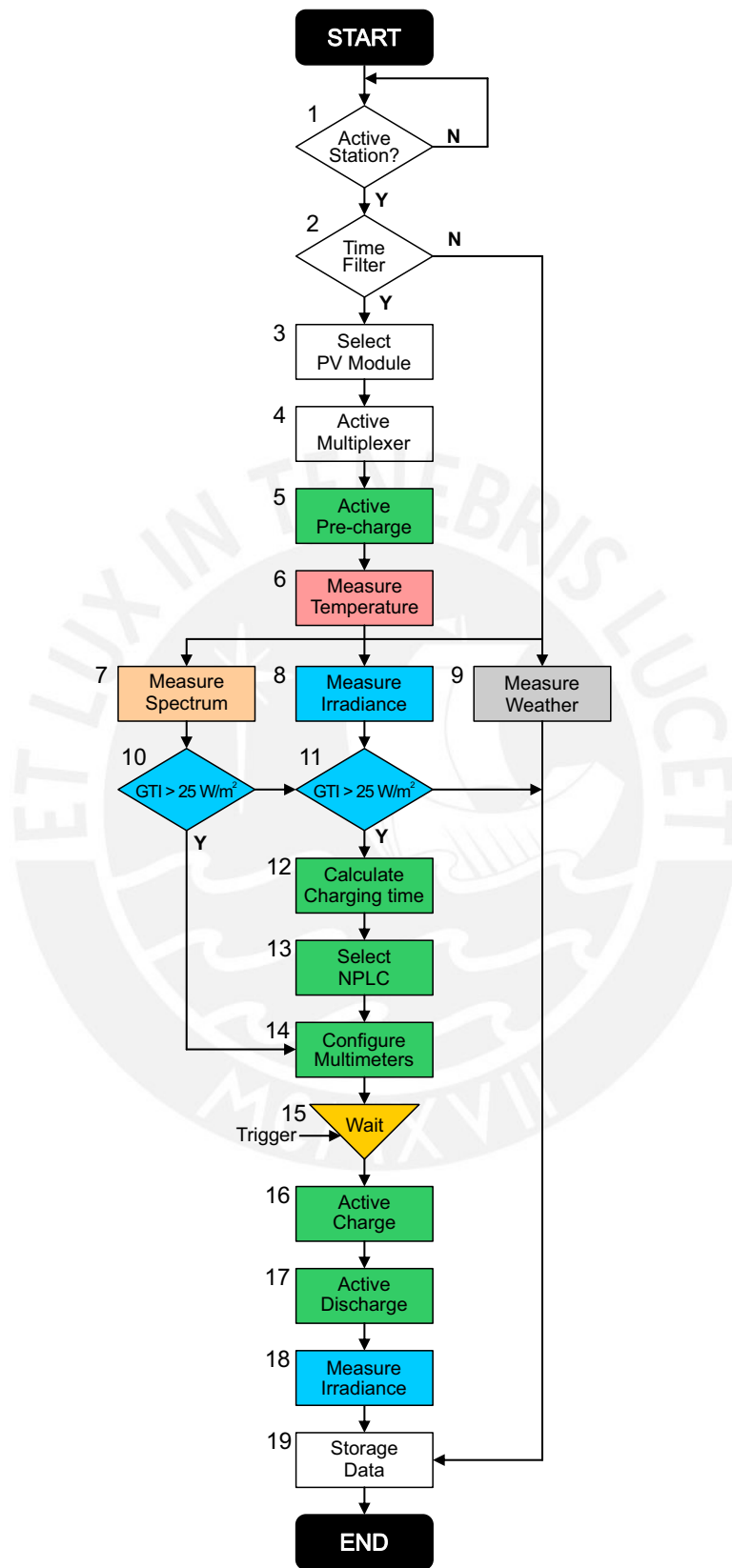


Figure A. 9: Flowchart of the automated software for the measurement and storage of I-V curves, solar spectrum and environmental parameters.

Appendix B: Gaussian fit for Spectral Response

This appendix describes the Gaussian fit that was described in section 4.2.3 and necessary for the results of chapter 4 in this doctoral thesis. The objective of this fit was to obtain a continuous function of the Spectral Responses in the following figure.

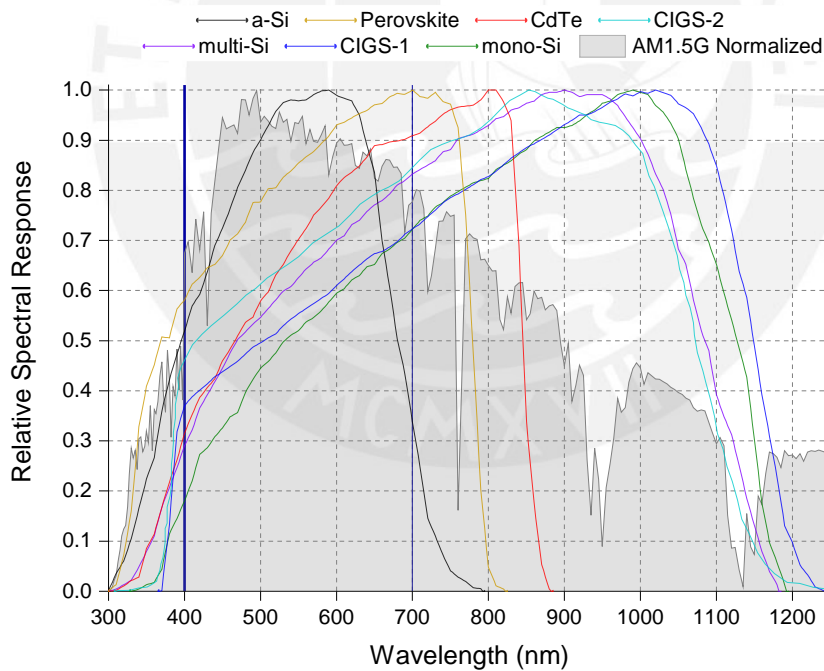


Figure B. 1: Spectral responses for seven PV technologies.

The Gaussian function of a peak,

$$p_n = y_0 + \frac{A}{w \cdot \sqrt{\frac{\pi}{2}}} e^{-2\left(\frac{x-x_c}{w}\right)^2} \quad (5.1)$$

The total fit is obtained by adding the peaks considered for each case. The number of peaks and values of the variables are shown in the tables.

Amorphous Silicon:

| | p_n | y_0 | x_c | w | A |
|------|--------|----------|-----------|-----------|-----------|
| a-Si | Peak 1 | -0.00335 | 322.29108 | 82.27475 | -15.12008 |
| | Peak 2 | -0.00335 | 393.25424 | 128.34538 | 62.08497 |
| | Peak 3 | -0.00335 | 530.08637 | 141.86485 | 156.34918 |
| | Peak 4 | -0.00335 | 637.90063 | 96.76148 | 75.63853 |

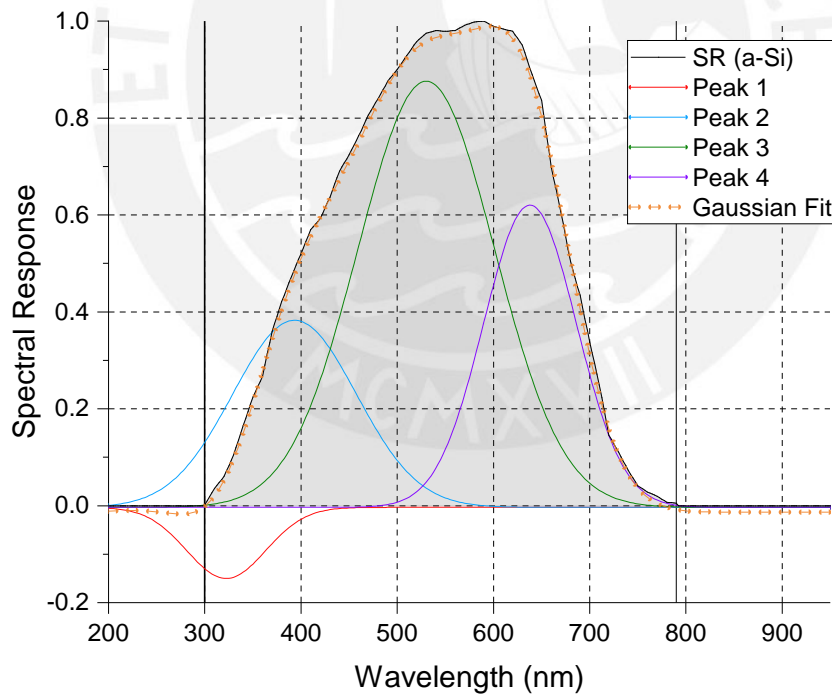


Figure B. 2: Gaussian Fit for a-Si SR.

Perovskite:

| | p_n | y_0 | x_c | w | A |
|------|--------|----------|-----------|-----------|-----------|
| a-Si | Peak 1 | -0.11779 | 367.03839 | 44.03272 | 40.84174 |
| | Peak 2 | -0.11779 | 370.45168 | 37.44048 | -25.20127 |
| | Peak 3 | -0.11779 | 412.73126 | 94.1745 | 55.83548 |
| | Peak 4 | -0.11779 | 511.69153 | 522.61203 | 54.89659 |
| | Peak 5 | -0.11779 | 511.69153 | 110.17439 | 93.30784 |
| | Peak 6 | -0.11779 | 622.09161 | 110.05367 | 112.8652 |
| | Peak 7 | -0.11779 | 712.59171 | 85.49106 | 81.5442 |
| | Peak 8 | -0.11779 | 750.10189 | 30.61282 | -32.63108 |
| | Peak 9 | -0.11779 | 755.94255 | 36.07943 | 59.78127 |

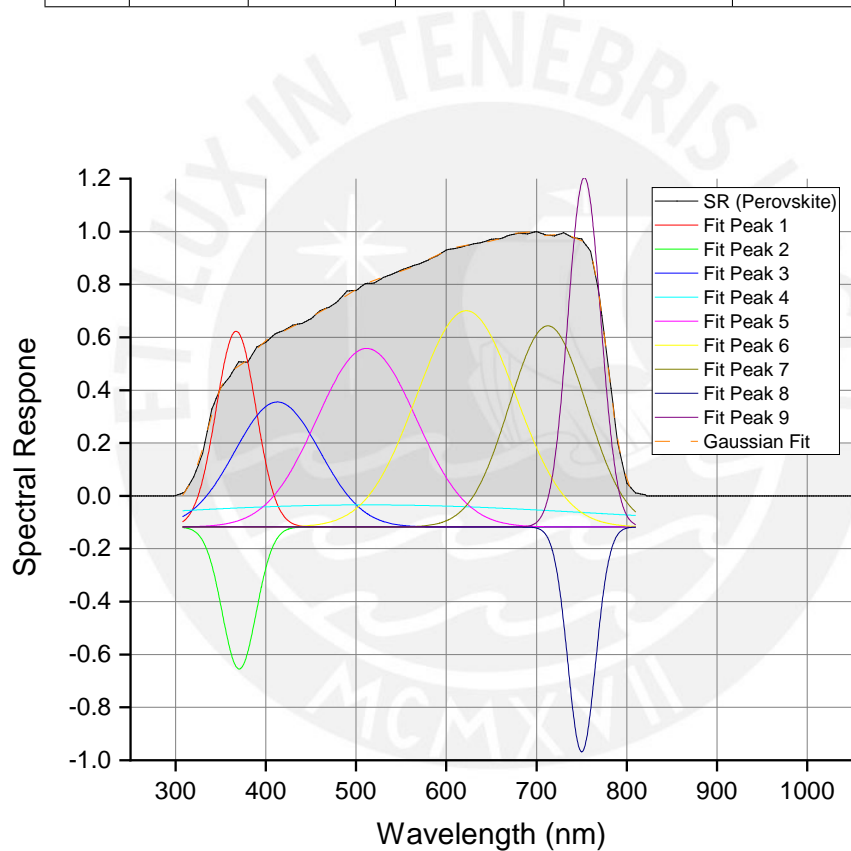


Figure B. 3: Gaussian Fit for Perovskite SR.

Cadmium Telluride:

| | p_n | y_0 | x_c | w | A |
|------|--------|----------|-----------|-----------|-----------|
| CdTe | Peak 1 | -0.54973 | 343.31056 | 58.22792 | -8.16636 |
| | Peak 2 | -0.54973 | 530.92672 | 425.36999 | 557.86793 |
| | Peak 3 | -0.54973 | 724.17726 | 227.36158 | 188.67842 |
| | Peak 4 | -0.54973 | 780.61322 | 80.6681 | 33.89733 |
| | Peak 5 | -0.54973 | 815.17233 | 39.08886 | 16.63886 |
| | Peak 6 | -0.54973 | 833.26457 | 20.4886 | 6.50625 |

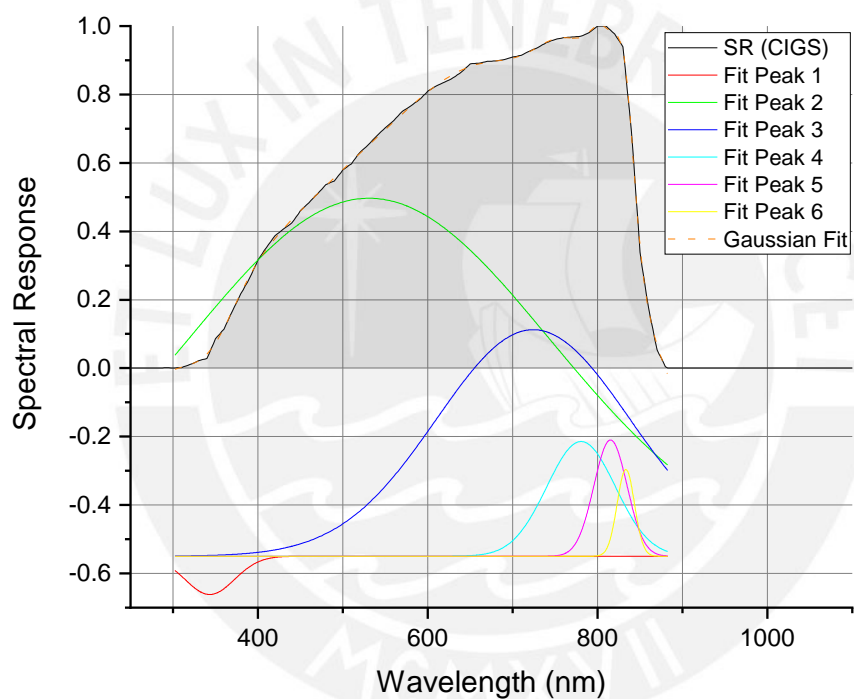


Figure B. 4: Gaussian Fit for CdTe SR.

CIGS-2:

| | p_n | y_0 | x_c | w | A |
|--------|---------|---------|------------|------------|------------|
| CIGS-2 | Peak 1 | 0.08562 | 342.81825 | 1429.17662 | -77.62555 |
| | Peak 2 | 0.08562 | 92.55775 | 1326.47143 | -68.90402 |
| | Peak 3 | 0.08562 | 39255775 | 18.63649 | 3.77032 |
| | Peak 4 | 0.08562 | 409.95629 | 39.54338 | 12.72585 |
| | Peak 5 | 0.08562 | 446.91442 | 62.38021 | 21.27623 |
| | Peak 6 | 0.08562 | 506.2004 | 98.70581 | 49.51263 |
| | Peak 7 | 0.08562 | 622.29114 | 141.20854 | 119.34006 |
| | Peak 8 | 0.08562 | 733.53588 | 108.07192 | 65.33525 |
| | Peak 9 | 0.08562 | 849.36146 | 136.94168 | 149.64532 |
| | Peak 10 | 0.08562 | 969.21816 | 115.72464 | 83.9293 |
| | Peak 11 | 0.08562 | 1049.03172 | 113.53287 | 59.58332 |
| | Peak 12 | 0.08562 | 1913.70748 | 1144.27614 | -132.48526 |

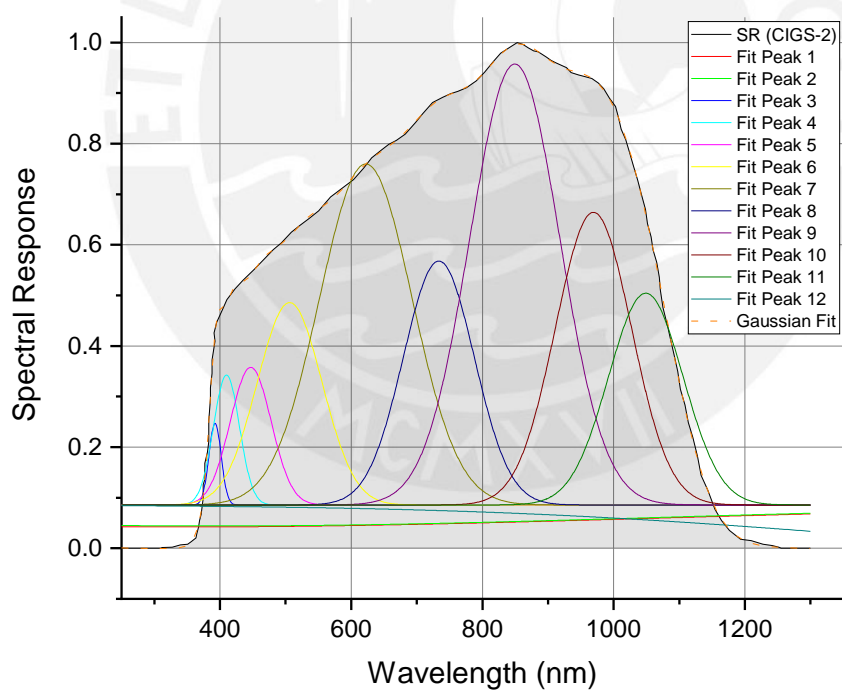


Figure B. 5: Gaussian Fit for CIGS-2 SR.

Multi-crystalline Silicon:

| | p_n | y_0 | x_c | w | A |
|----------|--------|----------|-----------|-----------|-------------|
| multi-Si | Peak 1 | -0.19604 | 446.82609 | 111.79138 | 18.0132 |
| | Peak 2 | -0.19604 | 653.4049 | 385.16609 | 439.85628 |
| | Peak 3 | -0.19604 | 933.91353 | 208.48011 | -2750.69918 |
| | Peak 4 | -0.19604 | 936.01141 | 213.409 | 3050.61874 |

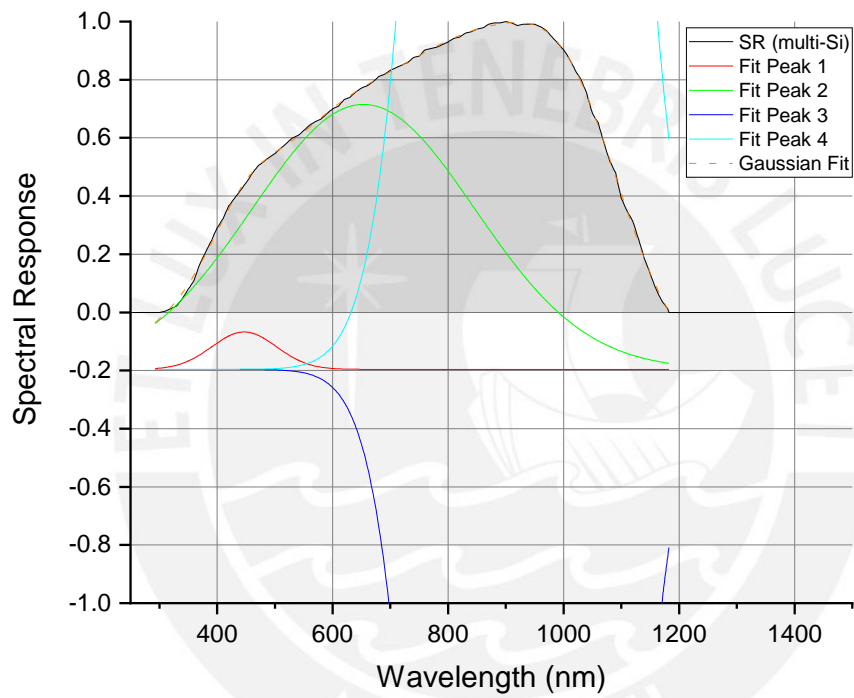


Figure B. 6: Gaussian Fit for multi-Si SR.

CIGS-1:

| | p_n | y_0 | x_c | w | A |
|----------|--------|----------|-----------|-----------|-------------|
| multi-Si | Peak 1 | -0.19604 | 446.82609 | 111.79138 | 18.0132 |
| | Peak 2 | -0.19604 | 653.4049 | 385.16609 | 439.85628 |
| | Peak 3 | -0.19604 | 933.91353 | 208.48011 | -2750.69918 |
| | Peak 4 | -0.19604 | 936.01141 | 213.409 | 3050.61874 |

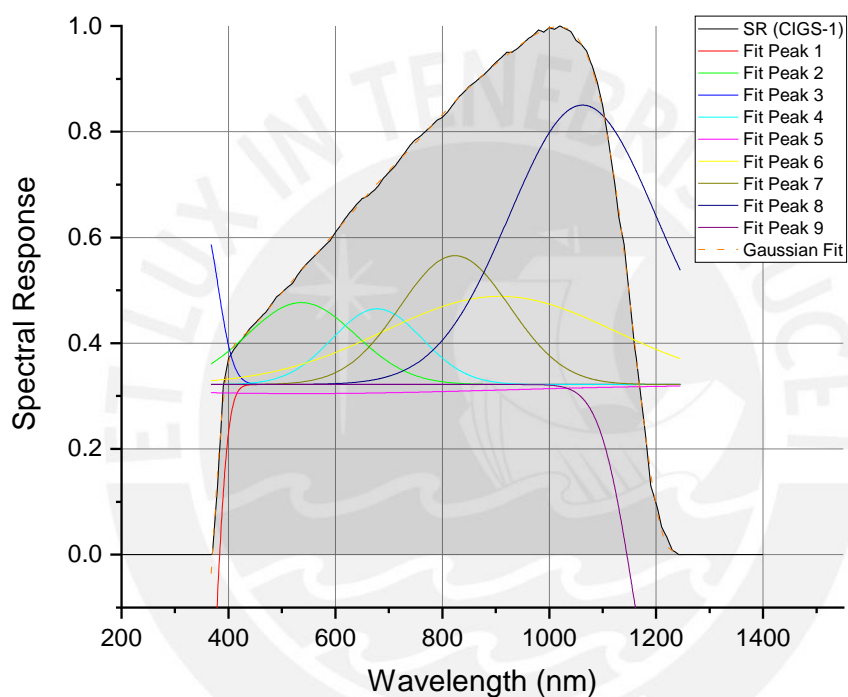


Figure B. 7: Gaussian Fit for CIGS-1 SR.

Mono-crystalline Silicon:

| | p_n | y_0 | x_c | w | A |
|---------|--------|----------|------------|-----------|------------|
| mono-Si | Peak 1 | -2.40303 | 352.54728 | 382.12385 | 519.88379 |
| | Peak 2 | -2.40303 | 858.55456 | 758.33375 | 3027.20614 |
| | Peak 3 | -2.40303 | 1059.28205 | 205.11326 | 126.30857 |

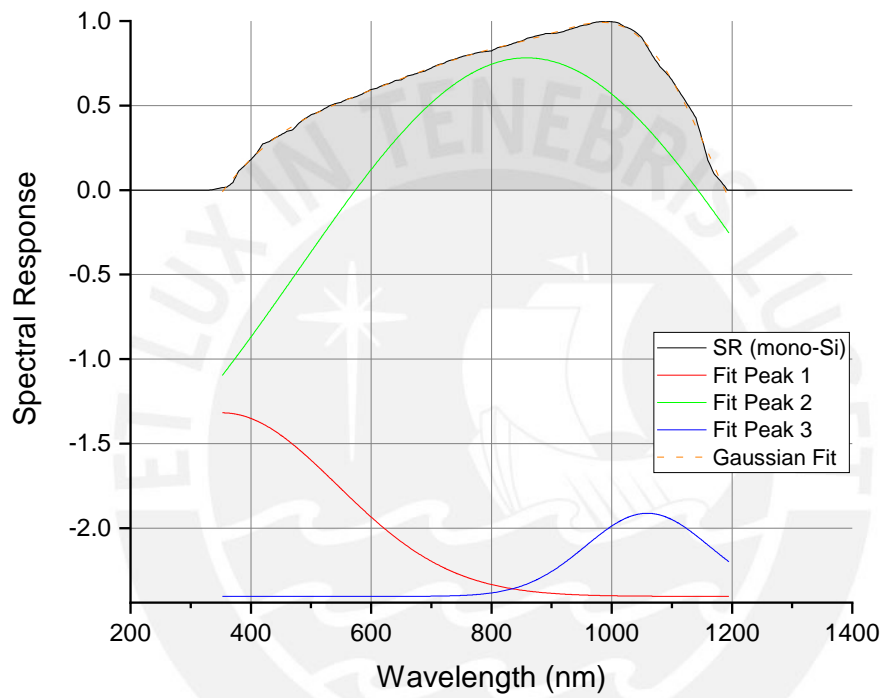


Figure B. 8: Gaussian Fit for mono-Si SR

Bibliography

- [1] THE BANK GROUP, “Peru Overview: Development news, research, data | World Bank,” 2021.
- [2] M. A. Zambrano-Monserrate, C. A. Silva-Zambrano, J. L. Davalos-Penafiel, A. Zambrano-Monserrate, and M. A. Ruano, “Testing environmental Kuznets curve hypothesis in Peru: The role of renewable electricity, petroleum and dry natural gas,” *Renewable and Sustainable Energy Reviews*, vol. 82, pp. 4170–4178, feb 2018.
- [3] M. López, M. Veigas, and G. Iglesias, “On the wave energy resource of Peru,” *Energy Conversion and Management*, vol. 90, pp. 34–40, 2015.
- [4] THE BANK GROUP, “Total greenhouse gas emissions (kt of CO2 equivalent) - Peru | Data,” 2020.
- [5] B. Schmerler, Daniel; Velarde, José Carlos; Rodríguez, Abel y Solís, ed., *Energías Renovables: Experiencia y Perspectivas en la Ruta del Perú Hacia la Transición Energética*. Osinergmin, 2019.
- [6] Enel, “Hoja de Ruta de Transición Energética - enel.pe,” 2021.
- [7] “Ministerio de Energía y Minas - Instalan más de 80 mil paneles solares en zonas rurales del Perú,” 2018.
- [8] “MEM y la Alianza Solar Internacional suscribieron convenio de cooperación para el impulso de Energías Renovables en Perú | Sun World 2019,” 2018.

- [9] D. Macera, “Enel inaugura la planta solar más grande del Perú | Economía | Perú | El Comercio Perú,” 2018.
- [10] L. M. y. D. M. Anabel Castro, Cristina Davila, Wil Laura, Félix Cubas, Grinia Avalos, Carlos López Ocana, Donna Villena, Marcia Valdez, Julio Urbiola, Irene Trebejo, “CLIMAS DEL PERÚ-Mapa de Clasificación Climática Nacional,” *Servicio Nacional de Meteorología e Hidrología del Perú*, 2021.
- [11] R. Espinoza, E. Muñoz-Cerón, J. Aguilera, and J. de la Casa, “Feasibility evaluation of residential photovoltaic self-consumption projects in Peru,” *Renewable Energy*, vol. 136, pp. 414–427, 2019.
- [12] R. E. Espinoza, E. Muñoz-Cerón, E. R. Ramos, and J. de la Casa, “Characterization in power and energy of two photovoltaic grid connected systems of different technologies (crystal silicon and thin film), operating in Lima,” *Journal of Physics: Conference Series*, vol. 1173, p. 012011, feb 2019.
- [13] I. Romero-Fiances, E. Muñoz-Cerón, R. Espinoza-Paredes, G. Nofuentes, J. De La Casa, R. Espinoza, E. Muñoz-Cerón, J. Aguilera, J. De La Casa, I. Romero-Fiances, E. Muñoz-Cerón, R. Espinoza-Paredes, G. Nofuentes, and J. De La Casa, “Analysis of the performance of various pv module technologies in Peru,” *Energies*, vol. 12, no. 1, p. 186, 2019.
- [14] “Universidad Nacional de Ingeniería - Emergiendo con el sol,” 2015.
- [15] M. Kottke, J. Grieser, C. Beck, B. Rudolf, and F. Rubel, “World Map of the Köppen-Geiger climate classification updated,” *Meteorologische Zeitschrift*, vol. 15, pp. 259–263, jul 2006.
- [16] M. Schweiger, W. Herrmann, C. Monokroussos, and U. Rau, “Understanding the energy yield of PV modules,” *Www.Pv-Tech.Org*, no. May, 2017.

- [17] I. E. C. Standard, “60891. Photovoltaic Devices. Procedures for Temperature and Irradiance Corrections to Measured IV Characteristics,” *International Electrotechnical Commission*, 2009.
- [18] O. O. Ogbomo, E. H. Amalu, N. N. Ekere, and P. O. Olagbegi, “A review of photovoltaic module technologies for increased performance in tropical climate,” *Renewable and Sustainable Energy Reviews*, vol. 75, pp. 1225–1238, aug 2017.
- [19] C. R. Osterwald, “Standards, Calibration and Testing of PV Modules and Solar Cells,” *Practical Handbook of Photovoltaics: Fundamentals and Applications*, pp. 793–816, 2003.
- [20] M. Schweiger, W. Herrmann, A. Gerber, and U. Rau, “Understanding the energy yield of photovoltaic modules in different climates by linear performance loss analysis of the module performance ratio,” *IET Renewable Power Generation*, vol. 11, pp. 558–565, apr 2017.
- [21] M. Schweiger and W. Herrmann, “Comparison of energy yield data of fifteen PV module technologies operating in four different climates,” in *2015 IEEE 42nd Photovoltaic Specialist Conference, PVSC 2015*, Institute of Electrical and Electronics Engineers Inc., dec 2015.
- [22] E. Duran, M. Piliouline, M. Sidrach-de Cardona, Gala, X, J. N, and J. M. Andujar, “Different methods to obtain the I-V curve of PV modules: A review,” *Photovoltaic Specialists Conference, 2008. PVSC '08. 33rd IEEE*, pp. 1–6, 2008.
- [23] M. Jankovec, “LPVO: PV module monitoring.”
- [24] J. Montes-Romero, M. Piliouline, J. V. Muñoz, E. F. Fernández, and J. De La Casa, “Photovoltaic device performance evaluation using an open-hardware system and standard calibrated laboratory instruments,” *Energies*, vol. 10, no. 11, 2017.

- [25] P. Hernday, "Field applications for IV curve tracers," tech. rep., Solarpro, 2011.
- [26] "Best Research-Cell Efficiency Chart | Photovoltaic Research | NREL."
- [27] I. E. Commission, "Photovoltaic system performance monitoring-guidelines for measurement, data exchange and analysis," *IEC 61724*, 1998.
- [28] B. Marion, J. Adelstein, K. Boyle, H. Hayden, B. Hammond, Fletcher, B. Canada, D. Narang, A. Kimber, L. Mitchell, G. Rich, and T. Townsend, "Performance parameters for grid-connected PV systems," in *Conference Record of the IEEE Photovoltaic Specialists Conference*, pp. 1601–1606, 2005.
- [29] M. Theristis, V. Venizelou, G. Makrides, and G. E. Georghiou, "Energy yield in photovoltaic systems," in *McEvoy's Handbook of Photovoltaics: Fundamentals and Applications*, pp. 671–713, Elsevier Inc., jan 2018.
- [30] L. A. Conde, J. Montes Romero, A. M. Carhuavilca Vela, R. A. Perich Ibañez, J. A. Guerra Torres, M. A. Sevillano Bendezú, B. X. Calsi Silva, J. R. Angulo Abanto, J. De la Casa Higuera, and J. A. Palomino Töfflinger, "Puesta en marcha de un laboratorio para la caracterización de tecnologías fotovoltaicas a sol real bajo las condiciones climáticas de Lima," *Tecnia*, vol. 30, pp. 80–89, may 2020.
- [31] L. A. Conde, J. Montes-Romero, A. Carhuavilca, R. Perich, A. Jorge, J. Angulo, E. Muñoz, J. A. Töfflinger, and J. D. Casa, "Performance evaluation and characterization of different photovoltaic technologies under the coastal , desertic climate conditions of Lima , Peru," *Solar World Congress*, 2019.
- [32] B. X. Calsi, L. A. Conde, J. R. Angulo, J. Montes-Romero, J. A. Guerra, J. de la Casa, and J. A. Töfflinger, "Monitoring versus prediction of the power of three different PV technologies in the coast of Lima-Peru," *Journal of Physics: Conference Series*, vol. 1841, p. 012001, mar 2021.

- [33] L. A. Conde, J. R. Angulo, M. Sevillano-Bendezú, G. Nofuentes, J. A. Töfflinger, and J. de la Casa, “Spectral effects on the energy yield of various photovoltaic technologies in Lima (Peru),” *Energy*, vol. 223, p. 120034, may 2021.
- [34] M. Piliouguine, J. Carretero, L. Mora-López, and M. Sidrach-de Cardona, “Experimental system for current-voltage curve measurement of photovoltaic modules under outdoor conditions,” *Progress in Photovoltaics: Research and Applications*, vol. 19, pp. 591–602, aug 2011.
- [35] E. F. Fernandez, J. Montes-Romero, J. De La Casa, A. Firman, M. Caceres, and L. H. Vera, “Contributions to the design and construction of characteristic curve tracers for photovoltaic devices,” in *Proceedings of 2018 Technologies Applied to Electronics Teaching, TAAE 2018*, Institute of Electrical and Electronics Engineers Inc., sep 2018.
- [36] J. Muñoz and E. Lorenzo, “Capacitive load based on IGBTs for on-site characterization of PV arrays,” *Solar Energy*, vol. 80, no. 11, pp. 1489–1497, 2006.
- [37] E. Lorenzo, *Ingeniería Fotovoltaica Vol III*. 2014.
- [38] T. Foken, *Springer Handbook of Atmospheric Measurements*. Springer, 2021.
- [39] F. Vignola, J. Michalsky, and T. Stoffel, *Solar and infrared radiation measurements*. CRC press, 2019.
- [40] J. Polo, W. Fernandez-Neira, and M. Alonso-García, “On the use of reference modules as irradiance sensor for monitoring and modelling rooftop PV systems,” *Renewable Energy*, vol. 106, pp. 186–191, jun 2017.
- [41] Lufft, ed., *User Manual Smart Weather Sensors WS510-UMB WS500-UMB WS301-UMB WS310-UMB WS300-UMB WS200-UMB WS100-UMB*. Lufft, 2018.
- [42] T. Bress, *Effective LabVIEW Programming*. Nts Press, 2013.

- [43] J. M. Carrillo, F. Martínez-Moreno, C. Lorenzo, and E. Lorenzo, “Uncertainties on the outdoor characterization of PV modules and the calibration of reference modules,” *Solar Energy*, vol. 155, pp. 880–892, oct 2017.
- [44] G. Nofuentes, J. Aguilera, R. L. Santiago, J. De La Casa, and L. Hontoria, “A reference-module-based procedure for outdoor estimation of crystalline silicon PV module peak power,” *Progress in Photovoltaics: Research and Applications*, vol. 14, no. 1, pp. 77–87, 2006.
- [45] C. R. Osterwald, “Translation of device performance measurements to reference conditions,” *Solar Cells*, vol. 18, no. 3-4, pp. 269–279, 1986.
- [46] M. Fuentes, G. Nofuentes, J. Aguilera, D. L. Talavera, and M. Castro, “Application and validation of algebraic methods to predict the behaviour of crystalline silicon PV modules in Mediterranean climates,” *Solar Energy*, vol. 81, no. 11, pp. 1396–1408, 2007.
- [47] A. Wheeler, M. Leveille, I. Anton, M. Limpinsel, and S. Kurtz, “Outdoor Performance of PV Technologies in Simulated Automotive Environments,” *Conference Record of the IEEE Photovoltaic Specialists Conference*, pp. 3103–3110, jun 2019.
- [48] M. Torres-Ramírez, G. Nofuentes, J. P. Silva, S. Silvestre, and J. V. Muñoz, “Study on analytical modelling approaches to the performance of thin film PV modules in sunny inland climates,” *Energy*, vol. 73, pp. 731–740, 2014.
- [49] J. Löffler, A. Gordijn, R. L. Stolk, H. Li, J. K. Rath, and R. E. Schropp, “Amorphous and ‘micromorph’ silicon tandem cells with high open-circuit voltage,” *Solar Energy Materials and Solar Cells*, vol. 87, pp. 251–259, may 2005.
- [50] A. Virtuani and L. Fanni, “Seasonal power fluctuations of amorphous silicon thin-film solar modules: distinguishing between different contributions,” *Progress in Photovoltaics: Research and Applications*, vol. 22, pp. 208–217, feb 2014.

- [51] M. G. Deceglie, T. J. Silverman, B. Marion, and S. R. Kurtz, “Metastable changes to the temperature coefficients of thin-film photovoltaic modules,” *2014 IEEE 40th Photovoltaic Specialist Conference, PVSC 2014*, pp. 337–340, oct 2014.
- [52] G. Nofuentes, B. García-Domingo, J. V. Muñoz, and F. Chenlo, “Analysis of the dependence of the spectral factor of some PV technologies on the solar spectrum distribution,” *Applied Energy*, vol. 113, pp. 302–309, 2014.
- [53] T. Ishii, K. Otani, T. Takashima, and Y. Xue, “Solar spectral influence on the performance of photovoltaic (PV) modules under fine weather and cloudy weather conditions,” *Progress in Photovoltaics: Research and Applications*, vol. 21, pp. n/a–n/a, nov 2011.
- [54] P. M. Rodrigo, E. F. Fernández, F. M. Almonacid, and P. J. Pérez-Higueras, “Quantification of the spectral coupling of atmosphere and photovoltaic system performance: Indexes, methods and impact on energy harvesting,” *Solar Energy Materials and Solar Cells*, vol. 163, pp. 73–90, apr 2017.
- [55] C. A. Gueymard, “Simple Model of the Atmospheric Radiative Transfer of Sunshine, version 2 (SMARTS2): Algorithms description and performance assessment,” *Florida Solar Energy Center*, 1995.
- [56] D. Dirnberger, B. Müller, and C. Reise, “On the uncertainty of energetic impact on the yield of different PV technologies due to varying spectral irradiance,” *Solar Energy*, vol. 111, pp. 82–96, jan 2015.
- [57] J. J. Pérez-López, F. Fabero, and F. Chenlo, “Experimental solar spectral irradiance until 2500nm: results and influence on the PV conversion of different materials,” *Progress in Photovoltaics: Research and Applications*, vol. 15, pp. 303–315, jun 2007.
- [58] C. Cornaro and A. Andreotti, “Influence of Average Photon Energy index on solar irradiance characteristics and outdoor performance of photovoltaic modules,” *Progress in Photovoltaics: Research and Applications*, vol. 21, pp. n/a–n/a, apr 2012.

- [59] J. Chantana, S. Ueno, Y. Ota, K. Nishioka, and T. Minemoto, “Uniqueness verification of direct solar spectral index for estimating outdoor performance of concentrator photovoltaic systems,” *Renewable Energy*, vol. 75, pp. 762–766, mar 2015.
- [60] J. Y. Ye, T. Reindl, A. G. Aberle, and T. M. Walsh, “Effect of solar spectrum on the performance of various thin-film PV module technologies in tropical Singapore,” *IEEE Journal of Photovoltaics*, vol. 4, no. 5, pp. 1268–1274, 2014.
- [61] C. Sirisamphanwong and N. Ketjoy, “Impact of spectral irradiance distribution on the outdoor performance of photovoltaic system under Thai climatic conditions,” *Renewable Energy*, vol. 38, pp. 69–74, feb 2012.
- [62] M. Braga, L. R. do Nascimento, and R. R  ther, “Spectral modeling and spectral impacts on the performance of mc-Si and new generation CdTe photovoltaics in warm and sunny climates,” *Solar Energy*, vol. 188, pp. 976–988, aug 2019.
- [63] G. Marques, W. Vilela, E. Pereira, M. Yamasoe, and G. Nofuentes, “Spectral impact on PV in low-latitude sites: the case of southeastern Brazil,” *Renewable Energy*, 2020.
- [64] G. S. Kinsey, N. C. Riedel-Lyngsk  r, A. A. Miguel, M. Boyd, M. Braga, C. Shou, R. R. Cordero, B. C. Duck, C. J. Fell, S. Feron, G. E. Georghiou, N. Habryl, J. J. John, N. Ketjoy, G. L  pez, A. Louwen, E. L. Maweza, T. Minemoto, A. Mittal, C. Molto, G. Neves, G. N. Garrido, M. Norton, B. R. Paudyal, E. B. Pereira, Y. Poissant, L. Pratt, Q. Shen, T. Reindl, M. Rennhofer, C. D. Rodr  guez-Gallegos, R. R  ther, W. van Sark, M. A. Sevillano-Bendez  , H. Seigneur, J. A. Tejero, M. Theristis, J. A. T  fflinger, C. Ulbrich, W. A. Vilela, X. Xia, and M. A. Yamasoe, “Impact of measured spectrum variation on solar photovoltaic efficiencies worldwide,” *Renewable Energy*, vol. 196, pp. 995–1016, aug 2022.
- [65] M. A. Zamalloa Jara, H. Berg, L. A. Conde, M. A. Sevillano-Bendez  , A. M. Carhuavilca, R. Grieseler, and J. A. T  fflinger, “Extreme Overirradiance events and their spectral dis-

tribution in Lima, Peru,” *Journal of Physics: Conference Series*, vol. 1841, p. 012006, mar 2021.

- [66] M. A. Sevillano-Bendezú, L. A. Conde, J. de la Casa, and J. A. Töfflinger, “Average photon energy assessment based on modelled spectra from the National Solar Radiation Database for Lima, Peru,” *Journal of Physics: Conference Series*, vol. 2180, p. 012018, jan 2022.
- [67] N. Martín and J. M. Ruiz, “A new method for the spectral characterisation of PV modules,” *Progress in Photovoltaics: Research and Applications*, vol. 7, pp. 299–310, jul 1999.
- [68] G. Nofuentes, J. de la Casa, E. M. Solís-Alemán, and E. F. Fernández, “Spectral impact on PV performance in mid-latitude sunny inland sites: Experimental vs. modelled results,” *Energy*, vol. 141, pp. 1857–1868, 2017.
- [69] J. A. Caballero, E. F. Fernández, M. Theristis, F. Almonacid, and G. Nofuentes, “Spectral Corrections Based on Air Mass, Aerosol Optical Depth, and Precipitable Water for PV Performance Modeling,” *IEEE Journal of Photovoltaics*, vol. 8, no. 2, pp. 552–558, 2018.
- [70] R. Gottschalg, D. G. Infield, and M. J. Kearney, “Experimental study of variations of the solar spectrum of relevance to thin film solar cells,” *Solar Energy Materials and Solar Cells*, vol. 79, no. 4, pp. 527–537, 2003.
- [71] I. Sara, T. Betts, R. G. P. o. t. n. EUPVSEC, U. Frankfurt, U. Germany, and U. 2012, “Analysis of a suitable model for spectral response of a photovoltaic device,” *Solar Energy Conference*, 2012.
- [72] S. A. Kalogirou, *Solar energy engineering: processes and systems*. Academic Press, 2013.
- [73] B. Marion, “Numerical method for angle-of-incidence correction factors for diffuse radiation incident photovoltaic modules,” *Solar Energy*, vol. 147, pp. 344–348, may 2017.

- [74] A. Louwen, A. C. de Waal, R. E. I. Schropp, A. P. C. Faaij, and W. G. J. H. M. van Sark, “Comprehensive characterisation and analysis of PV module performance under real operating conditions,” *Progress in Photovoltaics: Research and Applications*, vol. 25, pp. 218–232, mar 2017.
- [75] C. N. Jardine, T. R. Betts, R. Gottschalg, D. G. Infield, and K. Lane, “Influence of Spectral Effects on the performance of multijunction amorphous silicon cells,” tech. rep., Europe Conference Proceedings, 2002.
- [76] S. R. Williams, T. R. Betts, R. Gottschalg, D. G. Infield, T. Helf, R. Gottschalg, H. G. Beyer, and D. G. Infield, “Modelling long-term module performance based on realistic reporting conditions with consideration to spectral effects,” *Energy*, vol. 2, pp. 165–168, may 2003.
- [77] T. Minemoto, Y. Nakada, H. Takahashi, and H. Takakura, “Uniqueness verification of solar spectrum index of average photon energy for evaluating outdoor performance of photovoltaic modules,” *Solar Energy*, vol. 83, pp. 1294–1299, aug 2009.
- [78] I. E. Commission, “Photovoltaic devices—Part 7: Computation of the spectral mismatch correction for measurements of photovoltaic devices,” tech. rep., 2008.
- [79] J. Silva, J. Rojas, M. Norabuena, C. Molina, R. A. Toro, and M. A. Leiva-Guzmán, “Particulate matter levels in a South American megacity: the metropolitan area of Lima-Callao, Peru,” *Environmental Monitoring and Assessment*, vol. 189, pp. 1–18, dec 2017.
- [80] M. Simon and E. L. Meyer, “The effects of spectral evaluation of c-Si modules,” *Progress in Photovoltaics: Research and Applications*, vol. 19, pp. 1–10, jan 2011.
- [81] J. S. Silva, J. P. Rojas, M. Norabuena, and R. J. Seguel, “Ozone and volatile organic compounds in the metropolitan area of Lima-Callao, Peru,” *Air Quality, Atmosphere and Health*, vol. 11, pp. 993–1008, oct 2018.

- [82] S. Nann and C. Riordan, "Solar spectral irradiance under clear and cloudy skies: Measurements and a semiempirical model," *Journal of Applied Meteorology*, vol. 30, no. 4, pp. 447–462, 1991.
- [83] R. García, M. Torres-Ramírez, E. Muñoz-Cerón, J. de la Casa, and J. Aguilera, "Spectral characterization of the solar resource of a sunny inland site for flat plate and concentrating PV systems," *Renewable Energy*, vol. 101, pp. 1169–1179, 2017.
- [84] J. Polo, M. Alonso-Abella, J. A. Ruiz-Arias, and J. L. Balenzategui, "Worldwide analysis of spectral factors for seven photovoltaic technologies," *Solar Energy*, vol. 142, pp. 194–203, jan 2017.
- [85] D. Dirnberger, G. Blackburn, B. Müller, and C. Reise, "On the impact of solar spectral irradiance on the yield of different PV technologies," *Solar Energy Materials and Solar Cells*, vol. 132, pp. 431–442, 2015.
- [86] J. Chantana, H. Mano, Y. Horio, Y. Hishikawa, and T. Minemoto, "Spectral mismatch correction factor indicated by average photon energy for precise outdoor performance measurements of different-type photovoltaic modules," *Renewable Energy*, vol. 114, pp. 567–573, 2017.
- [87] J. Chantana, Y. Imai, Y. Kawano, Y. Hishikawa, K. Nishioka, and T. Minemoto, "Impact of average photon energy on spectral gain and loss of various-type PV technologies at different locations," *Renewable Energy*, vol. 145, pp. 1317–1324, 2020.
- [88] E. F. Fernandez, F. A. Cruz, T. K. Mallick, and S. Sundaram, "Effect of Spectral Irradiance Variations on the Performance of Highly Efficient Environment-Friendly Solar Cells," *IEEE Journal of Photovoltaics*, vol. 5, pp. 1150–1157, jul 2015.
- [89] M. Tsuji, M. M. Rahman, Y. Hishikawa, K. Nishioka, and T. Minemoto, "Uniqueness verification of solar spectrum obtained from three sites in Japan based on similar index of average photon energy," *Solar Energy*, vol. 173, pp. 89–96, oct 2018.

- [90] H. Mano, M. Mijanur Rahman, A. Kamei, and T. Minemoto, “Impact estimation of average photon energy from two spectrum bands on short circuit current of photovoltaic modules,” *Solar Energy*, vol. 155, pp. 1300–1305, oct 2017.
- [91] G. Nofuentes, C. A. Gueymard, J. Aguilera, M. D. Pérez-Godoy, and F. Charte, “Is the average photon energy a unique characteristic of the spectral distribution of global irradiance?,” *Solar Energy*, vol. 149, pp. 32–43, 2017.
- [92] W. Seok Jin, *Digital Multimeters 34460A, 34461A, 34465A (6½ digit), 34470A (7½ digit)*. keysight, 2017.



Publications

Scientific publications indexed with relative quality index

1. M. A. Sevillano-Bendezú; J. A. Dulanto; **L. A. Conde**; R. Grieseler; J. A. Guerra; J. A. Töfflinger, (2020). Capacitance voltage curve simulations for different passivation parameters of dielectric layers on silicon. *Journal of Physics: Conference Series*, 1433 - 012007. (Percentile 18th SCOPUS – SJR).
<https://doi.org/10.1088/1742-6596/1433/1/012007>
2. **L. A. Conde**; J. R. Angulo; M. A. Sevillano-Bendezu; G. Nofuentes; J. A. Töfflinger; J. de la Casa, (2021). Spectral effects on the energy yield of various photovoltaic technologies in Lima (Peru). *Energy*, 223, art. no. 120034. (Q1 WOS-JCR)
<https://doi.org/10.1016/j.energy.2021.120034>
3. B. Calsi; **L. A. Conde**; J.R. Angulo; J. Montes-Romero; J.A. Guerra; J. de la Casa; J. A. Töfflinger, (2021). Monitoring versus prediction of the power of three different PV technologies in the coast of Lima-Peru. *Journal of Physics: Conference Series*, 1841 – 012001. (Percentile 18th SCOPUS – SJR).
<https://doi.org/10.1088/1742/6596/1841/1/012001>

4. M. Z. Jara; H. Berg, **L. A. Conde**; M. A. Sevillano-Bendezú; A. M. Carhuavilca; R. Grieseler; J. A. Töfflinger, (2021). Extreme Overirradiance events and their spectral distribution in Lima, Peru. *Journal of Physics: Conference Series*, 1841 - 1, 012006. (Percentile 18th SCOPUS – SJR).

<https://doi.org/10.1088/1742-6596/1841/1/012006>

5. A. M. Carhuavilca; **L. A. Conde**; A. E. Berastain; J. Montes-Romero; W. Gosgot; J. de la Casa; J. A. Töfflinger; M. A. Cataño, (2021). Monitoring system based on IEC standards for irradiance and module temperature measurements in photovoltaic systems. *Journal of Physics: Conference Series*, 1841 – 012002. (Percentile 18th SCOPUS – SJR).

<https://doi.org/10.1088/1742/6596/1841/1/012002>

6. P. Llontop; C. E. Torres; M. Piñeiro; **L. Conde**; A. Tejada; J. A. Töfflinger; F. Rumiche; F. F. H. Aragón; D. G. Pacheco-Salazar; R. Grieseler; L. Korte; J. A. Guerra, (2022). Indirect excitation and luminescence activation of Tb doped indium tin oxide and its impact on the host's optical and electrical properties. *Journal of Physics D: Applied Physics*, 55 - 21, 210002. (Percentile 18th SCOPUS – SJR).

<https://doi.org/10.1088/1361-6463/ac52fc>

7. J. R. Angulo; B. X. Calsi; **L. A. Conde**; J.A. Guerra; E. Muñoz-Cerón; J. de la Casa; J. A. Töfflinger (2022). Estimation of the effective nominal power of a photovoltaic generator under non-ideal operating conditions. *Solar Energy*; 231; pp. 784-792. (Q1 WOS-JCR).

<https://doi.org/10.1016/j.solener.2021.12.015>

8. M. A. Sevillano-Bendezú; **L. A. Conde**; J. de la Casa; J. A. Töfflinger, (2022). Average photon energy assessment based on modelled spectra from the National Solar Radiation Database for Lima, Peru. *Journal of Physics: Conference Series*, 2180(1) –012018. (Percentile 18th SCOPUS – SJR).

<https://doi.org/10.1088/1742/6596/2180/1/012018>

9. A. E. Berastain; **L. A. Conde**; J. Angulo; A. M. Carhuavilca; M. García; M. A. Sevillano-Bendezú; J. Montes-Romero; J. de la Casa; L. Chirinos; J. A. Töfflinger, (2022). Resolving challenges of monitoring PV systems: A case study for three 1.5 kW generators in Lima, Peru. *Journal of Physics: Conference Series*, 2180(1) – 012006. (Percentile 18th SCOPUS – SJR).

<https://doi.org/10.1088/1742/6596/2180/1/012006>

10. J. Angulo; **L. A. Conde**; E. Muñoz-Cerón; J. de la Casa; J. A. Töfflinger, (2022). PV generator nominal power estimation using a ground sensor and the PVLIB online irradiance database. *Journal of Physics: Conference Series*, 2180(1) – 012005. (Percentile 18th SCOPUS – SJR).

<https://doi.org/10.1088/1742/6596/2180/1/012005>

11. C.A. Espinosa-González; J. Angulo; **L. A. Conde**; A. M. Carhuavilca; E. F. Alfaro; R. Espinoza; J. A. Töfflinger; E. Muñoz-Cerón; J. de la Casa, (2022). Is the information provided by free satellite sources suitable for predicting or evaluating the performance of photovoltaic systems in Peru? (In memoriam to Heinrich Berg). *Journal of Physics: Conference Series*, 2180(1) – 012016. (Percentile 18th SCOPUS – SJR).

<https://doi.org/10.1088/1742/6596/2180/1/012016>

Scientific publications without relative quality index

1. R. Perich-Ibañez; M. Sevillano-Bendezú; J. Montes-Romero; **L. Conde-Mendoza**; J. R. Angulo-Abanto; J. de la Casa; J. A. Tofflinger (2020). Estudio de los métodos analíticos para la extracción de parámetros eléctricos de módulos fotovoltaicos de capas delgadas. *Revista Científica TECNIA*, 30, pp. 53-58.

<https://doi.org/10.21754/tecnia.v30i1.851>

2. J. R. Angulo-Abanto; B. Calsi-Silva; E. F. Alfaro-Collazos; **L. Conde-Mendoza**; E. Muñoz-Cerón; R. Grieseler; J. A. Guerra; J. Palomino-Tofflinger; R. Espinoza-Paredes; J. de la Casa, (2020). Estudio del efecto del polvo y estimación de la potencia nominal en un string fotovoltaico. Revista Científica TECNIA, 30, pp. 27-33.

<https://doi.org/10.21754/tecnia.v30i1.832>

3. B. Calsi-Silva; J.R. Angulo-Abanto; **L. Conde-Mendoza**; Emilio Muñoz Cerón; R. Grieseler; J.A. Guerra; J. de la Casa; J. Palomino-Tofflinger, (2020). Procedimiento del cálculo de la potencia nominal de un generador fotovoltaico. Revista Científica TECNIA, 30, pp. 22-26.

<https://doi.org/10.21754/tecnia.v30i1.834>

4. **L. Conde-Mendoza**; J. Montes-Romero; A. Carhuavilca-Vela; R. Perich-Ibañez; J.A. Guerra; M. Sevillano-Bendezú; B. Calsi-Silva; J.R. Angulo-Abanto; J. de la Casa; J. A. Tofflinger, (2020). Puesta en marcha de un laboratorio para la caracterización de tecnologías fotovoltaicas a sol real bajo las condiciones climáticas de Lima, Revista Científica TECNIA, 30, pp. 80-89.

<https://doi.org/10.21754/tecnia.v30i1.835>

Communications in congresses with paper indexed in scopus

1. **L. A. Conde-Mendoza**; J. Montes-Romero; A. Carhuavilca; R. Perich; J. A. Guerra; J. Angulo-Abanto; E. Muñoz-Cerón; J. A. Töfflinger; J. de la Casa. PERFORMANCE EVALUATION AND CHARACTERIZATION OF DIFFERENT PHOTOVOLTAIC TECHNOLOGIES UNDER THE COASTAL DESERT CLIMATE CONDITIONS OF LIMA, PERÚ. En: ISES Solar World Congress 2019, Santiago de Chile, 2019, pp. 695-702. Participation: Poster and communication.

<http://dx.doi.org/10.18086/swc.2019.16.01>

2. J. Angulo-Abanto; B. Calsi; **L. Conde-Mendoza**; E. Muñoz-Ceron; R. Grieseler; J. A. Guerra; J. de la Casa; J. A. Töfflinger. MODELING OF THE NOMINAL POWER OF A PV GENERATOR UNDER CLEAR AND CLOUDY SKY CONDITIONS. En: ISES Solar World Congress 2019, Santiago de Chile, 2019, pp. 695-702. Poster and communication.

<http://dx.doi.org/10.18086/swc.2019.14.01>

